



**XANES STUDY OF CHEMISTRY OF LOCALISED CORROSION
IN ARTIFICIAL PITS OF
316L STAINLESS STEEL AND TITANIUM**

By

Mehdi Monir

**A thesis submitted to the University of Birmingham for the degree
of Doctor of Philosophy**

**Metallurgy and Materials
University of Birmingham**

September 2011

**UNIVERSITY OF
BIRMINGHAM**

University of Birmingham Research Archive

e-theses repository

This unpublished thesis/dissertation is copyright of the author and/or third parties. The intellectual property rights of the author or third parties in respect of this work are as defined by The Copyright Designs and Patents Act 1988 or as modified by any successor legislation.

Any use made of information contained in this thesis/dissertation must be in accordance with that legislation and must be properly acknowledged. Further distribution or reproduction in any format is prohibited without the permission of the copyright holder.

Abstract

X-ray absorption near edge structure (XANES) experiments on artificial pits of 316L stainless steel were carried out to study the oxidation state and speciation of alloying elements in the pit solution. It was confirmed that the oxidation states of Fe, Cr and Ni are 2+, 3+ and 2+, respectively. $\text{Ni}(\text{H}_2\text{O})_6^{2+}$ was found to be the main solution species through the pit with no evidence of any Ni-Cl complexes. However, for iron and chromium, hexa-aquo ions ($\text{Fe}(\text{H}_2\text{O})_6^{2+}$ and $\text{Cr}(\text{H}_2\text{O})_6^{3+}$) were found near the pit mouth with chloro complexes close to the dissolving metal surface.

The chemistry of molybdenum species in artificial pits of 316L stainless was investigated and the molybdenum oxidation state was found to be 3+. There was no evidence of any Mo(VI) polymolybdates, which have previously been proposed to explain the beneficial effects of Mo on the corrosion resistance of 316L stainless steel. High resolutions measurements did not detect any different molybdenum species adjacent to the salt film.

XANES measurements on titanium artificial pits showed a presence of TiCl_4 , titanium oxides (rutile and anatase) and metal fragments that were generated during the electrochemical dissolution process. X-ray fluorescence and XANES were also carried out to study the titanium distribution and species in human tissues extracted from the vicinity of failed knee, BAHA (bone-anchored hearing aid) and dental implants. Metal fragments and titanium oxides (rutile and anatase) were found in the tissues. In addition, XANES was carried out on neutrophil cells that had been cultured in the presence of anatase. In one case, a spectrum of rutile was found, suggesting the cells may be able to convert anatase to rutile.

Acknowledgments

This work was carried out in the School of Metallurgy and Materials within the University of Birmingham and supported by EPSRC grant.

I would like to express my gratitude to my supervisor Dr. Alison J. Davenport for her valuable care, support and guidance during last four years. I would also like to thank my co-advisor Prof. Trevor Rayment for all his precious help, advice and support. Special thanks to Prof. Andrew Dent for productive meetings and discussions at Diamond Light Source.

I would also like to thank Dr. Richard Martin (Aston University), Owen Addison (University of Birmingham, Dental School) and Sonam Kalra (University of Birmingham, Dental School) for their help on titanium experiments.

I greatly acknowledge all of help from people at Diamond Light Source. I would like to specially thank I18 beamline scientists (Fred Mosselmans, Paul Quinn and Tina Geraki), B18 beamline (Giannantonio Cibin and Silvia Ramos) and B16 beamline (Dr Igor Dolbnya) for their help and support during experiments.

I wish to thank Dr. Roger Sebenik of AAA Molybdenum Products Inc. for supplying K_3MoCl_6 .

I would also especially like to thank Joshua A. Hammons, Majid Ghahari and Mahrez Amri for the extensive support and help in the lab and during synchrotron experiments.

I owe my deepest gratitude to my beloved families and all friends for their understanding and support throughout my PhD.

Contents

List of Abbreviations.....	vi
1. Introduction.....	1
2. Literature review	4
2.1. Forms of corrosion	4
2.2. Localised corrosion	5
2.2.1. Pitting corrosion.....	6
2.2.2. Crevice corrosion	8
2.2.3. Intergranular corrosion.....	9
2.3. Stability of pit growth	10
2.4. Artificial pits	11
2.5. Salt film.....	14
2.6. Pitting of stainless steel.....	16
2.6.1. Introduction.....	16
2.6.2. Chemistry of pits in stainless steel	17
2.7. Role of Mo in stainless steel corrosion behaviour	18
2.8. Localised corrosion of titanium	19
2.8.1. Introduction.....	19
2.8.2. Pitting corrosion of Ti	19
2.8.3. Crevice corrosion of titanium.....	20
2.8.4. Mechanically assisted crevice corrosion	21
2.8.5. Artificial pits of titanium.....	22
2.8.6. Pit chemistry.....	22
2.9. Corrosion of titanium in the body	24
2.9.1. Titanium alloys and microstructure.....	24
2.9.2. Titanium alloys for biomedical applications	24
2.9.3. Mechanisms of corrosion in the body	25
2.9.4. Effect of Ti species on human tissue.....	26
2.9.5. Titanium alloys biological effects and toxicity on human body	28
2.10. Synchrotron methods for in situ characterisation of corrosion	29
2.10.1. Introduction.....	29
2.10.2. X-ray absorption spectroscopy.....	29
2.10.3. X-ray fluorescence mapping	34
2.10.4. XAS studies of Fe chemistry.....	35

2.10.5. XAS studies of Cr chemistry.....	39
2.10.6. XAS studies of Ni chemistry.....	43
2.10.7. XAS studies of Mo chemistry	45
2.10.8. XAS studies of Ti chemistry	48
2.11. Summary	54
3. Experimental method	55
3.1. Metal foils for electrochemical measurements.....	55
3.2. Standards for XAS measurements.....	55
3.2.1. Metal foils for calibration.....	55
3.2.2. Procedures for preparing of powder standards.....	56
3.2.3. Procedures for preparation of liquid standards.....	56
3.2.4. Mo (V) preparation	58
3.2.5. Mo (III) preparation by adding zinc powder to Mo (V).....	59
3.2.6. Reference materials for XANES measurements	61
3.2.7. Ringer's solution and BSA.....	63
3.3. Electrochemical cells and procedures for synchrotron studies of artificial pits	63
3.3.1. Electrochemical cells and samples	63
3.3.2. Electrochemical procedures for growing artificial pits	64
3.4. Preparation of human tissue and cell culture samples.....	65
3.5. Synchrotron experiments	66
3.5.1. XANES experiments at Diamond I18 beamline	66
3.5.2. XRF mapping at Diamond I18 beamline	68
3.5.3. XANES measurements at Diamond B16	68
3.5.4. XANES measurements at Diamond B18	68
3.6. XAS data analysis	69
3.6.1. XANES	69
4. Chemistry of Fe, Ni and Cr in 316L stainless steel artificial pits	71
4.1. Introduction	71
4.2. Results.....	71
4.2.1. Electrochemistry of pit growth.....	71
4.2.2. Speciation of Fe in 316L stainless steel artificial pit.....	73
4.2.3. Fe spectroscopy in 316L stainless steel artificial pits	74
4.2.4. Speciation of Cr in artificial pit of 316L stainless steel	80
4.2.5. Cr spectroscopy in 316L stainless steel artificial pits	82

4.2.6. Speciation of Ni in artificial pit of 316L stainless steel	84
4.3. Discussion	87
4.3.1. Fe spectroscopy in 316L stainless steel artificial pits	87
4.3.2. Cr spectroscopy in 316L stainless steel artificial pits	88
4.3.3. Ni spectroscopy in 316L stainless steel artificial pits	89
4.4. Conclusions.....	90
5. Chemistry of Mo in 316L stainless steel artificial pits.....	91
5.1. Introduction.....	91
5.2. Results.....	91
5.3. Discussion	100
5.4. Conclusions.....	103
6. Spectroscopy of Ti in human tissue and artificial corrosion pits	104
6.1. Introduction.....	104
6.2. Results.....	104
6.2.1. Ti reference compounds	104
6.2.2. Ti artificial pit	106
6.2.3. Ti XANES in artificial pits.....	109
6.2.4. Ti XANES in BSA and Ringers solutions	115
6.2.5. Ti XANES in neutrophil cells	117
6.2.6. XRF mapping of human tissues	118
6.2.7. Ti XANES in human tissues	120
6.3. Discussion	128
6.4. Conclusions.....	130
7. Summary	131
7.1.1. Fe, Cr, Ni speciation in 316L stainless steel artificial pits	131
7.1.2. Mo speciation in 316L stainless steel artificial pits	131
7.1.3. Ti XANES studies in artificial pits and human tissues	132
8. Future work	134
9. References.....	136

List of Abbreviations

1D	One Dimensional
2D	Two Dimensional
3D	Three Dimensional
XANES	X-ray Absorption Near Edge Structure
EXAFS	Extended X-ray Absorption Fine Structure
XRF	X-ray Fluorescence
SECM	Scanning Electrochemical Microscopy
MACC	Mechanically Assisted Corrosion Cracking
XAS	X-ray Absorption Spectroscopy
CP-Ti	Commercially Pure Titanium
Ti-6Al-4V	Titanium, 6% Aluminium and 4% Vanadium
SEM	Scanning Electron Microscopy
TEM	Transmission Electron Microscopy
BSA	Bovine Serum Albumin
PBS	Phosphate Buffer Solution

1. Introduction

Pitting corrosion is one of the most important types of corrosion that occurs on alloys such as stainless steel in chloride environments. Very acidic environments with high concentration of metal cations within a salt film present at metal/solution interface are required to maintain the pit stable and growing.

Different aspects of corrosion of stainless steel such as pitting potential, pitting propagation mechanisms and passivation behaviour have been studied in a wide range of environments, but the chemistry and complexation of species present within pits have been very little studied, and restricted to some Raman Spectroscopy measurements studying the chemistry of alloying species in chloride environment.

1D artificial pit is one of the methods of studying the pit solution chemistry by growing the pit under potentiostatic conditions. Artificial pits were initially introduced to study the salt film formation on corroding behaviour of stainless steel and titanium. Further work was then carried out to study the passivation and dissolution kinetics of stainless steel. The elemental composition within stainless steel artificial pits has been investigated, but the oxidation state and coordination of the alloying elements (Fe, Cr, Ni and Mo) in 316L stainless steel have not previously been studied in chloride solutions owing to the difficulty of characterising pits *in situ* during their growth.

Synchrotron x-ray methods such as X-ray absorption near edge structure (XANES) are ideal for characterising solution chemistry. XANES is very sensitive to oxidation state and coordination of the absorbing atom; therefore it is an ideal probe for investigating the chemistry of metal ions in localised corrosion sites *in situ* and in real time. There is also

limited number of standard compounds used in previous works which is very crucial for elements with wide range of oxidation states. In this project, XANES was used to study the oxidation state and complexation of Fe, Cr, Ni and Mo inside corrosion pits in 316L stainless steel.

In order to identify the species present within artificial pits, their spectra are compared with different standard compounds in solid and solution states. This will help to cover all the possible oxidation states of solution species mainly for Mo. The chemistry of Mo is of particular interest because its role in improving the corrosion resistance of 316L stainless steel is not well understood.

Over 1000 ton of titanium is implanted annually into patients in the form of medical prostheses used for orthopaedic, craniofacial and dental rehabilitation. Ti-6Al-4V and CP-Ti are the main type of alloys used in body implants. Ti is usually considered to be a biocompatible material for human implantation. However, concern is now being raised over the potential biological effects of particles and Ti ions generated by wear and corrosion processes such as those causing failure of cemented Ti hip implants. Titanium alloys are very corrosion resistant materials but they are vulnerable to pitting corrosion only in halide solutions at high potentials or high temperatures. However, they may undergo crevice corrosion at low temperatures in the presence of any micro-motion between the surfaces. There is therefore concern that such processes may cause release of Ti species into human tissue around implants, which can therefore cause adverse cell reactions. In this project, X-ray fluorescence mapping is used to determine the distribution of titanium species in human tissues taken from retrieved implants. The results from tissues adjacent to knee, BAHA (bone-anchored hearing aid) and dental implants are compared with XANES measurements on 1D

artificial pit to gain an understanding of the processes leading to the formation of the corrosion products in tissue.

Titanium chemistry has been less studied in chloride environments due to high corrosion resistance of titanium alloys at low potentials and low temperatures. XANES Studies of titanium oxidation state has been only limited to solids and mineral compounds of titanium and less understood in solution environments. Therefore, XANES can be used as a very unique method to explore the oxidation state and chemistry of titanium in solution environments.

Titanium artificial pits have previously only been studied electrochemically. In this project, the solution species and corrosion products within the pits are investigated with XANES in order to identify the species present. Solution and solid standards compounds of titanium were used to identify the species present during electrochemical dissolution of titanium in chloride environment.

In order to simulate the possible species formed as a result of reaction between titanium corrosion products and the environment in the body, BSA has been used as the protein type and Ringers solution has been used as the inorganic part of body fluid to simulate the environment in the body.

2. Literature review

2.1. Forms of corrosion

All the system failures are very important in industries and corrosion is one of the critical issues that needs investigation to find out the cause of failure. The main important forms of corrosion are: Uniform (or general) corrosion, Crevice, Pitting, Galvanic, Selective leaching, Erosion, Environmental cracking and Intergranular corrosion [1, 2]. Different forms of corrosion are based on the appearance of the corroded metal and ease of identification as shown in Figure 2.1[1, 2].

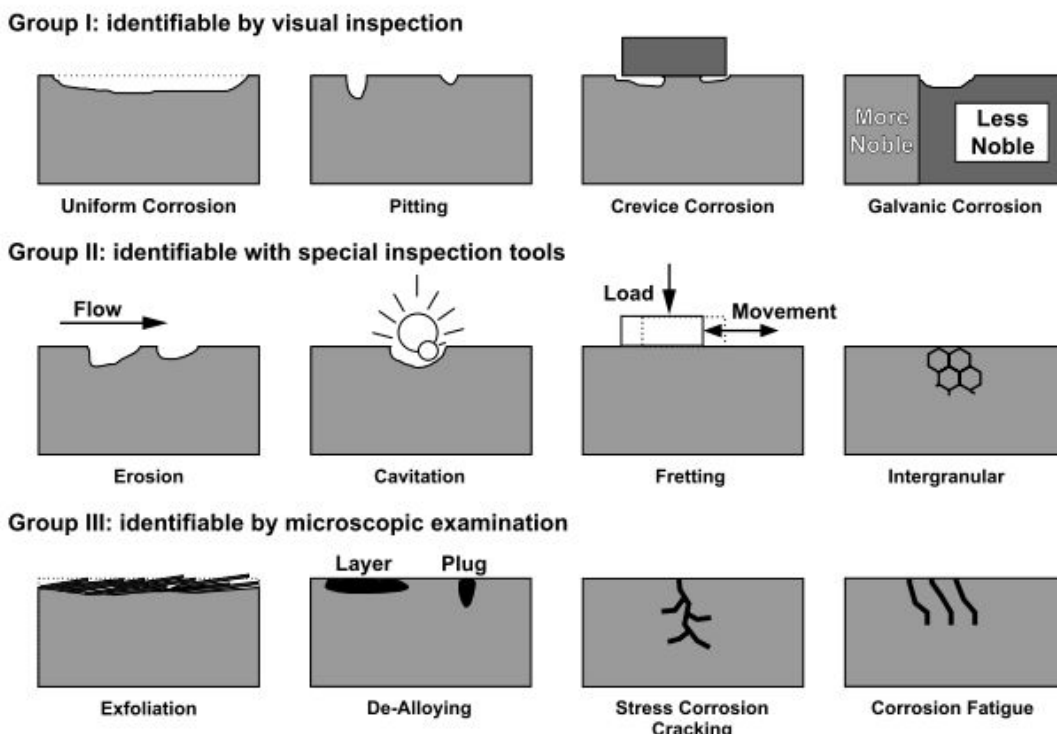


Figure 2.1 Main forms of corrosion regrouped by their ease of recognition [2].

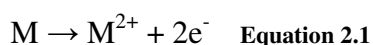
General corrosion is a type of attack over the entire exposed surface area or large fraction of the total area of material which results the metal thinning and eventual failure. Uniform corrosion is not of a great interest, because the lifetime of equipment can be accurately

predicted. This type of corrosion can be prevented by using the suitable materials with coatings, inhibitors or a cathodic protection system.

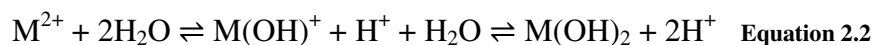
Most of corrosion types are localised attack and restricted to specific parts or areas of equipment, therefore, it is difficult to predict the occurrence. The main types of localised corrosion are pitting, crevice and intergranular corrosion [1].

2.2. Localised corrosion

Most metals owe their resistance to general corrosion in wet environments to the presence of a thin passive oxide film. However, corrosion can develop at one part of a metal surface. Different forms of localised corrosion such as pitting and crevice corrosion are critical issues in a wide range of applications. They are generally associated with the presence of chloride ions, which facilitate dissolution of the metal [3]. At some local sites on the metal surface such as inclusions, metal dissolution (anodic reaction) will occur and forms metal cations [4]:



Where, “M” represents a dissolving metal. This reaction produces electron flow in an electrical circuit from the corroding sites (anode) to the metal surface (cathode), which is passive. The dissolution of metal in these anodic sites leads to a build up of chloride ions inside the pit to balance the positive charge of metal cations. This process will also decrease the pH due to hydrolysis of metal ions [3, 4]:



High chloride concentration and low pH inside the corroding pit prevents repassivation of the metal surface and accelerates dissolution of metal Figure 2.2. The concentration of metal ions within the pit controls both the pH (through hydrolysis) and the chloride concentration (through charge balance). If the rate of metal ion production within the pit through metal dissolution is less than the rate at which the ions escape from the pit, then the solution will be diluted, and repassivation of the pit will take place. However, if the rate of metal dissolution is greater than the rate of escape at the pit mouth, then the pit will become supersaturated in metal and a metal chloride salt film may precipitate.

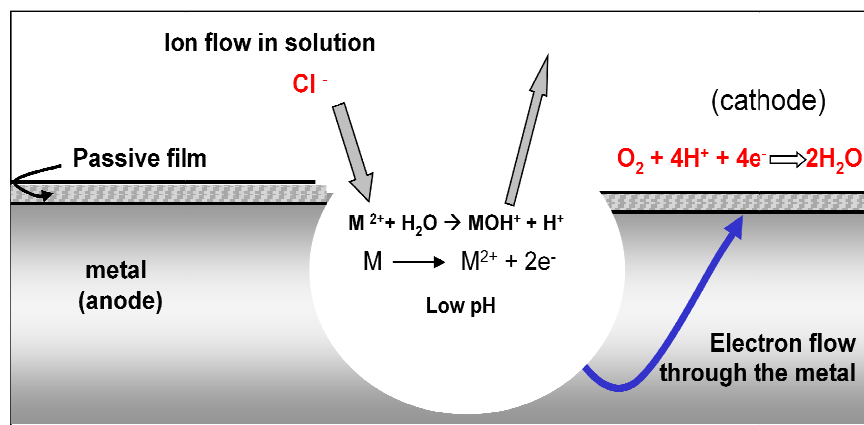


Figure 2.2 Schematic diagram of the corrosion process taking place in localised corrosion.

2.2.1. Pitting corrosion

Pitting corrosion is one the most common types and destructive forms of localised corrosion which occurs on the surface of metals. Pitting corrosion generally occurs on passive layers of stainless steel due to a presence of inclusions or geometrical defects or where the passive layer is damaged [3]. The pits can be observed in different geometrical shapes such as wide and shallow or narrow and deep as shown in Figure 2.3.

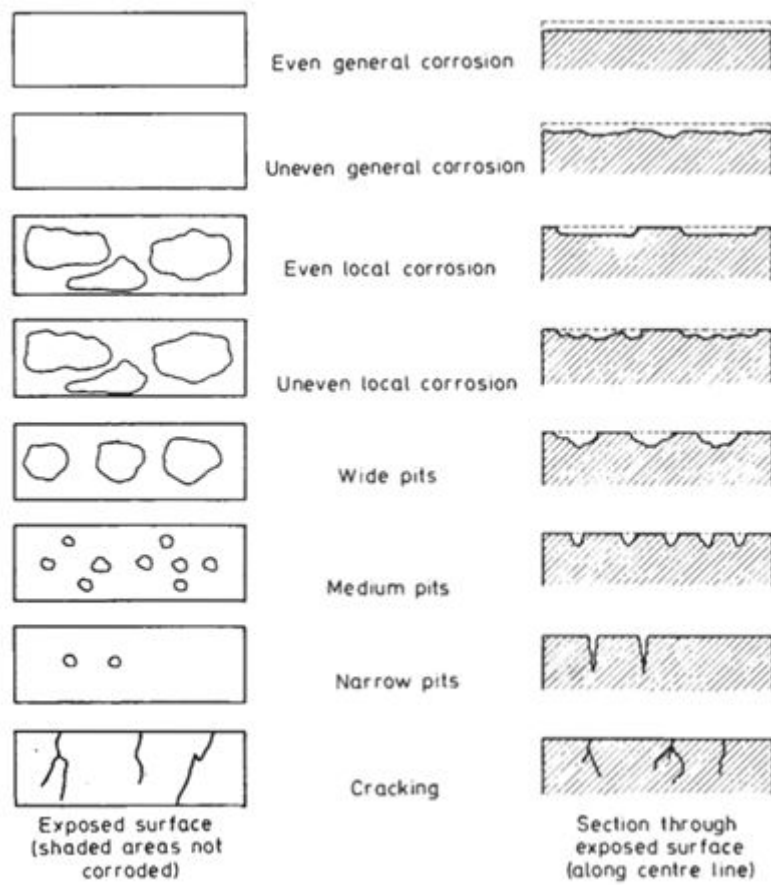


Figure 2.3 Different types of corrosion pits (left: top view; right: side view) [4].

This type of corrosion usually occurs in the holes that may be small or large in size. Pits are generally difficult to detect because of their small size or because they are covered with corrosion products. It is also difficult to measure the pits quantitatively since they occur in different pit depths. Pits usually grow vertically in the direction of gravity. Pits also tend to undermine or undercut the surface when they start growing [5, 6].

Increasing the velocity of environment solution often decreases the pitting attack. Surface finish has also remarkable effect on pitting resistance of materials and it is less likely to have pitting corrosion on polished surfaces [1].

Adding 2% of Molybdenum to 304 stainless steel to produce 316 stainless steel increases the pitting resistance. Generally, stainless steels with high content of molybdenum has more pitting resistance but less compared with titanium [1].

2.2.2. Crevice corrosion

Crevice corrosion is a form of localised corrosion usually occurs at stagnant environments in crevices such as under gaskets, washers, insulation materials, surface deposits and clamps [1]. Sands, dirt, corrosion products and other solids can act as a shield to create a stagnant environment for crevice corrosion. A crevice size is a critical factor for crevice corrosion to happen and must be wide enough to permit liquid entry and narrow enough to keep the environment stagnant. Because of this reason, crevice corrosion rarely occurs in openings with more than a few thousands of an inch width [1].

In Crevice corrosion, after a short time the oxygen within the crevice is depleted because of oxygen diffusion restriction into the crevice. After oxygen depletion, no oxygen reduction occurs in the crevice and metal dissolution increases the positive charge (M^+) causes chloride ions migration into the crevice and formation of metal chlorides and then metal chloride hydrolysis occurs as shown in Figure 2.4.

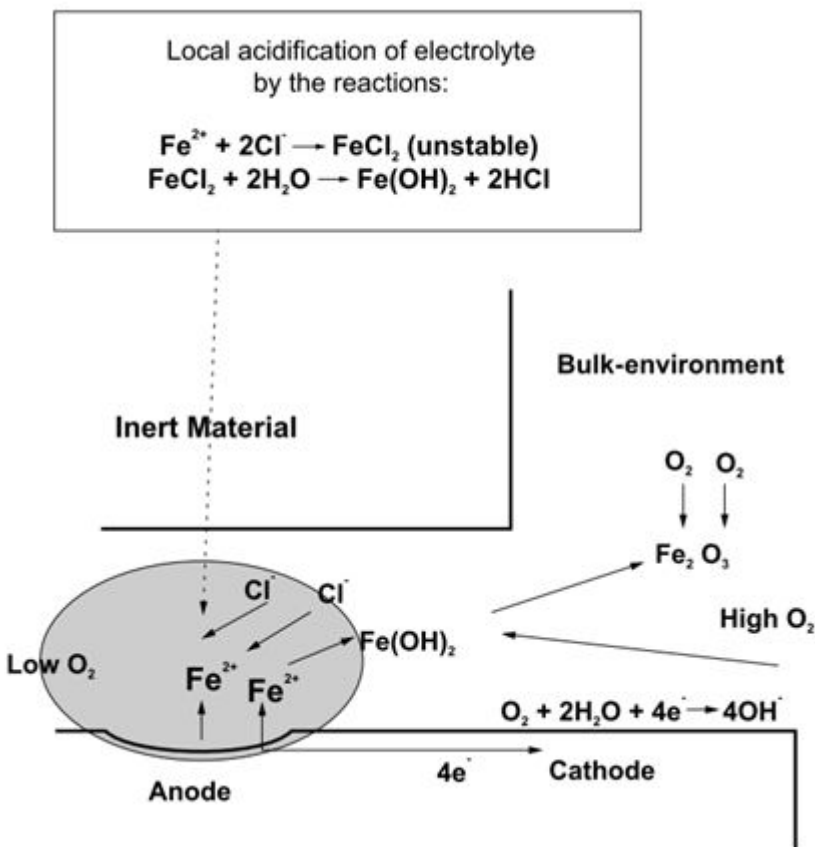


Figure 2.4 Crevice corrosion mechanism of steel in chloride environment [2].

2.2.3. Intergranular corrosion

Intergranular corrosion is a localised type of attack along the grain boundaries or adjacent to grain boundaries while the grains remain unaffected. Impurities tend to be enriched in the form of precipitated phases at grain boundaries [1]. These precipitations produce zones of reduced corrosion resistance adjacent to grain boundaries. The most famous type of this corrosion is the sensitisation of stainless steels. This intergranular corrosion in stainless steels is based on depletion of chromium in areas adjacent to grain boundaries. Generally more than 10% chromium is needed to produce a stainless steel. In the range of 950 to 1450°F, Cr₂₃C₆ is insoluble and precipitates in grain boundary as shown in Figure 2.5. The chromium depleted

zone is corroded because of lower corrosion resistance of this area. This is very common in 304 stainless steels [1].

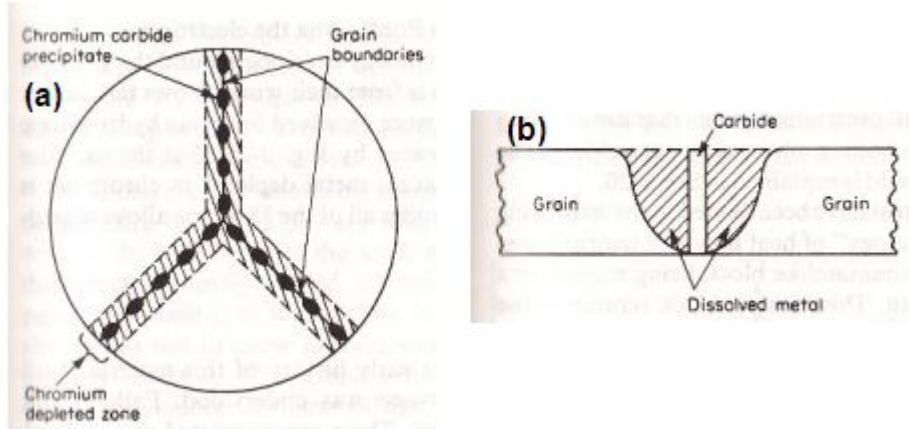


Figure 2.5 (a) Schematic representation of a grain boundary in sensitised 304 stainless steel
(b) Cross section of area shown in (a) [1].

2.3. Stability of pit growth

It is very well known now that pit propagation requires acidification inside the cavity. In 1937, Hoar [7] was the first who showed the localised aggressive chemistry of pits in tin in neutral bulk solutions. The very low pH values inside pit cavity were later measured by Suzuki et al. [8] and Wilde et al. [9].

The pitting potential (E_{pit}) is one of the important values which usually is measured in studying the pitting corrosion behaviour. Corrosion pits can stably grow above the pitting potential. Stable pit growth require high anodic dissolution rate inside the corrosion pit which contains a high concentration of chloride ions with a lower pH comparing to the bulk solution [10].

In 1976, Galvele [10] proposed a model for the acidification process required for stable pit propagation. He assumed that cracks in the passive film cause bare metal surface to be

exposed to the solution, and under this condition he calculated the condition required for stable pitting. He simplified the dissolution reactions into one-dimensional pit geometry and solved the transport equations for all species in a stable pit in a steady state condition. He calculated the values of a critical quantity ix , where i is the pit current density and x is the pit depth. The pit will propagate in a stable way when the product ix reaches a high enough pH value lower than the critical value required for corrosion.

2.4. Artificial pits

Real pits are very difficult to study as they have a complex geometry that changes with time. Pits have different shapes, for example pits in 302 stainless steel undercut the surface and have lacy covers [11]. The active surface area of the pit increases as it grows and this can be difficult to measure as a function of time. In addition, the number of the pits that can grow simultaneously is random and difficult to predict. Instead, artificial pits have been used widely for in situ study of pit geometry and chemistry of the pit solution [12-14].

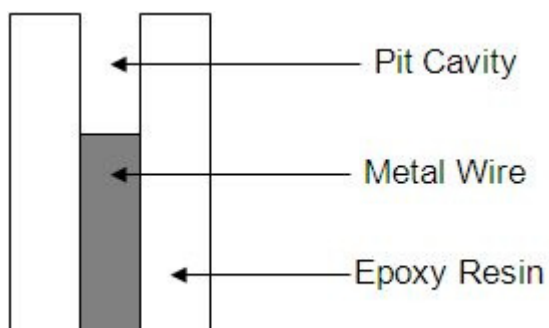


Figure 2.6 Schematic diagram of 1D artificial pit electrode.

The artificial pit method was introduced by Isaacs and Tester [15, 16] for in situ study of localised corrosion of 304 stainless steel and followed by Beck to study the pitting behaviour of titanium [17, 18]. Hunkeler and Bohni [19] have also used the same method to study the mass transport control of 302 and 316 stainless steel wires and 99.98% purity nickel. Artificial pits can be prepared by embedding a metal wire or foil with epoxy resin similar to lead in a pencil. The metal surface is dissolved to a certain depth as illustrated in

Figure 2.6. Artificial pits have been widely used to study the behaviour of salt films on stainless steels [12, 20-22]. Isaacs [12] has studied resistance and thickness of the salt film followed by in situ X-ray fluorescence to study the metallic cation concentration in an artificial pit of stainless steel. Further works by Newman and Isaacs [20] and Steinsmo [21, 22] have studied the dissolution and passivation kinetics of stainless steels and Fe-Cr alloys using 1D artificial pits. Assuming that all the charge passed was consumed in metal dissolution, the pit depth x , can be calculated by integrating the current passed during the dissolution [16]:

$$x = \int_0^t \frac{M}{AnF\rho} idt \quad \text{Equation 2.3}$$

where t is dissolution time, M is the molecular weight of the metal, A is the area of dissolving metal, n is the number of electrons produced for dissolution of metal, F is the Faraday constant (96500 C/mol) and ρ is the density. This equation derives from Fraday law as shown below [16]:

$$Q = \int idt \quad \text{Equation 2.4}$$

Where Q is the charge passed and i is the current passed during the dissolution.

The current-voltage characteristics of an artificial pit are shown in Figure 2.7. The current increases and is controlled by the iR drop in the pit by increasing the voltage from point A to B. From B to C, where metal ions are being produced faster than they can escape from the pit cavity by a diffusion process, a salt film precipitates at the metal/solution interface, so there is a sudden drop in current to D. Then the current is limited by diffusion of ions out of the pit cavity, and the salt film thickness is adjusted to support the potential drop (E). This current is called limiting current density (i_{lim}) [5]:

$$i_{lim} = \frac{nFDC}{x} \quad \text{Equation 2.5}$$

Where, n is the number of the electrons produced, F is Faraday constant (96500 C/mol), D is the diffusion coefficient of ions, C is the concentration of ions and x is the pit depth. This equation derives from Nernst-Einstein equation. Tester and Isaacs [16] didn't observe any bubbles in wire anode system, therefore, simplified the Nernst-Einstein equation to :

$$\frac{i}{AnF} = -D \frac{\partial C}{\partial X} \quad \text{Equation 2.6}$$

Where, A is the area of dissolving metal, n is the number of the electrons produced, F is Faraday constant (96500 C/mol), D is the diffusion coefficient of ions, C is the concentration of ions and x is the pit depth.

By reversing the potential at point E, the salt film is present at the surface from point E to F until the iR drop-limited current is lower than the diffusion-limited current and the salt film dissolves (F, G).

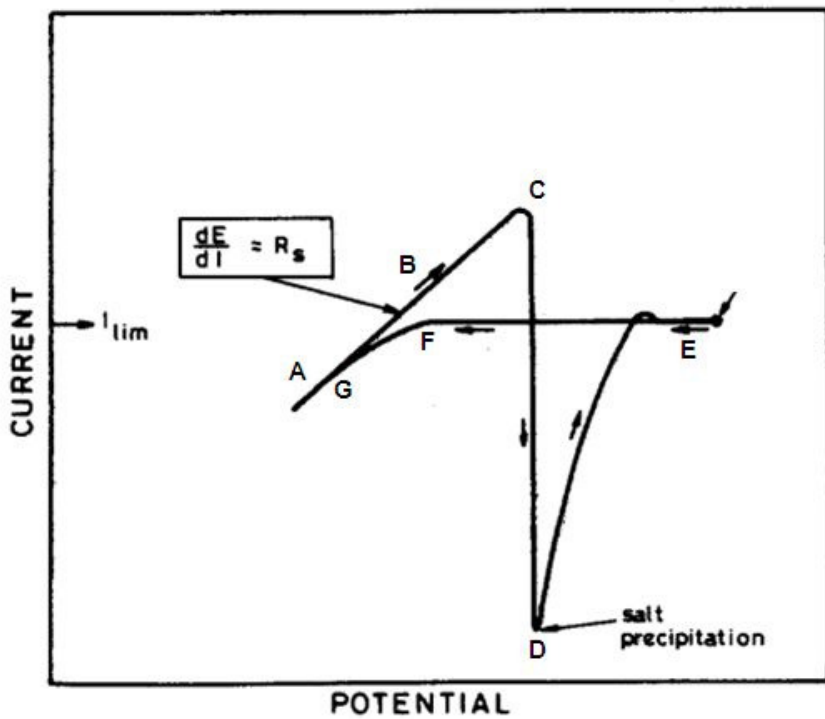


Figure 2.7 Current-voltage characteristics of artificial pit of stainless steel type 302(18Cr-8Ni) at 0.1 M HCl with scan rate of 50 mV/s at room temperature ($19\pm 3^\circ\text{C}$) [23].

2.5. Salt film

As described above, when the rate of production of metal cations at the interface exceeds the rate that cations escape from the metal/solution interface, a salt film forms and a stable pit grows as shown in

Figure 2.8. Vetter and Strehblow [24] claimed that at the bottom of stable pits, a thin non-porous salt layer similar to the passive layer can form. Isaacs [12] also studied the composition (Fe,Cr,Ni) of the salt layer in chloride solutions by using X-ray fluorescence and showed that the salt layer is mostly iron in comparison to little chromium and nickel. Newman et al.[20, 25-27] have also carried out a lot of work on stainless steel pit chemistry including Fe, Cr, Ni and Mo species mainly in chloride environments.

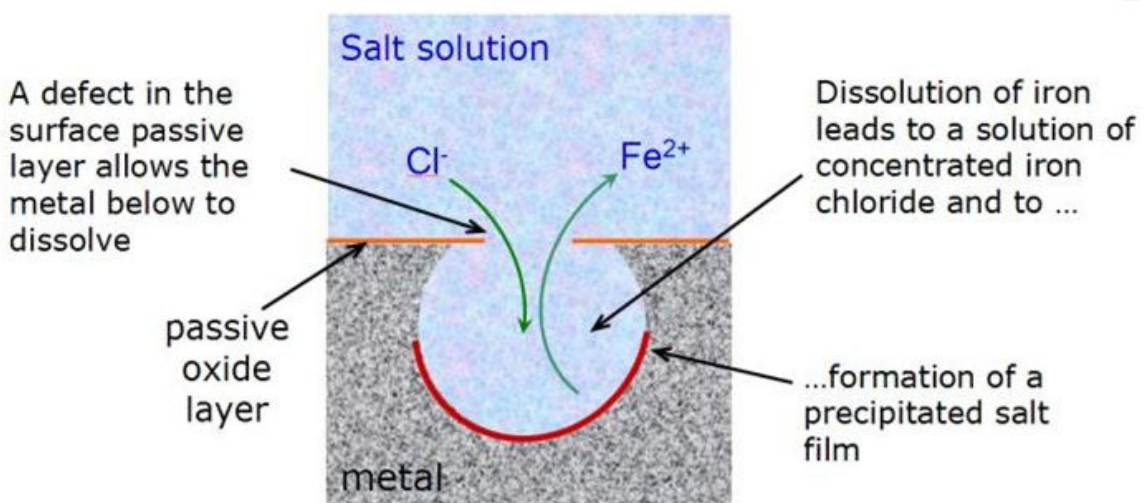


Figure 2.8 Schematic of salt film inside a corrosion pit of iron

Beck et al. [17, 18] also claimed the presence of a salt film on pit surfaces of titanium. Beck and Alkire [28] concluded from their calculations that the salt layer thickness could be 40 to 190 Å. Isaacs [15] has also studied the layer formed on stainless steel in various chloride solutions and concluded that the salt film has approximately 100 Å thickness with a resistivity of about 108 Ω.cm.

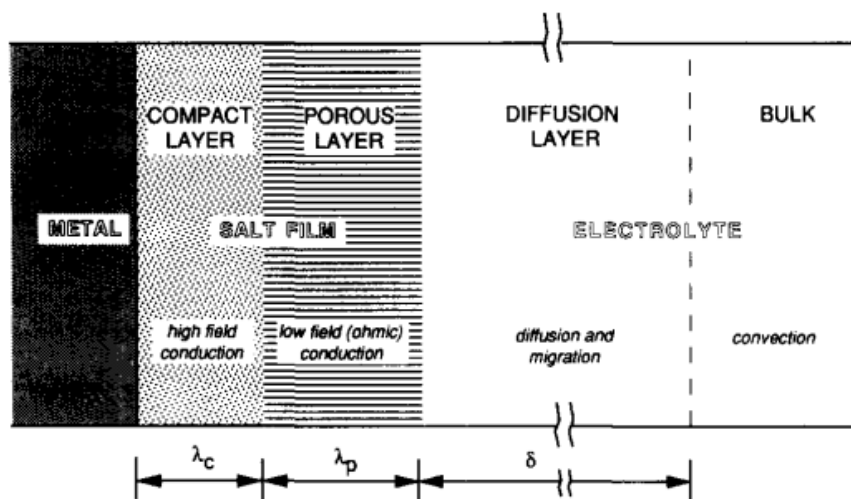


Figure 2.9 Schematic presentation of the salt film [29]

Grimm and Landolt [29, 30] proposed a salt film layer for iron with duplex structure including an inner compact layer showing high field conduction and outer layer with ohmic conduction through a porous layer as shown in

Figure 2.9. The thickness of the layer is a function of the potential and the diffusion rate of metal ions from the layer/solution interface. Several researchers [12, 31, 32] have reported that the salt film thickness increases with increasing potential or as the pit deepens.

Sridhar and Dunn [33] also have studied the structure of the salt film grown on nickel in chloride environments using Raman spectroscopy and detected the presence of solid $\text{NiCl}_2 \cdot 6(\text{H}_2\text{O})$ in the salt film formed in a 10 mm deep pit.

2.6. Pitting of stainless steel

2.6.1. Introduction

Pitting corrosion can be considered as two separate initiation and propagation stages. Pitting corrosion of stainless steel commonly starts with a nucleation process that occurs at nucleation sites or surface defects [34]. There are many theories of pit initiation on stainless steel focusing on passive film penetration, film breaking, or adsorption [3]. However, for commercial stainless steels, manganese sulphide (MnS) inclusions have been identified as the main pit initiation sites [35]. Corrosion pits on stainless steel exposed to chloride solution grow in two stages of metastable and stable. Metastable pits initiate and grow for a limited time before repassivation and their survival depends on the maintenance of a perforated cover over the pit mouth as an effective barrier to diffusion [36]. One of the characteristics of pitting in stainless steel is the perforated cover on the pit cavity commonly known as lacy cover. Most recently, Ernst [5, 6] studied the lacy cover formation in 2D pits using video microscopy

and Ghahari et al. [37] demonstrated the similar growth pattern in 3D through tomography studies.

2.6.2. Chemistry of pits in stainless steel

The pH of the pit environment was measured and reported by Mankowski [38], less than zero in some experiments. Tester and Isaacs [16] showed that stainless steel 304 could dissolve under anodic dissolution through an iron rich salt film.

Salt film formation in stainless steels has been extensively studied but the effect of different alloying elements in stable growth, critical chloride concentration for propagation of the pit and dissolution kinetics are still unclear. Therefore, the composition of the solution in the pit and presence of any metal-chloro complexes needs to be investigated more in detail.

Isaacs et al. [12] studied the composition of the salt film in Fe-18Cr-13Ni stainless steel by X-ray fluorescence and found that the salt film enriched in Fe and depleted in Ni and Cr. They also calculated the metal cations concentration and reported the value to be 5 M (3.4 M Fe, 1.1 M Cr, 0.5 M Ni). In their investigations, the cation species in the solution and solubility of metal chloride were not considered. Speciation is a critical factor in understanding the composition of stable pit growth.

Sridhar et al. [39] and Brossia et al. [40] have studied the chemistry of pits and crevices in stainless steel. They used a Raman spectroscopy method which indicated that the pit solution contained Cr-Cl complexes but no Fe-Cl or Ni-Cl complexes were found. Hakkarainen [41] also studied the concentrated metal chlorides of growing corrosion pits by dissolving stainless steel (AISI 304 or AISI 316) into 10 M HCl which resulted in finding a critical minimum concentration for dissolution to passivation process below this critical concentration.

The oxidation state of different alloying elements has been assumed as Fe^{2+} , Cr^{3+} and Ni^{2+} by researchers [19, 20, 27, 42] studying the dissolution kinetics of stainless steel. Laycock and White [43] also used the same oxidation states in the simulation of single pit propagation in stainless steel (Fe-18Cr-8Ni) under potentiostatic conditions. These oxidation states are of interest in calculating the average charge of dissolved metal ions (z) in stainless steel which was mainly calculated as 2.2 in the modelling of stainless steel pit propagation [43]. However, the oxidation state of iron species has never been studied using X-ray spectroscopy especially by the XANES technique which is one of the most powerful techniques in determining the oxidation state.

2.7. Role of Mo in stainless steel corrosion behaviour

The beneficial effects of molybdenum in improving the corrosion resistance of stainless steel are very well known [14, 26, 44-49]. There are different mechanisms proposed to explain this behaviour. It has been suggested that molybdenum can affect the chemistry of the passive film [49-56]. Habazaki et al. [50] studied the effect of addition of molybdenum to Fe-Cr-P-C alloys and reported the improvement of passivation ability in 6 M HCl solution. Hashimoto et al. [51] have reported the formation of molybdenum oxide as a passive layer in 1 M HCl which decreases the active dissolution current. It has been suggested that; Mo can decrease the dissolution rate of stainless steel by blocking the interface with a Mo-containing species at the dissolving interface [14, 26, 44, 45, 50, 51, 57]. Goetz and Landolt [44] studied the dissolution of Cr-Mo alloys in chloride media and reported Mo-enrichment at the dissolving interface. Newman et al. [14, 45] have also studied the effect of molybdenum on dissolution and passivation behaviour of Fe-Cr-Ni-Mo alloys and suggested the presence of a

Mo sub-monolayer at the dissolving interface in HCl solutions. Kimura and co-workers [13], have made some in situ measurements on Mo species inside an artificial pit of stainless steel (Fe-18Cr-20Ni-5Mo) using X-ray absorption spectroscopy. Their experiments were carried out in LiCl and LiBr solutions at constant potential of 0.8 V (Ag/AgCl) and suggested the presence of molybdate ions (MoO_4^{2-}) that inhibit the corrosion of stainless steel.

2.8. Localised corrosion of titanium

2.8.1. Introduction

Titanium alloys are highly resistant to corrosion owing to the presence of a thin passive oxide layer (TiO_2) which is highly resistant to dissolution. Because of this, titanium alloys are commonly used in for biomedical implants. However, a number of cases have been observed where titanium alloys corrode in the body [58-60]. The passive oxide film on titanium has been very well studied. Early investigations by Mathieu [61, 62] and Quinn [63] reported the TiO_2 as the passive layer by using AES [61, 63] and later studies by Kelly and Mathieu showed the presence of TiO_2 oxide layer in aqueous solutions [61, 64, 65]. Further work on passivation of Ti in chloride-containing solutions has been carried out by Kelly [65-67] and Nishimura and Kudo [64].

2.8.2. Pitting corrosion of Ti

Relatively few investigations on the pitting corrosion of titanium have been reported. Early studies by Dugdale and Cotton [68] and Beck [17, 18] on pitting corrosion of titanium showed that titanium alloys are vulnerable to pitting corrosion in bromide, chloride and iodide solutions. When titanium is subjected to halide solutions, at a potential that is dependent on

the halide solution (chloride 12 V, bromide and iodide 2-3 V), the oxide film breaks and pitting corrosion occurs. Casillas et al. [69, 70] and Garfias-Mesias et al. [71, 72] have investigated the pitting corrosion of titanium using SECM for imaging the microscopic sites in bromide solutions and found evidence of micron sized pits. Also, Burstein et al. [73] and Jiang et al. [74] have investigated the pitting behaviour of titanium and reported the metastable pitting in Ringer's and chloride solutions but not propagating pits. Ringer's solution is a physiological fluid to simulate the human body conditions. Generally, Ringer's solution is consisting of NaCl, CaCl₂, KCl and NaHCO₃ salts dissolved in distilled water [75, 76]. BSA (bovine serum albumin) is also a protein based solution which is used as a model protein to simulate the human body environment [77]. According to these studies of titanium pitting corrosion conditions, it is very unlikely that pitting corrosion should occur in the environment in human body.

2.8.3. Crevice corrosion of titanium

Crevice corrosion is one of the most common types of localised corrosion. Crevice corrosion is well known with changes in local chemistry within the crevice. Shoesmith and co-workers [78-80] have studied the crevice corrosion of titanium alloys reporting the crevice initiation at 65°C. Other studies of crevice corrosion on titanium alloys have shown that these alloys do not corrode by crevice corrosion mechanism below 70°C [81, 82]. Crevice corrosion of titanium normally only occurs in static aggressive solutions at high temperatures. It has been suggested that the oxide film degrades by the process which is shown in Figure 2.10 at low and high temperatures [79].

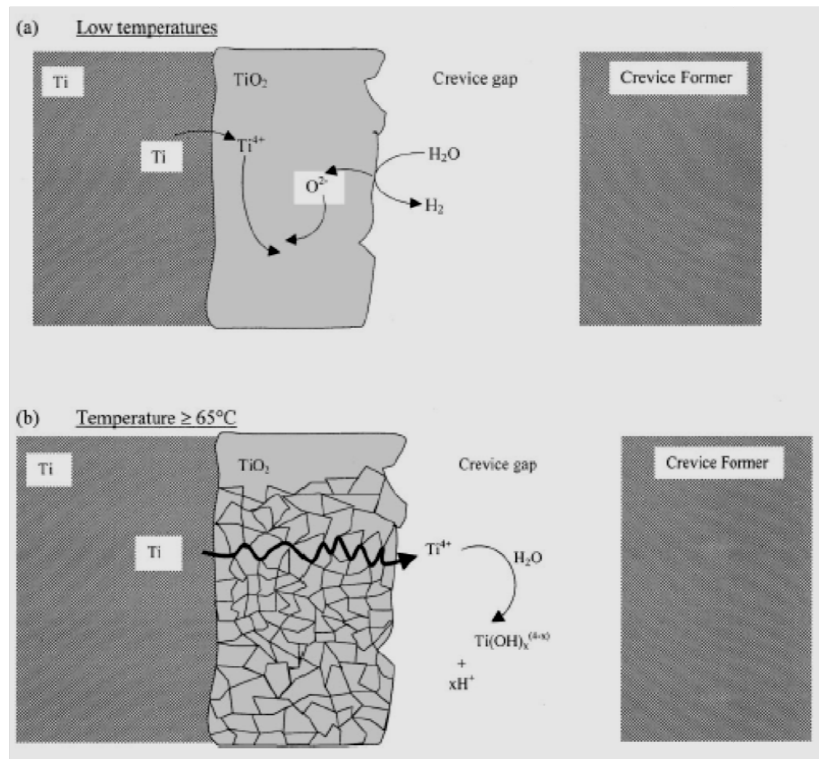


Figure 2.10 Schematic diagrams illustrating the processes occurring within a crevice at (a) low temperature, and (b) temperatures greater than 65°C . At low temperatures, pit growth predominates and passivity is maintained. At higher temperatures, film breakdown/recrystallisation processes occur leading to cation hydrolysis and the development of acidity within the creviced site [79].

2.8.4. Mechanically assisted crevice corrosion

Although corrosion of titanium alloys in crevices does not happen below 65°C [78-80], crevice corrosion can occur at low temperatures if there is any micro-motion between the two surfaces in a crevice. This process will lead to removal of the oxide passive layer and exposure of the active surface of titanium alloy to corroding environment [58, 59]. This type of corrosion, which happens under mechanical loading and movement, is also sometimes referred to as mechanically-assisted crevice corrosion (MACC) [83].

2.8.5. Artificial pits of titanium

Artificial pits have been little studied for titanium corrosion. The initial investigations by Beck established titanium's susceptibility to pitting corrosion in aqueous solutions that contains bromide, iodide and chloride [17, 18]. He used a qualitative model to describe the reactions in the pit. He also studied the pitting potential stability versus the pit depth and showed that pitting potential increases with pit growth. The experiments were carried out over a range of different potentials. The pitting potential was reported as 0.9 V (vs. Ag/AgCl) in bromide solution and minimum potential was reported 6 V (vs. Ag/AgCl) to sustain the pit stable at 1 mm depth and 30 V (vs. Ag/AgCl) for 8 mm pit depth in 6 M HCl [17].

2.8.6. Pit chemistry

Titanium has four valence electrons. The most stable and common oxidation state is Ti^{4+} and the other oxidation states are quite readily oxidized to Ti^{4+} by air, water or other reagents. There is an active-passive transition for titanium [65-67, 84]. Armstrong et al. [85] identified Ti^{3+} as the active state in HCl dissolution product in H_2SO_4 solution.

The valence for titanium following the dissolution of titanium foil in bromide, chloride and iodide solutions was reported by Beck to be Ti^{4+} from weight loss of specimens and the integration of current over the time of the experiments. There is evidence of the production of some white precipitates in the solution which are related to formation of TiO_2^+ or TiO_2 [17].

A number of experiments were also done by mixing Ti^{3+} and Ti^{4+} species in sulphuric acid to study the oxidation and reduction of titanium species [65-67, 86, 87]. Kelly and Cserenyak found the mixed oxidation state of Ti^{3+} and Ti^{4+} in sulphate solutions and found the same evidence in chloride solutions [65-67, 86, 87]. Thomas and Nobe reported that Ti^{3+}

accelerated the anodic dissolution of titanium in both the active and passive region in H_2SO_4 solutions [84]. Ti^{+2} species are limited to some solid compounds such as hydride TiH_2 and halides such as TiF_2 and TiCl_2 [88]. The potential-pH diagram of titanium shows the possible stable aqueous phases at different potentials as shown in Figure 2.11.

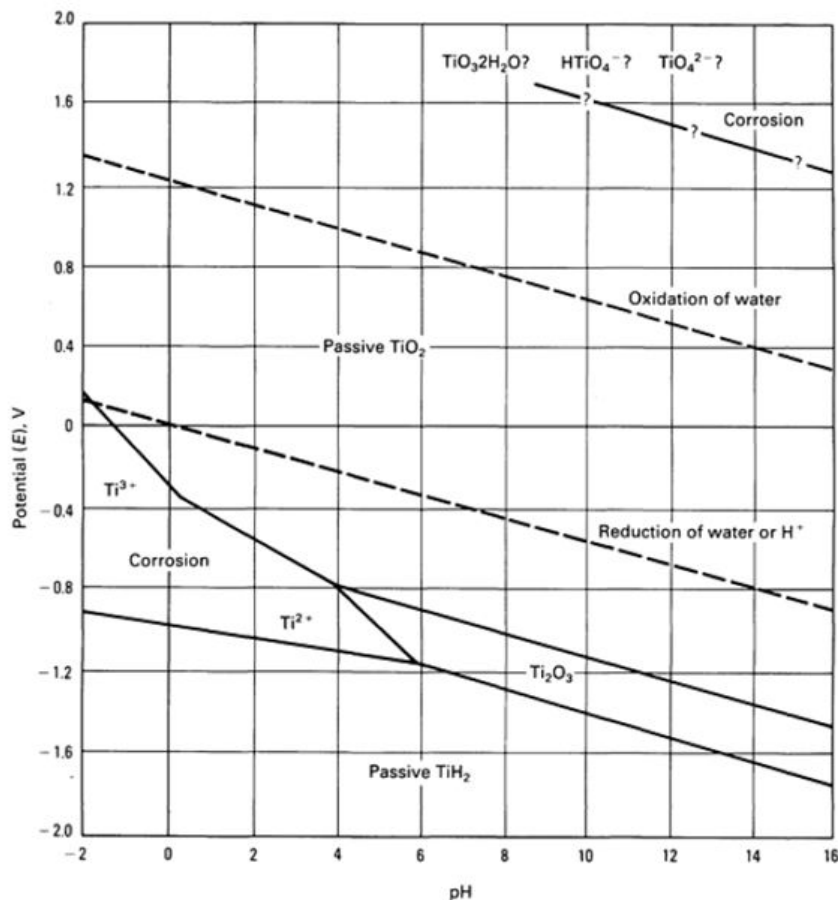


Figure 2.11 Pourbaix (potential-pH) diagram for the titanium-water system at 25 °C (77 °F) [89]

In summary, it is unlikely to find Ti^{2+} in solutions. Titanium solution species can be found in the Ti^{3+} form in sulphate solutions and the most likely oxidation state of titanium in chloride solutions is 4+.

2.9. Corrosion of titanium in the body

2.9.1. Titanium alloys and microstructure

Titanium has two crystal structures: α phase with the hexagonal closed-pack structure (hcp), and β phase with the body centred cubic (bcc) structure. Addition of alloying elements to titanium stabilises the α or β phase [60]. Titanium alloy microstructures are generally divided into α , near α , $\alpha + \beta$ and β alloys [60, 90-93].

Aluminium and oxygen stabilise the α -phase. Commercially pure titanium (CP-Ti) is the most important type of α -phase alloy and has low concentration impurities of oxygen and iron and has long been used for dental implants in which lower strength is required. CP-Ti alloy (ASTM Grades 1-4) usually undergoes a forging, hot rolling and heat treatment process to form a single α -phase [90, 92]. Titanium alloys containing 4-6% of β stabilisers generally form an $\alpha + \beta$ alloy. Ti-6Al-4V is the most commonly used alloy among the titanium alloys.

2.9.2. Titanium alloys for biomedical applications

Titanium alloys have excellent corrosion resistance in the body environment and a lower strength and density compared to stainless steel and cobalt alloys, which is the main reason for use in biomedical applications [91, 94]. Commercially pure titanium (CP-Ti) and Ti-6Al-4V alloy are the most common titanium alloys used as implants in the human body. CP-Ti has long been used for dental implants [91, 95]. Generally Ti-6Al-4V is used for joint replacement components and knee implants because of its good mechanical properties in comparison with CP-Ti [93, 96]. An example of a typical titanium screw in dental applications is given in Figure 2.12.

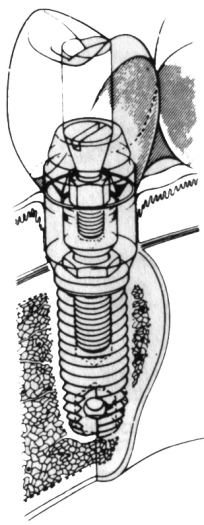


Figure 2.12 Titanium tooth-root implanted into a human jaw bone into which is screwed an artificial tooth [91].

2.9.3. Mechanisms of corrosion in the body

Hallam et al. [58] and Thomas et al. [59] demonstrated that crevice corrosion can occur where there is micro-movement of cemented hip implants. They suggested not using the cemented implants which result in early pain and inflammation in the human body.

Figure 2.13 shows a corroded cemented titanium femoral stem after implantation in the human body. The corroded parts were at the tips of implant. When the implant was removed for revision surgery, pH tests were carried out at the stem, indicating a highly acidic pH at the tip of the implant [58].

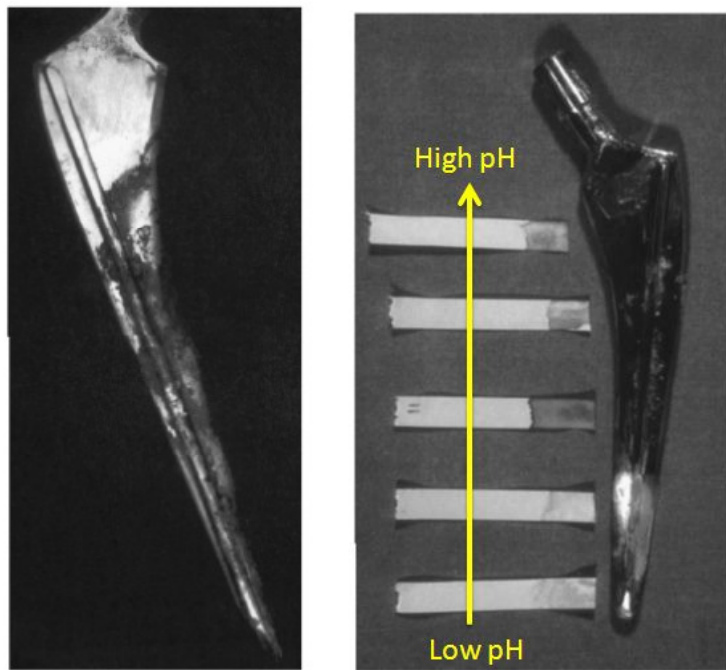


Figure 2.13 Photograph of a cemented femoral component showing corrosion (left), and photograph showing pH testing result of the femoral component (right) [58].

The observations can be attributed to fretting/MACC caused by micro-motions between the moving parts, which cause fretting of the titanium oxide layer at the surface, leading to surface exposure to the environment and corrosion processes. The hydrolysis of metal ions can be balanced by negative ions in the environment and as the pH decreases and chloride concentration increases, the corrosion of the titanium will be accelerated [58, 59, 83].

2.9.4. Effect of Ti species on human tissue

Titanium particles and species released into a human body by wear, fretting or a corrosion process have an inflammatory effect on surrounding tissues. These effects have been investigated by many researchers [58, 59, 96-99]. Sargeant et al. [99] and Jacobs et al. [96] have studied the effects of metal ion concentrations released from hip implants in the human body. Sargeant et al. [99] studied the different concentrations of ions released from titanium,

stainless steel and cobalt implants. They discussed the harmful effects of released ions which cause damage to DNA and resulting genotoxicity [99].

In some patients, pain has been reported after hip replacements with no sign of infection even if they are well-fixed. Radiography has been used to study this observation and the inflammation around the implant [58]. Figure 2.14 shows the swelling of the femur around the tip of the femoral stem of the implant, which was very well fixed during the surgery.



Figure 2.14 Radiographs of a cemented titanium total hip replacement. Left: two days after implantation and right: two years after implantation showing a swelling of the femur around the tip of the stem [58].

2.9.5. Titanium alloys biological effects and toxicity on human body

Titanium has been known as an inert and relatively biocompatible material used in medical and dental prosthesis, but there is scientific evidence that titanium alloy and its corrosion products can cause harmful reactions in the blood and osteogenic cells. Wang et al. [100] have shown that titanium particles can decrease cellular viability and increase the level of tumour suppressor proteins.

TiO_2 particles as a result of wear or corrosion process in titanium implants are of great concern because of exhibiting cytotoxicity effect of different cells. Bernier et al. [101] showed that TiO_2 particles provoked the decrease of cell size, the increase of cell granularity and DNA fragmentation.

Ti(IV) has been found as the main titanium species and the most ionic form after biocorrosion process. Titanium that released into the peri-implant tissues in the body can bind with the proteins because of their unstable nature [102, 103].

Hallab et al. [104] have also found two different molecular weight ranges of human serum proteins linked with the binding of Cr and Ti from Co-Cr-Mo and Ti implants alloy degradation which considered as potentially toxic. High molecular weight serum proteins showed greater lymphocyte bioreactivity after complexation with Cr and Ti compared to low molecular weight serum proteins.

The mechanism of how these ions effect and interact with human body is not a concern, but all these effects of titanium species and corrosion products on human body need careful consideration and more investigation.

2.10. Synchrotron methods for in situ characterisation of corrosion

2.10.1. Introduction

Localised corrosion is very difficult to study since it is associated with wet environments and many characterisation techniques must be performed in vacuum. However, synchrotron X-rays can easily penetrate through the solution environment and give information about the chemistry and present phases in the solution. Synchrotron X-ray techniques have been used to investigate the corrosion and passivation behaviour of different alloys. A number of papers have been published on characterisation of passive layers on iron, stainless steel and copper alloys using X-ray absorption spectroscopy [105-109]. X-ray diffraction has also been used to explore the passive layer characteristics on nickel [110] and iron [111] as well as X-ray fluorescence to study the dealloying processes [112] and solution composition in artificial pits [12, 113]. Recently, X-ray studies have been mainly focused on archaeological artefacts [114, 115], oil and gas corrosion [116, 117] and stress corrosion cracking [118]. In this project, the use of X-ray absorption spectroscopy, particularly XANES is explored to study the chemistry of the solution within the artificial pits of 316L stainless steel and titanium.

2.10.2. X-ray absorption spectroscopy

2.10.2.1. XANES/ EXAFS

X-rays are absorbed by atoms by a process in which an electron is ejected from a quantum core level (such as the 1s or 2p level) as shown in Figure 2.15. In the absorption process, the binding energy of the core level must be less than an incident X-ray and if the binding energy is greater than the energy of incident X-ray, the electron will not absorb the X-ray. If the

binding energy of the electron is less than the energy of x-ray, the electron may be ejected from its quantum level. Therefore, the x-ray is absorbed and any excess energy is given to an electron that is ejected from the absorbing atom [119]. Measurement of X-ray absorption spectra is often referred to as X-ray absorption spectroscopy (XAS) or X-ray absorption fine structure (XAFS).

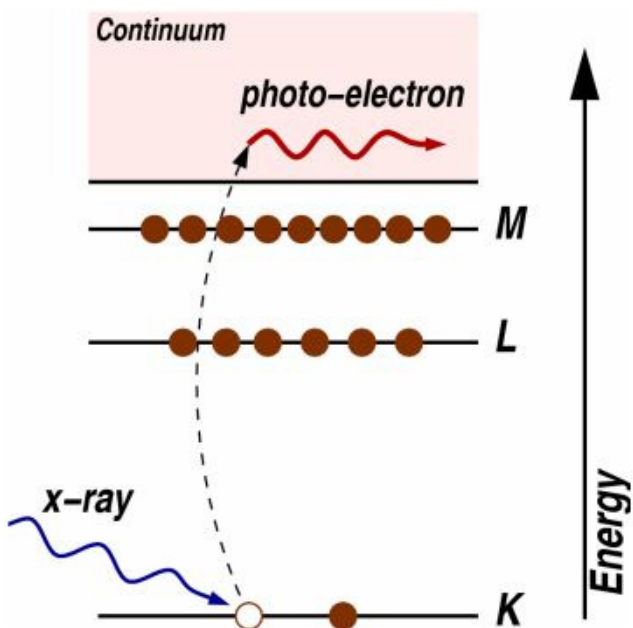


Figure 2.15 The photoelectric effect, in which an x-ray is absorbed and a core-level electron is promoted out of the atom [119].

The x-ray absorption spectrum is typically divided into two main regimes: x-ray absorption near-edge spectroscopy (XANES) and extended x-ray absorption fine structure spectroscopy (EXAFS) as shown in Figure 2.16. XANES is strongly sensitive to oxidation state and coordination (octahedral or tetrahedral) of the absorbing atom, while the EXAFS is used to determine the distances, coordination number and neighbouring atom speciation. The XANES region is normally divided into three: pre-edge, edge and above edge regions as shown in Figure 2.17.

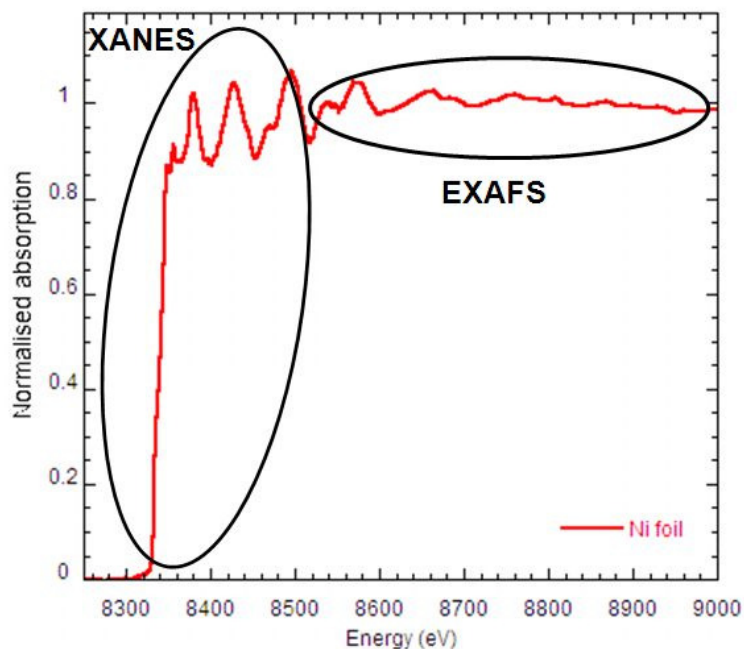


Figure 2.16 Schematic of XANES and EXAFS regions in typical nickel metal spectrum.

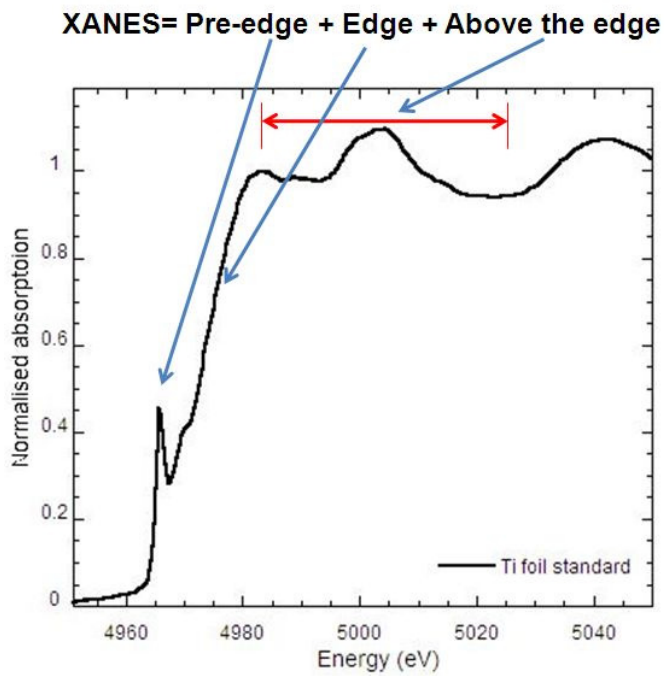


Figure 2.17 Schematic of XANES region of a typical titanium metal spectrum.

The pre-edge is particularly sensitive to local structure around the element and oxidation state. The edge energy position is a specific characteristic of the absorbing atom but is dependent on the oxidation state. As the oxidation states increases, the absorption edge position shifts to higher energies as shown in Figure 2.18 for different oxidation states of iron.

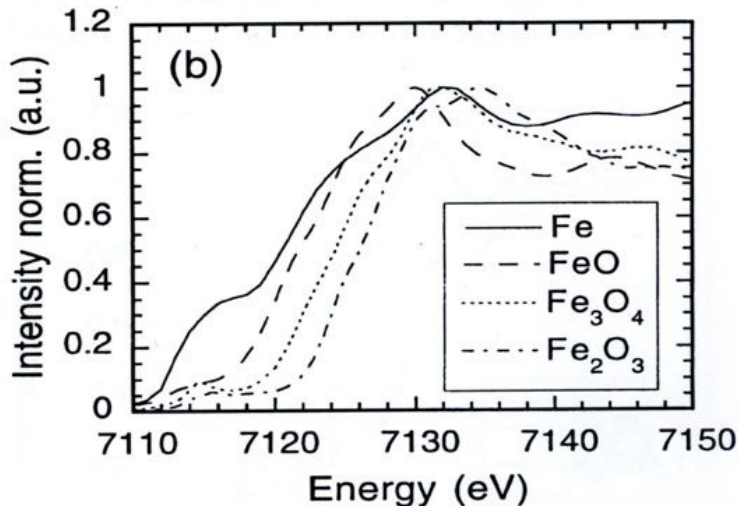


Figure 2.18 Normalised XANES spectra for Fe foil and various iron oxide powder standards [120].

2.10.2.2. Experimental modes

XAFS is typically measured in transmission and fluorescence modes. Transmission mode involves measuring the X-ray flux before and after the beam is passed through a uniform sample as shown in Figure 2.19.

In x-ray absorption, the absorption coefficient μ , gives the probability of x-rays absorption and calculated according to Beer's Law [121]:

$$I=I_0 e^{-\mu x} \quad \text{Equation 2.7}$$

Where, I_0 is the x-ray intensity, x is the sample thickness, and I is the intensity transmitted through the sample. In fluorescence mode, the incident flux I_0 and the fluorescence X-rays I_f are measured and usually the fluorescence detector is horizontally positioned at 90° to the

incident X-ray beam, with the sample positioned at 45° with respect to the beam as shown in Figure 2.20. The spectrum is generally shown as I_f/I_0 . Absorption of X-rays results in generation of a core hole as shown in Figure 2.15. The fluorescence X-rays are generated when an electron from a higher level drops down into the core hole: an X-ray is generated with an energy that is the difference between the energy of the original core hole and that of the level from which the electron drops to fill the core hole.



Figure 2.19 Transmission XAFS experimental configuration [121].



Figure 2.20 Fluorescence XAFS experimental configuration [121].

2.10.3. X-ray fluorescence mapping

XRF mapping is generally used to find the distribution of different elements and usually followed by XANES or EXAFS measurements at the sites of highest concentration of the element. XRF mapping is usually indicated by the relative intensity of x-ray fluorescence of the element with different colours showing the distribution of any elements in the sample. This method has been used in finding trace elements and their distribution in human tissues as shown in Figure 2.21 [122].

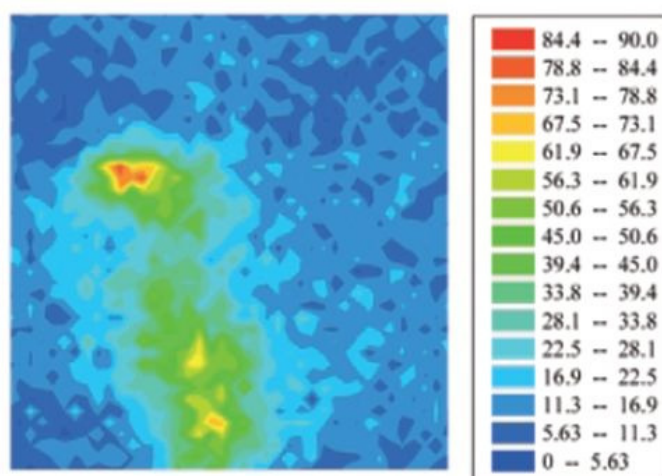
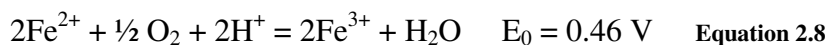


Figure 2.21 XRF imaging of iron of the temporal lobes tissue of Alzheimer's disease patient. The measurement area was $40 \times 40 \mu\text{m}$ and the step for each pixel was $1 \mu\text{m}$. The ranges of fluorescent x-ray intensity are shown in the colour scales (arbitrary unit) [122].

2.10.4. XAS studies of Fe chemistry

2.10.4.1. Fe chemistry and complexes

Iron mainly has two main oxidation states, (2+ and 3+). Iron in the oxidation state 2+ is ferrous iron and iron in the form of +3 oxidation state is ferric iron. The most common form of ions in solution are hexaaquo iron (II) $[\text{Fe}(\text{H}_2\text{O})_6]^{2+}$ and hexaaquo iron (III) $[\text{Fe}(\text{H}_2\text{O})_6]^{3+}$ [123-125]. Fe^{2+} in the absence of complexing anions oxidises in acidic environments [123]:



Also, all the species from $[\text{Fe}(\text{H}_2\text{O})_6]^{2+}$ to $[\text{FeCl}_4]^{2-}$ are known to exist in solution. Most Fe^{2+} complexes have an octahedral structure except a few tetrahedral complexes including $[\text{FeCl}_4]^{2-}$ [123]. Fe^{2+} species in chloride solutions tend to form hexa-aquo complexes with octahedral structure. Apted et al. [124] have reported this structure in the presence of 0.1 to 4 M chloride concentrations.

2.10.4.2. XAS study of iron speciation in solid compounds

Many studies have been done by using XAS to investigate the oxidation state and speciation of Fe minerals and solid compounds [126-128]. Waychunas et al. [127] has studied the variety of Fe minerals and oxides using x-ray absorption spectroscopy. They indicated that the position and intensity of pre-edge features are the main characteristics of Fe oxidation state and structure.

2.10.4.3. XAS study of iron speciation in chloride solutions

The chemical composition and speciation of iron solutions have been extensively studied using x-ray spectroscopy [124, 125, 129]. But, the chemistry of the solution inside the corrosion pits has not been widely studied using X-ray spectroscopy technique. Isaacs et al. [12] used in situ x-ray fluorescence microprobe analysis to study the salt layer and saturated solutions during dissolution of stainless steel in acidic chloride solution. The iron metal cation concentration was calculated to be 3.4 M in the salt film. They didn't consider the pit speciation and solution composition in their studies.

X-ray absorption near edge structure (XANES) particularly has been used to investigate the oxidation state and presence of chloro complexes in iron solutions at different chloride concentrations and temperatures [129, 130]. Apted et al. [124] have studied Fe^{2+} and Fe^{3+} species in chloride environments indicating octahedral coordination of ferrous ions as a hexa-aquo complex in the range of 0.1 to 0.4 M chloride concentration. Benfatto et al. [125] have also studied Fe^{2+} and Fe^{3+} species in water which showed a clear difference in white line (maximum absorbance) shape between $\text{Fe}(\text{H}_2\text{O})_6^{2+}$ and $\text{Fe}(\text{H}_2\text{O})_6^{3+}$ as shown in Figure 2.22. The Fe^{2+} spectrum shows a sharp peak above the edge while Fe^{3+} has a broader peak followed by a shoulder (A) which is clearly different from Fe^{2+} .

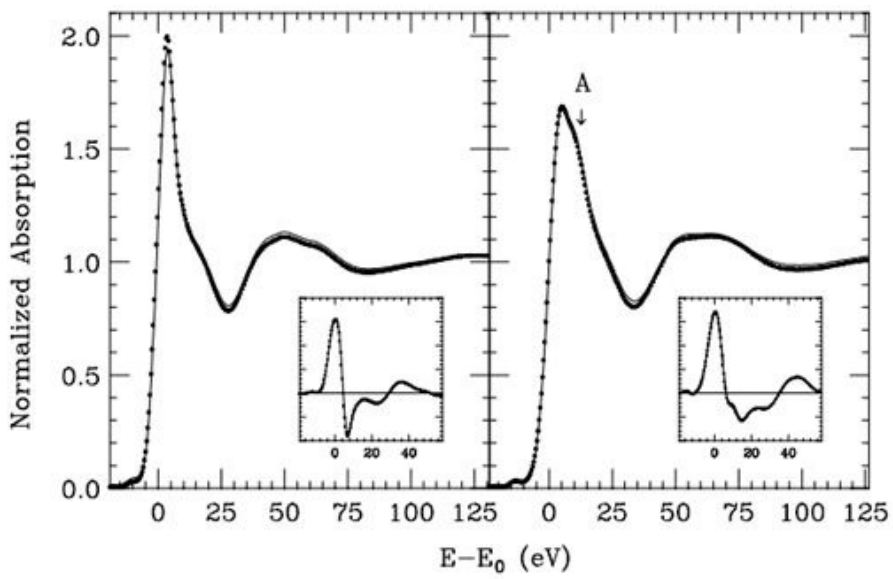


Figure 2.22 Comparison of the normalised Fe K-edge XANES spectra of the $\text{Fe}(\text{H}_2\text{O})_6^{3+}$ (right) and $\text{Fe}(\text{H}_2\text{O})_6^{2+}$ (left) complexes at two different pHs: Fe^{2+} pH, 1 (dots) and 6 (solid line); Fe^{3+} pH, 1 (dots) and 2 (solid line). (In the inset, comparison of their derivative is shown) [125].

Testemale et al. [129] used XAS techniques to determine the coordination structure and to study the speciation of aqueous ferrous chloride complexes in acidic chloride brines over a wide range of conditions (25-450°C, 500 bar, 0.5-12 m chloride molality). They showed that increasing the temperature or chloride concentration will decrease the white line intensity and increase the pre-edge intensity. These changes are attributed to structural change from octahedral to tetrahedral. However, temperature has more effect on changing the white line and pre-edge intensity as shown in Figure 2.23. There are also some features in the post edge region which indicated structural changes in Fe^{2+} complexes from octahedral to tetrahedral due to heating or increase in chlorinity [129].

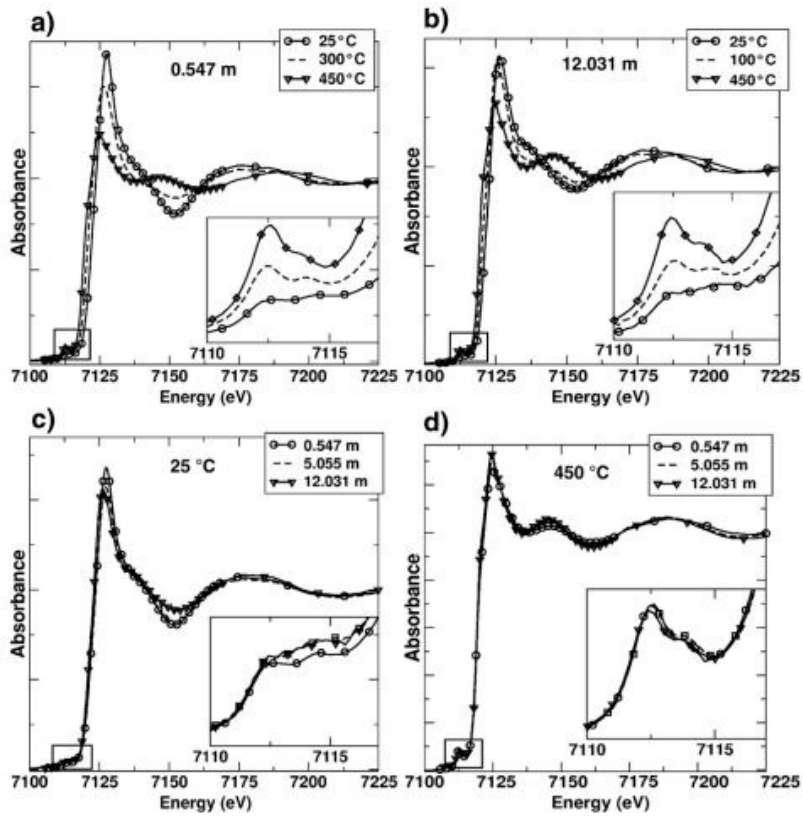


Figure 2.23 Normalised Fe K-edge XANES spectra of solutions measured a) chloride concentration 0.547 m, b) chloride concentration 12.031 m, c) temperature 25 °C, d) temperature 450 °C [129].

The increase of the intensity of the pre-edge region was explained by a transition from an octahedral species to a tetrahedral species associated with the reduction of two components distances from 2 eV to 1.5 eV as shown in Figure 2.24. It can be seen that the intensity of the white line (maximum absorbance) is reduced and the edge position shifted to lower energy is attributed to a structural transition to tetrahedral due to 1s-4p dipole transition which is the case for tetrahedral structures [126].

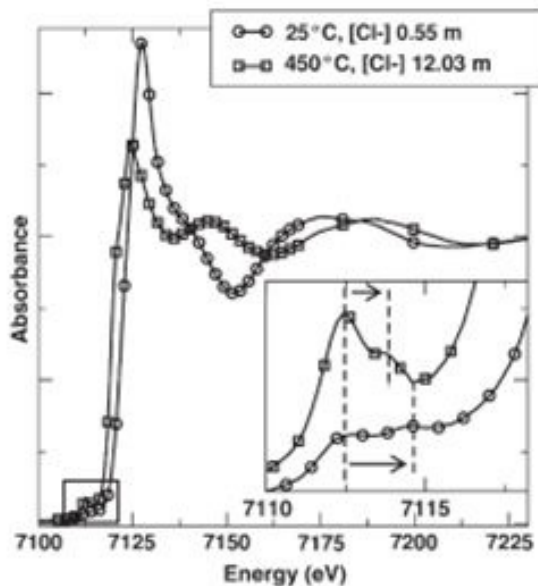


Figure 2.24 Normalised Fe K-edge XANES spectra of 2 end-members ($25\text{ }^{\circ}\text{C}/0.547\text{ m}$ chloride concentration and $450\text{ }^{\circ}\text{C}/12.031\text{ m}$ chloride concentration). The inset corresponds to the pre-edge region [129].

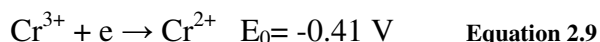
Liu et al. [130] have also observed the same transition from octahedral to tetrahedral structure by studying the Fe(II) and Zn(II) chloride complexes in a wide range of chloride concentrations and lower temperatures (up to $150\text{ }^{\circ}\text{C}$) compared to Testemale et al's [129] experiments.

2.10.5. XAS studies of Cr chemistry

2.10.5.1. Cr chemistry and complexes

The main oxidation states of chromium are 2, 3 and 6. The Cr^{2+} aqua ion does not have a strong complex in aqueous environments and easily undergoes hydrolysis and should be protected from air otherwise it oxidises to Cr^{3+} [131].

The Cr(II) ion has a bright blue colour and can be obtained by dissolving pure chromium in dilute acids or by reducing Cr(III) solutions electrochemically or with Zn/Hg [131]:



Cr(III) complexes have been of more greater interest due to the inertness of chromium species in aqueous environments; they remain stable for a long time in the solution and have been studied in chloride environments [132-134]. Chromium(III) chloroaquo complexes can be obtained by dissolving salts in water or HCl [133, 135]. $[\text{CrCl}_3(\text{H}_2\text{O})_3]^{3+}$ can be formed by dissolving $\text{CrCl}_3 \cdot 6\text{H}_2\text{O}$ salt in concentrated HCl solution. $[\text{CrCl}(\text{H}_2\text{O})_5]^{2+}$ and $[\text{Cr}(\text{H}_2\text{O})_6]^{3+}$ can also be obtained by dissolving the chromium salt in water [135]. When the salt is dissolved in water, the solution contains mainly $\text{Cr}(\text{H}_2\text{O})_4\text{Cl}_2^+$, then changes and results in the formation of $\text{Cr}(\text{H}_2\text{O})_5\text{Cl}_2^+$ and $\text{Cr}(\text{H}_2\text{O})_6^{3+}$ due to a replacement of the chlorine with water which occurs in two stages following each other [133] :



Cr (VI) solution complexes are mostly in the form of CrO_4^{2-} and $\text{Cr}_2\text{O}_7^{2-}$ which can be obtained by dissolving CrO_3 and $\text{K}_2\text{Cr}_2\text{O}_7$ respectively. CrO_4^{2-} can be obtained by dissolving CrO_3 in basic solutions above pH 6 and $\text{Cr}_2\text{O}_7^{2-}$ can be formed by dissolving $\text{K}_2\text{Cr}_2\text{O}_7$ salt in 6 M HCl [131] .

2.10.5.2. XAS study of chromium speciation in chloride solutions

Isaacs et al. [12] calculated the concentration of Cr^{3+} and reported 1.1 M in the salt film above the dissolving interface between metal and solution in chloride environment and Brossia et al. [40] found the CrCl^{2+} complex at high concentration of chromium and both hexaaquo complex $\text{Cr}(\text{H}_2\text{O})_6^{3+}$ and CrCl^{2+} below 1 molal chromium concentration.

Chromium species in stainless steel pits have not been studied using XANES or EXAFS techniques before but some X-ray techniques have been used to investigate metal complex

formation in solutions [133, 135]. Magini [133] used x-ray diffraction to study concentrated chromium (III) chloride solutions in equilibrium conditions and complex formation between Cr^{3+} and Cl^- ions and obtained average values of the structural parameters for the first shells of species.

Diaz-Moreno et al. [135] used EXAFS to determine the structure of Cr species in aqueous solutions. Figure 2.25 shows the XANES spectra of the solids with known structure and coordinated atoms. The local structure of each solid compound was explained as an octahedron formed by six oxygen atoms in $\text{Cr}(\text{NO}_3)_3 \cdot 9\text{H}_2\text{O}$, four oxygen atoms and two chlorine atoms in $\text{CrCl}_3 \cdot 6\text{H}_2\text{O}$ and six chlorine atoms in anhydrous CrCl_3 . In all the spectra, small similar pre-edge features and featureless edges appeared. In the hexahydrate (Figure 2.25a) and dichlorotetrahydrate (Figure 2.25b), there were two distinct peaks at 5 and 15 eV after the edge with the same intensity for the second peak and higher intensity for the first peak of the hexahydrate. In contrast, a wide and less intense peak was observed for the hexachloro compound as shown in Figure 2.25c [135].

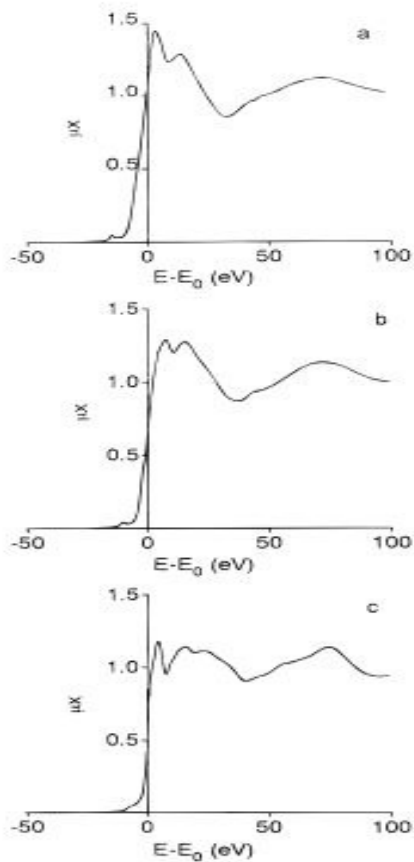


Figure 2.25 Normalised absorption spectra at the Cr K-edge, XANES region of the following solid compounds:
(a) $\text{Cr}(\text{NO}_3)_3 \cdot 9\text{H}_2\text{O}$, (b) $[\text{CrCl}_2(\text{H}_2\text{O})_4]\text{Cl} \cdot 2\text{H}_2\text{O}$, (c) CrCl_3 [135].

The XANES spectra for aqueous solutions of Cr species are shown in Figure 2.26. The small pre-edge peaks appeared in four species, and the peaks above the edge at 5 and 15 eV showed different intensities in the hexaaquo and monochloro species (Figure 2.26 parts a and b), and the peaks were merged together in dichloro and trichloro species (Figure 2.26, parts c and d). Figure 2.26 showed a systematic trend in the overall shape of the peak above the edge when the water molecules were replaced by chlorine atoms resulting a broader peak in the trichloro species [135].

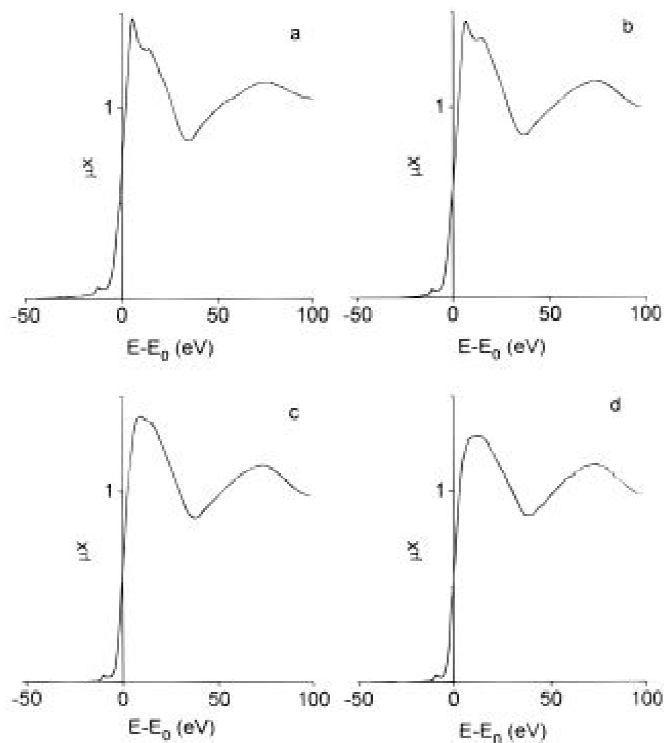


Figure 2.26. Normalised absorption spectra at the Cr K-edge , XANES region, of the following species in aqueous solution (a) $\text{Cr}(\text{H}_2\text{O})_6^{3+}$ (0.01 m) (b) $\text{CrCl}(\text{H}_2\text{O})_5^{2+}$ (1 m) (C) $\text{CrCl}_2(\text{H}_2\text{O})_4^+$ (0.005 m) (d) $\text{CrCl}_3(\text{H}_2\text{O})_3$ (0.005) [135].

2.10.6. XAS studies of Ni chemistry

2.10.6.1. Ni chemistry and complexes

Nickel compounds are often hydrated with the characteristic colour of blue or green [136]. Nickel has different oxidation states from 1+ to 4+ but the most important oxidation state is 2+. The Ni (II) ion forms different complexes on dissolving nickel dihalides in water [136, 137]. In highly concentrated pure NiCl_2 solutions, the main present species in acidic conditions are $[\text{Ni}(\text{H}_2\text{O})_6]^{2+}$ and $[\text{Ni}(\text{H}_2\text{O})_5\text{Cl}]^+$ ions [137]. Angel et al. [138] studied the Ni(II) aqueous solutions in different chloride concentrations up to 320 °C and found that $[\text{Ni}(\text{H}_2\text{O})_6]^{2+}$ species are replaced by Cl^- ions to give Ni-Cl complexes.

2.10.6.2. XAS study of nickel speciation in chloride solution

Nickel speciation and chemistry has not been studied very well by using x-ray techniques. Waizumi et al. [139] used X-ray diffraction to study the Ni^{2+} species in chloride aqueous solutions and reported bond distances between Ni and coordinated atoms. Sridhar et al. [33] used Raman spectroscopy which was not able to measure any nickel chloro complexes at 0.5 M HCl solution.

In crystalline NiCl_2 , the structure is octahedral coordinated with six chloride ions but in solid $\text{NiCl}_2 \cdot 6\text{H}_2\text{O}$, the first Ni(II) coordination sphere contains only four water molecules and two chloride ions [140]. Nickel coordination changes in aqueous solutions when the solid compound dissolves in the solution environment. The Ni^{2+} is well known to be coordinated with six water molecules in aqueous solutions [141].

Recently, D'Angelo et al. [141, 142] have used XANES and EXAFS to study the Ni^{2+} speciation in aqueous solutions by dissolving 0.2 M $\text{Ni}(\text{NO}_3)_2$ in solution. They compared the experimental results with theoretical calculations for $\text{Ni}(\text{H}_2\text{O})_6^{2+}$. In Figure 2.27, it can be seen that there is a very good agreement between the theoretical calculations for the $\text{Ni}(\text{H}_2\text{O})_6^{2+}$ spectra compared with solution spectra obtained from $\text{Ni}(\text{NO}_3)_2$ dissolution in water.

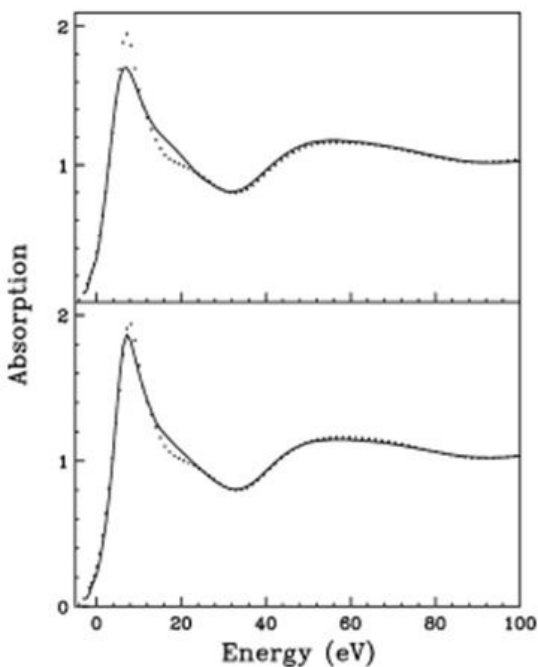


Figure 2.27 Upper panel: Comparison between the averaged theoretical XANES spectrum including the first shell (solid line) of Ni^{2+} in water solution. Lower level: Comparison between the average theoretical XANES spectrum including the first and second shell (solid line) and the experimental data (solid line) of Ni^{2+} in water solution [141].

2.10.7. XAS studies of Mo chemistry

Many studies have been done on characterisation of molybdenum species in aqueous solutions, mainly XANES and EXAFS widely used to study the molybdenum structure and oxidation states [13, 143-146]. Cramer et al. [143] have studied the molybdenum species in aqueous solutions as shown in Figure 2.28. Yokoi et al. [145, 146] studied the Mo(V) and Mo(VI) solid and solution compounds using XANES and EXAFS. They explained the structure of Mo(VI) as MoO_2^{2+} ions in low HCl concentrations (1 and 2 M) and chloride complex in higher concentrations of HCl (4 and 6 M). They also found μ -oxo dimer of Mo(V) (Mo-O-Mo) in 4.5-6 M HCl solutions.

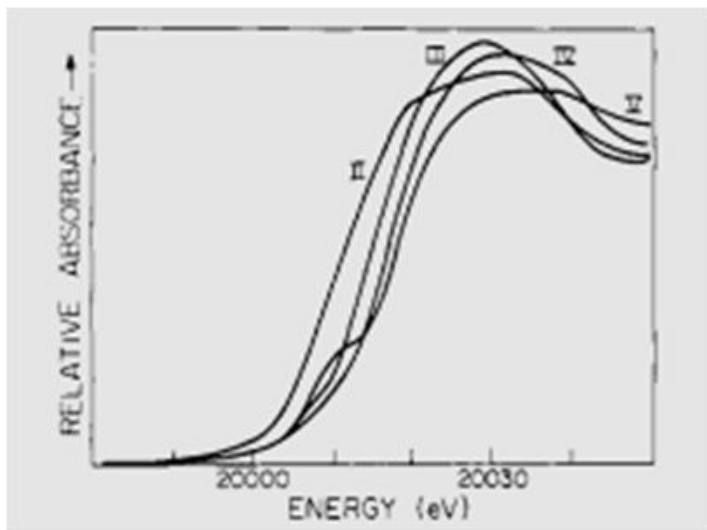


Figure 2.28 Absorption edge spectra for aqueous molybdenum ions: Mo (II) in 1 M trifluoromethanesulfonic ; Mo(III) in 3 M methanesulfonic acid; Mo (IV) in 4 M methanesulfonic acid; Mo (V) in 3 M HCl [143].

Studies of the Mo K edge for MoCl_5 dissolved in HCl solutions of different concentrations ranging from 1.7-9.4 M HCl have been carried out by Jalilehvand et al. [144]. They carried out a set of XANES measurements showing a shoulder which was clearly defined in low concentrations in which single and double bridged Mo-O-Mo dimers were found, compared with high chloride concentrations where mononuclear Mo species were found as shown in Figure 2.29.

Kimura et al. [13] measured the Mo K edge in stainless steel (Fe-18Cr-20Ni-5Mo) pits that were grown in 1 M LiCl and 1 M LiBr and claimed that the spectra are similar to a network of molybdate $[\text{MoO}_4(\text{H}_2\text{O})_2]^{2-}$. They suggested that formation of these networks close to the interface near the dissolving metal has an important role in the beneficial effect of Mo in the corrosion resistance of stainless steel (Fe-18Cr-20Ni-5Mo) as shown in Figure 2.30. Kimura et al. [13] used quite a large beam (0.1 mm height x 10 mm width) to measure the XANES spectra and they only used Mo (VI) standards for comparison with the pit results.

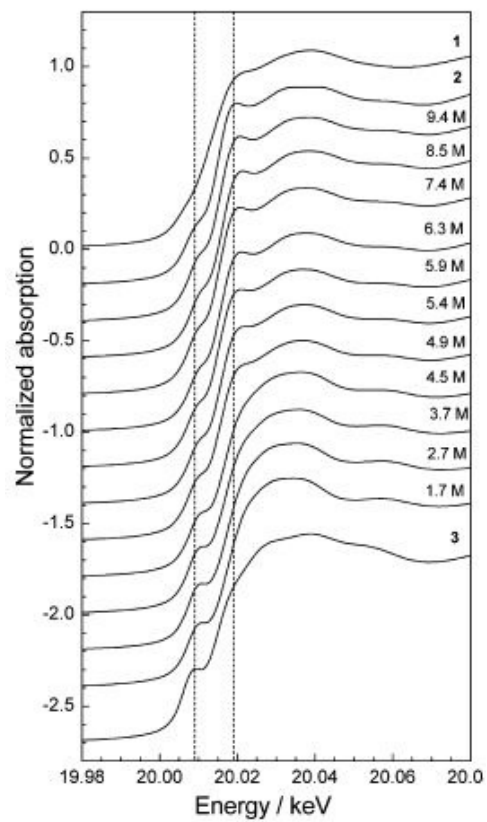


Figure 2.29 Normalized Mo K-edge XANES spectra for MoCl_5 in 1.7-9.4 M HCl solutions and the solid compounds [144].

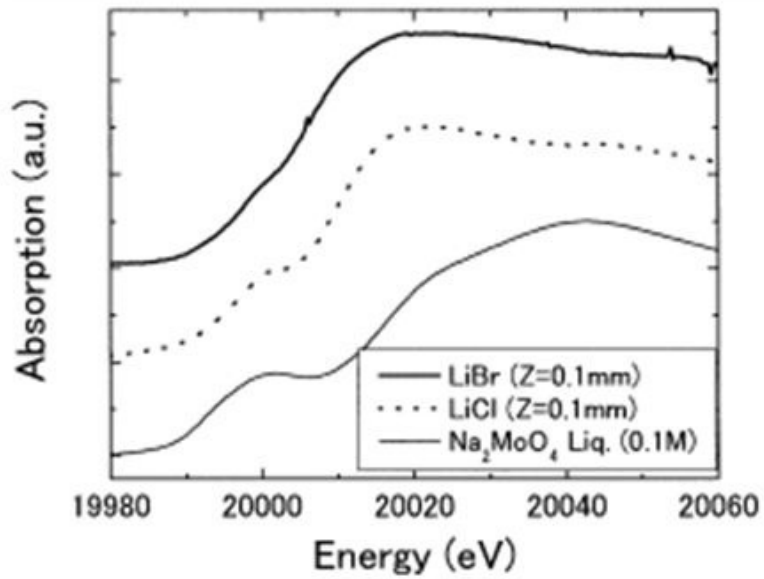


Figure 2.30 XANES spectra at Mo-K edge of in situ measurement for LiCl, LiBr and Na_2MoO_4 solution [13].

2.10.8. XAS studies of Ti chemistry

2.10.8.1. XANES study of titanium species

XANES study of the titanium K-edge has been extensively used to find out information about the electronic state and local environment in different compounds of titanium. Farges et al. [147-151] has studied a wide range of titanium compounds as shown in Figure 2.31. Many other researchers have also studied the titanium compounds mainly focused on pre-edge area of XANES spectra [151-155].

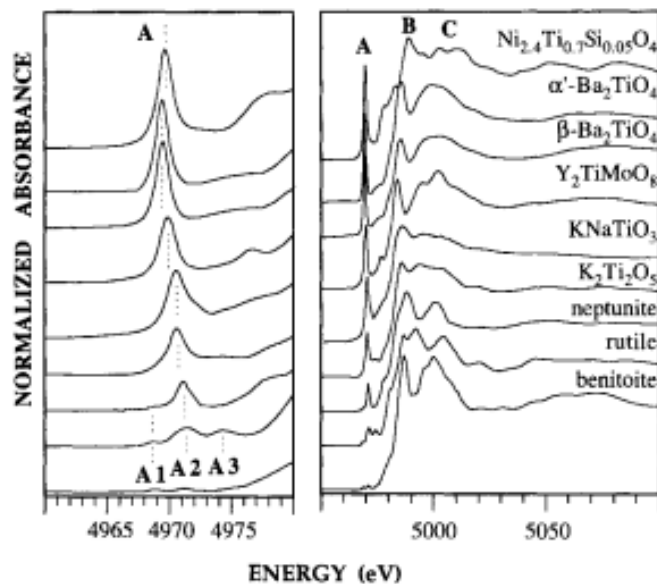


Figure 2.31 Normalized Ti K-edge XANES spectra for selected Ti-bearing model compounds containing Ti^{4+} , Ti^{5+} and Ti^{6+} (right), Detail of the normalized pre-edge feature (left) [147].

XANES measurements of Ti^{3+} species in solid compounds has been less commonly studied and is restricted to some oxides such as Ti_2O_3 and $\text{NaTiSi}_2\text{O}_6$ which show ~ 2 eV energy shift of the edge towards lower energies relative to Ti^{4+} samples such as rutile and anatase (TiO_2) [154]. Figure 2.32 shows the K-edge XANES spectra of Ti^{3+} and Ti^{4+} solid compounds.

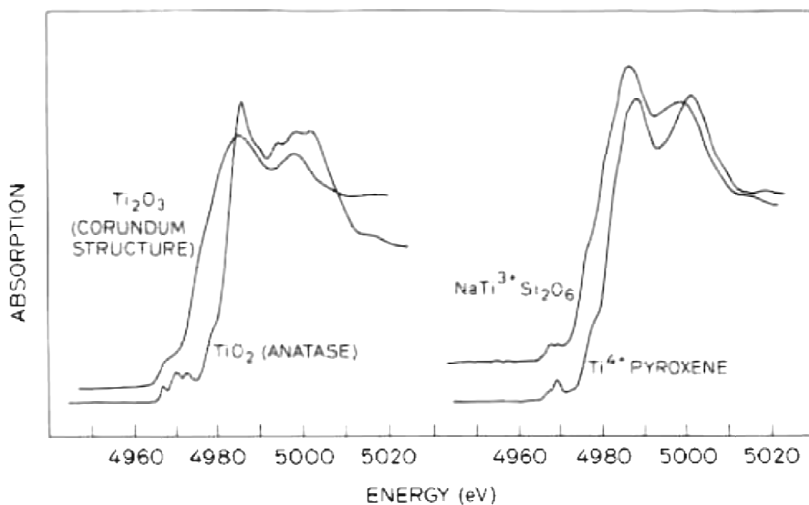


Figure 2.32 Comparison of near K-edge spectra of Ti^{3+} and Ti^{4+} structures[154]

XANES study of Ti species in solution is not well understood and is limited to some investigations using a methyl acrylate- TiCl_4 complex [156] and TiCl_3 [157] as a doping material for NaAlH_4 (Figure 2.33) [156, 157]. The main difference between TiCl_3 and TiCl_4 XANES spectra is the absence of pre-edge peak in TiCl_3 spectrum as shown in Figure 2.34.

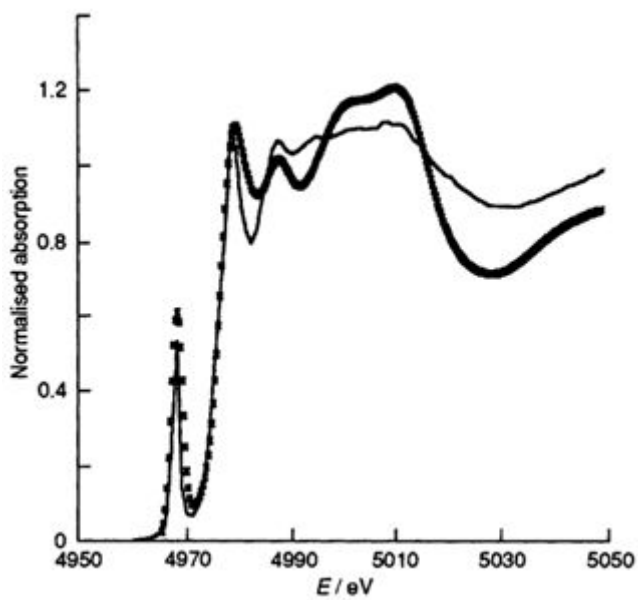


Figure 2.33 Comparison between experimental (---) and theoretical (xxx) XANES spectra of TiCl_4 [156]

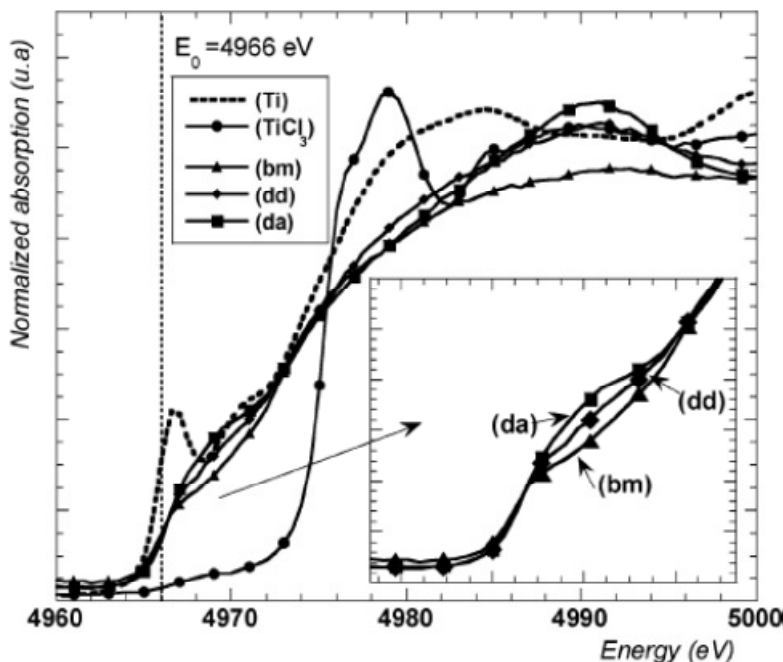


Figure 2.34 Normalised Ti K-edge XANES spectra of NaAlH_4 doped with 5 mol % of TiCl_3 at different stages. Samples are ball-milled (bm), after 2.6 wt % of hydrogen was released at 150°C under a residual hydrogen pressure of 0.3 bar (dd: dehydrogenation) and after 2.3 wt % of hydrogen was reabsorbed at 100°C under 100 bar of hydrogen (da: hydrogenation). For comparison the spectra of TiCl_3 as received (TiCl_3) and pure Ti metal are presented (Ti). The vertical dashed line at 4966 eV corresponds to the first inflection point in the Ti K-edge XANES spectrum of the pure metal [157].

2.10.8.2. Pre-edge features for titanium

Pre-edge features found at the base of the absorption edge provide valuable information about the coordination of titanium species. In tetrahedral coordination, Ti metal K-edge XANES spectra show a strong pre-edge peak, while in octahedral coordination there is a very weak or no pre-edge absorption feature [147-151].

Farges et al. [147, 150] have studied Ti coordination by studying the pre-edge features defining three regions corresponding to tetrahedral (four-fold), square-pyramid (five-fold) and octahedral (six-fold) coordinated Ti. They studied a large number of mineral compounds with known structures and categorised the minerals with different coordination numbers into three regions. Figure 2.35 shows a series of Ti K-edge spectra for some titanium model compounds

in which Ti is located in 4, 5 and 6 coordinated sites. Pre-edge areas are different for any coordination as they have different pre-edge height and position.

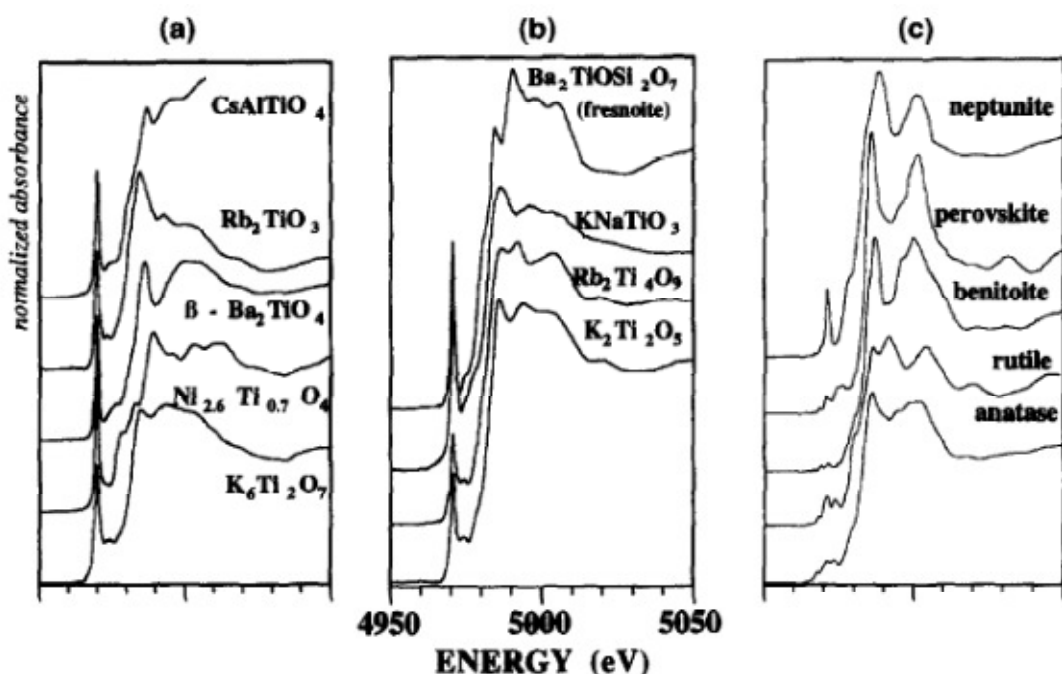


Figure 2.35 Ti K-edge XANES spectra of titanium model compounds containing (a) 4 coordinated, (b) 5 coordinated and (c) 6 coordinated Ti [151].

The experimental pre-edge features have the maximum height for four-fold coordinated Ti and located at lower energies by 2 eV compared to Ti six-fold coordination. Pre-edge energies and heights for five-fold Ti compounds are between the values of four-fold and six-fold coordination showing three distinct regions as shown in Figure 2.36. [150]. It was also found that maximum effect of pre-edge features is due to Ti-O bond length reduction, but the other factors, such as symmetry, coordination number and angles have the same effect [153]. Therefore, it needs very careful consideration about using Ti pre-edge peaks information to analyse Ti coordination.

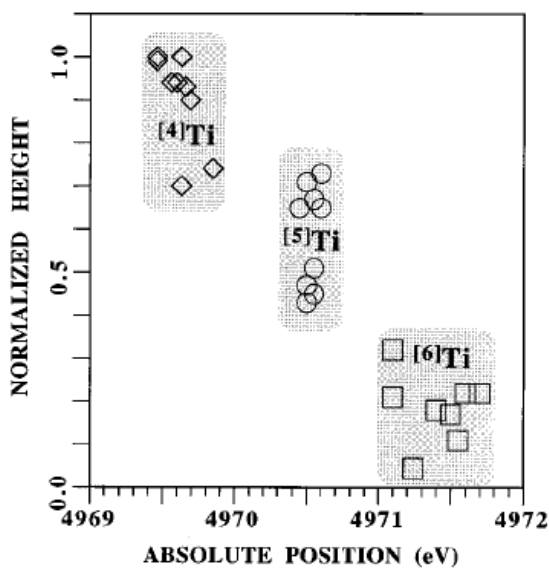


Figure 2.36 Normalised pre-edge height vs. energy position for Ti K-pre-edge features in model compounds showing three domains for four-fold, five-fold and six-fold coordinated Ti [150].

2.10.8.3. XANES study of human tissue

XANES is a very useful method to indicate the chemical state of elements, and particularly makes it possible to investigate the state of distributed Ti species in human soft tissues at low concentrations. XRF mapping can be used as preliminary method to find the image of the elemental distribution in tissues followed by XANES measurements on high intensity areas [122, 158]. XRF mapping is not the only way for in situ imaging of human cells and tissues. Radioisotope Imaging, Magnetic Resonance Imaging (MRI) and Mass Spectrometry Imaging are the other methods for studying human tissue [159].

XANES has not been widely used for studying the metallic traces in human tissues but some investigations show the evidence of metallic Ti in human tissues which is considered as debris generated from mechanical movement of implants in addition of titanium oxides species

(rutile and anatase) in tissues [158]. In some tissues, Ti k-edge XANES spectra can be the linear combination of metallic Ti and oxides as shown in Figure 2.37.

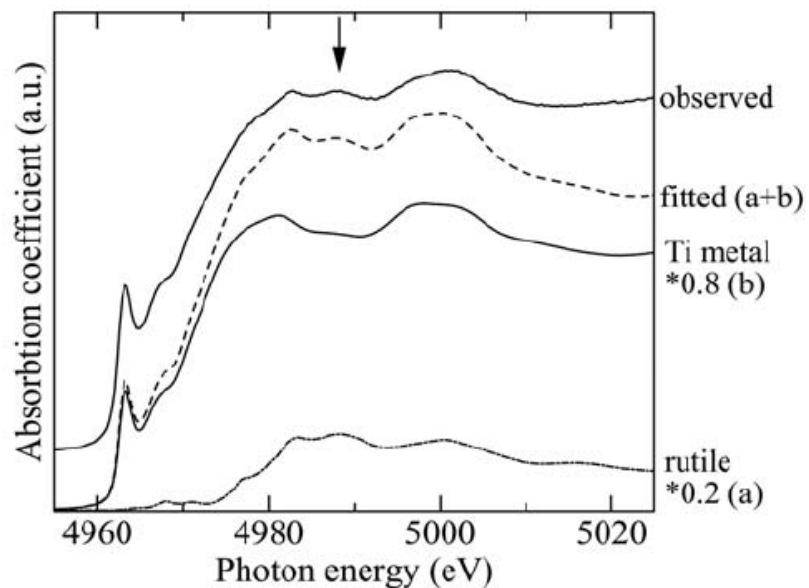


Figure 2.37 Ti K-edge XANES spectra of tissue adjacent to dental implant and a curve fitting of metallic Ti and TiO_2 [158].

2.11. Summary

Despite the fact that stainless steel and titanium are corrosion resistant materials, 316L stainless steels are susceptible to corrosion in chloride containing solutions and titanium implants are vulnerable to corrosion in the human body.

In situ XAS is a very powerful method to study the chemistry of localised corrosion sites of these alloys. However, there are relatively few in situ studies of the chemistry of localised corrosion sites. X-ray fluorescence and Raman spectroscopy have been used to characterise the chemistry of pits of stainless steel as well as XRF mapping and XANES for Ti corrosion products in human tissue. Therefore, in this work, XAS will be used to study the speciation of alloying elements Fe, Cr, Ni and Mo in artificial pits of stainless steel in comparison with reference materials of known oxidation state.

Titanium species have been studied using XANES and this has mostly been limited to titanium oxides and minerals; there is less known about the solution species. Titanium solution chemistry has not been widely studied by XAS, and no measurements have been made on artificial pits. Solution and solid titanium reference materials are needed in order to study the solution chemistry and corrosion products of titanium. In this project, XANES measurements are carried out on titanium artificial pits and standards followed by XANES measurements on human tissue in order to investigate the origin of the corrosion products found in human tissues.

3. Experimental method

3.1. Metal foils for electrochemical measurements

The working electrodes for growing the artificial pits were made from 3 mm wide strips of 50 µm foils of 316L stainless steel (Advent Materials, Oxford, UK, temper annealed, typical analysis ppm: C< 300, Si<1%, Mn<2%, Ni 10-14%, Cr 16-18%, Mo 2-3%, S<300, P<450, Fe balance) and commercially pure titanium with 99.6% purity (Advent Materials, Oxford, UK, temper annealed, analysis max values in ppm: Fe 2000, H 150, O 1800, N 300, C 800). Reference foils for calibration were 5 µm thickness iron foil with 99.5% purity (Advent Materials, Oxford, UK, temper hard, typical analysis ppm: C 1200, Mn 5000, S 500, P 500), 75 µm chromium foil with 99% purity (Advent Materials, Oxford, UK, temper annealed, typical analysis ppm: C 200, Mn 2500, Si 900, Cu 10, Fe 1600), 5 µm molybdenum foil with 99.95% purity (Advent Materials, Oxford, UK, temper annealed, typical analysis ppm: Ag < 5, Al 10, As < 1, Cr < 10, Cu 5, Fe 50, H < 1, Mn < 5, Ni < 5, O 20, P < 5, S < 5, Si < 5), 15 µm chromium foil (no information available) and 5 µm titanium foil (Advent Materials, Oxford, UK, temper hard, quality light tight, typical analysis in ppm: Fe 300, H 10, O 400, N 100, C 100).

3.2. Standards for XAS measurements

3.2.1. Metal foils for calibration

Metal foils of Mo, Fe, Cr, Ni and Ti (Advent Materials, Oxford, UK) were used as references to calibrate the energy of all measurements. Spectra from the foils were measured at the same time as sample spectra were collected in the usual procedure which places the reference foil

between the second (transmitted) and third ion chamber. Table 3.1 shows the thickness of the metallic reference foils used for calibration of XANES measurements.

Table 3.1 Reference metallic foils for calibration of XANES spectra

Reference foil	Thickness (μm)
Fe	5
Cr	15
Ni	75
Mo	5
Ti	5

3.2.2. Procedures for preparing of powder standards

Solid air-stable powder standards of Mo and Fe compounds were weighed and diluted with boron nitride (BN) powder and loaded into plastic cuvettes (Eppendorf UK Limited) with a 1 mm thick window and 2 mm path lengths, with content estimated to give an optimum edge step of 0.2-0.5. Powders of Fe, Ni, Cr and Ti compounds were ground with boron nitride (BN) and sealed between two layers of Kapton tape. Air sensitive solid standards were handled in a glove box (MBRAUN Labmaster sp) under argon gas and loaded into cuvettes in glove box. Air-sensitive samples were sealed with Parafilm and Al foil to prevent oxidation of the materials inside.

3.2.3. Procedures for preparation of liquid standards

Solution standards were prepared by weighing powder in the glove box under an argon atmosphere and then transferred into volumetric flasks, which were sealed with a rubber septum removed from the glove box. Solutions of air-sensitive species were prepared under

an argon gas atmosphere by dropwise addition of the solution (which had previously been deaerated with argon for 10 minutes) to a flask containing the powder. The solution standards were transferred into special cells or plastic cuvettes using plastic syringes with argon gas pressure and sealed as shown in Figure 3.1. This procedure was typically carried out 1h before measuring the spectrum.



Figure 3.1 Solution transfer via syringe from flask into a plastic cuvettes for Mo(V) solution.

Fe, Ni, Cr and Ti solution standards were made by adding solution dropwise to the flask containing the powders as explained above. Non-air-sensitive solutions were made and transferred via syringe into a thin-walled Teflon solution container with a 3 mm path length with Kapton windows at both sides as shown in Figure 3.2a. Air sensitive solutions were made under inert gas and transferred from the glass flask into the Teflon cell via syringe from an inlet tube under inert gas pressure until the cell was filled and the solution flowed into the outlet tube. Then, both inlet and outlet tubes were sealed to prevent the oxidation of solution. Figure 3.2b shows the cells that were used for XANES measurements of non air sensitive and air sensitive solutions of Fe, Ni, Cr and Ti.

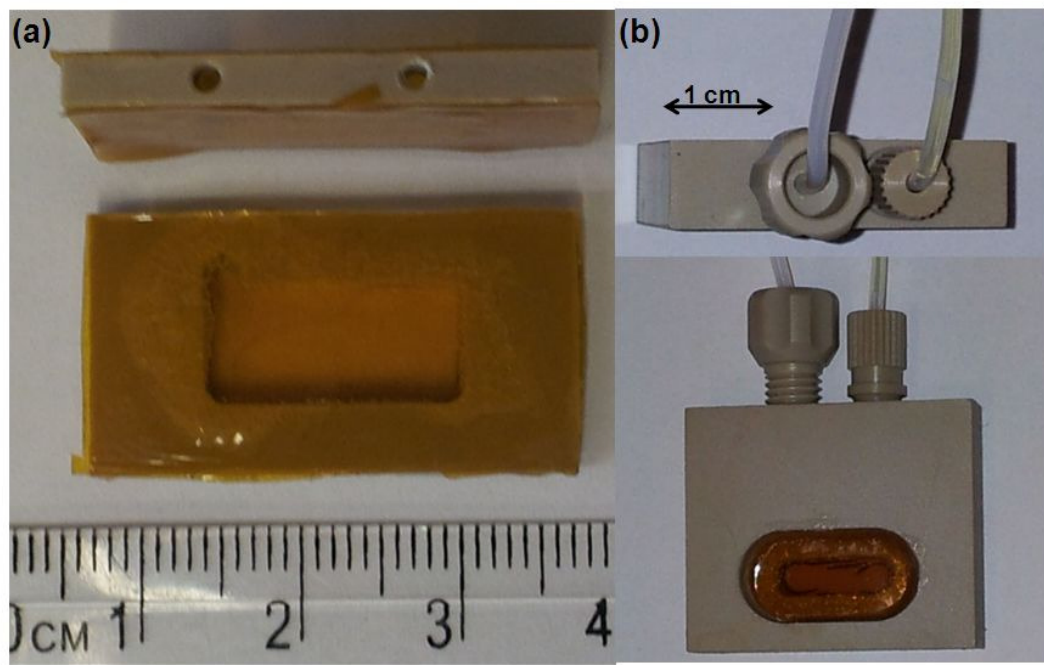


Figure 3.2 Photographs of cells that were used for Fe, Ni, Cr and Ti solutions (a) plastic cell for non air sensitive solutions, (b) plastic cell for air sensitive solutions.

3.2.4. Mo (V) preparation

135 mg of MoCl_5 powder was weighed in the glove box and transferred into a 50 ml volumetric flask in the glove box. The volumetric flask was sealed with a rubber septum removed from the glove box. Meanwhile, 6 M HCl was purged with argon for 10 minutes to remove the oxygen from the solution. The 6 M HCl solution was then added dropwise to the MoCl_5 powder via a syringe to give a 10 mM of MoCl_5 reference solution. Plastic cuvettes (10 mm x 10 mm) were sealed with Parafilm, electrical tape and a 12 mm rubber septum (Fischer Scientific) in the glove box. The cuvette was taken out of the glove box and MoCl_5 solution was transferred into the cuvette by syringe via the rubber septum, then the cuvette was placed in a glass bottle with argon flow for 10 minutes.

3.2.5. Mo (III) preparation by adding zinc powder to Mo (V)

An Mo (III)-containing solution was prepared following the method of Kekesi [160]. In this method, 10 mM of previously prepared MoCl_5 in 6 M HCl solution was transferred from the glass flask into the apparatus by argon gas pressure as shown in Figure 3.3.

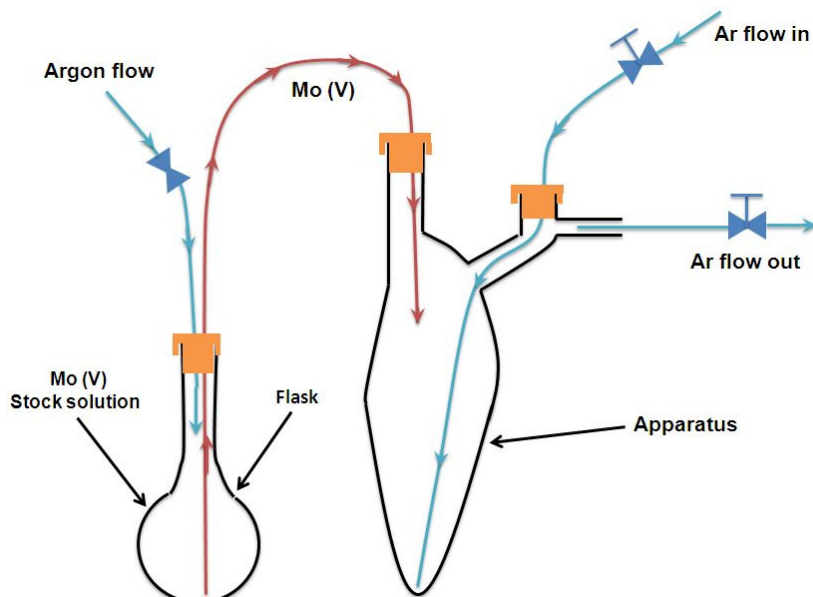


Figure 3.3 MoCl_5 solution transfer from flask into the flash with two neck narrow bottom.

After transferring the Mo (V) solution, 1.2 g of granulated zinc (Fischer Scientific, purity $\geq 99\%$) was added to 10 ml of the solution whilst being purged with argon as shown in Figure 3.4a. Adding the zinc powder produced vigorous evolution of hydrogen gas as shown in Figure 3.4b. After Mo (V) reduction to Mo (III) by zinc powder, the Mo (III) solution was transferred via plastic tube and under argon gas atmosphere to the plastic cuvette as shown in Figure 3.5.

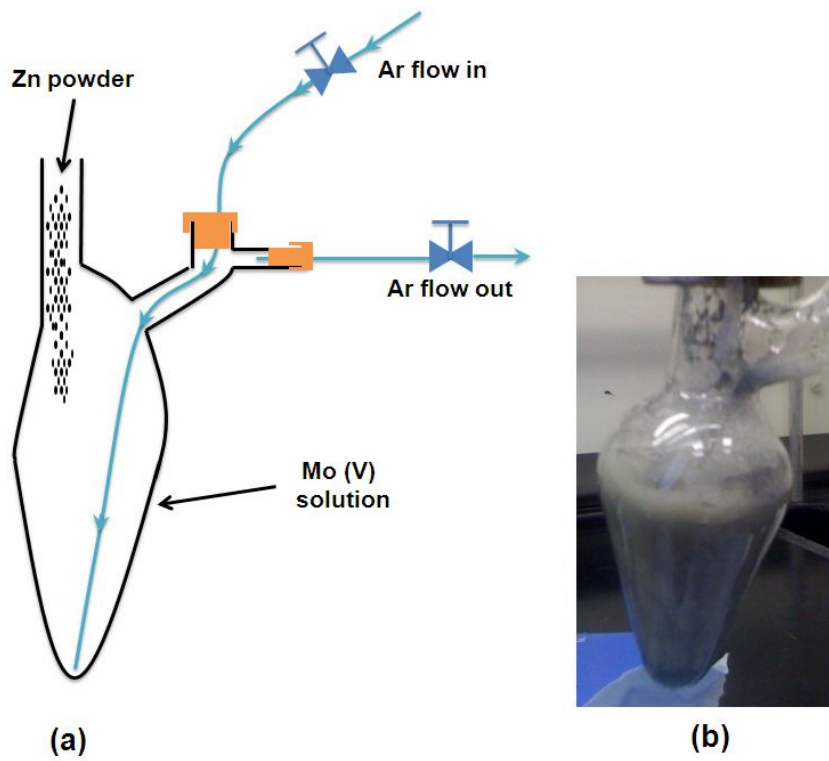


Figure 3.4 (a) Addition of zinc powder to Mo (V) solution (b) zinc reaction with Mo (V) solution.

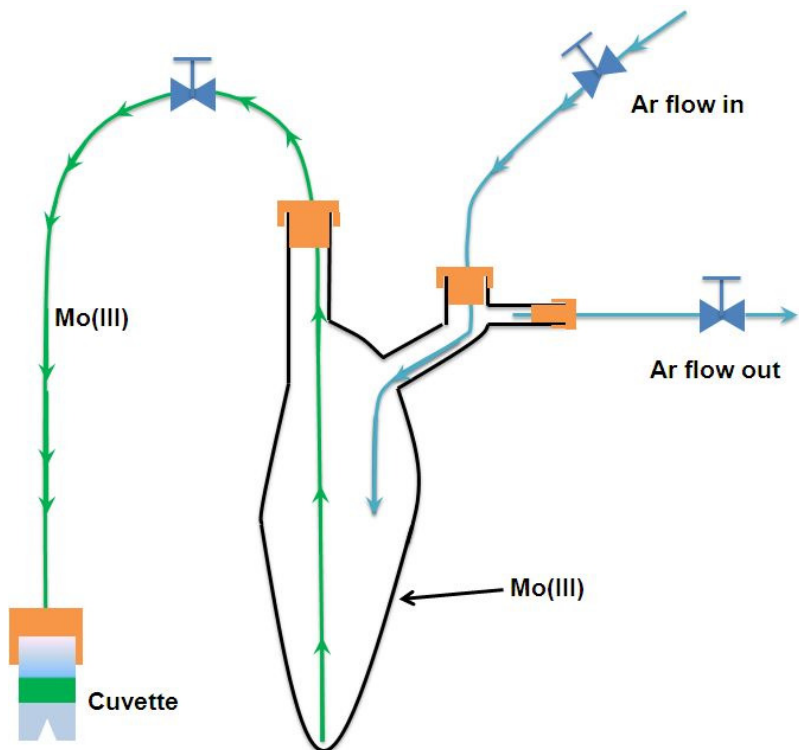


Figure 3.5 Mo (III) solution transfer from apparatus into a plastic cuvette under argon gas atmosphere.

3.2.6. Reference materials for XANES measurements

Details of reference materials including the primary powder, oxidation state, solution composition and environment are shown in Table 3.2 for Fe, Cr and Ni as well as Table 3.3 and Table 3.4 for Mo and Ti standards respectively.

Table 3.2 List of Fe, Cr and Ni reference materials for XANES measurements

Compound	State	Oxidation state	Solution composition	Environment	Species
FeSO ₄ .7H ₂ O	Solution	2	10 mM in water	Air	Fe(H ₂ O) ₆ ²⁺
Fe ₂ (SO ₄) ₃	Solution	3	10 mM in water	Air	Fe(H ₂ O) ₆ ³⁺
FeCl ₂ .4H ₂ O*	Solution	2	10 mM in LiCl/HCl/water [12M Cl ⁻]	N ₂	Fe ²⁺
FeCl ₂ .4H ₂ O*	Solution	2	10 mM in 10 M HCl	N ₂	Fe ²⁺ [124]
FeCl ₂ .4H ₂ O*	Powder	2	-	N ₂	Fe ²⁺
Cr(NO ₃) ₃ .9H ₂ O	Solution	3	10 mM in Water	Air	Cr(H ₂ O) ₆ ³⁺
CrCl ₃ .6H ₂ O	Solution	3	10 mM in 10.44 M HCl	Air	CrCl ₃ (H ₂ O) ₃
Ni(NO ₃) ₂ .6H ₂ O	Solution	2	10 mM in Water	Air	Ni(H ₂ O) ₆ ²⁺

*air sensitive

Table 3.3 List of Mo reference materials for XANES measurements

Compound	State	Oxidation state	Solution composition	Environment
*Mo acetate	powder	2	-	N ₂
*K ₃ MoCl ₆	powder	3	-	N ₂
*K ₃ MoCl ₆	solution	3	0.1M in 1, 6 and 10 M HCl	N ₂
*MoCl ₃	powder	3	-	N ₂
*Mo(III) [160]	solution	3	10 mM in 6 M HCl	N ₂
*MoO ₂	powder	4	-	N ₂
*MoCl ₅	powder	5	-	N ₂
*MoCl ₅	solution	5	0.1 M in 1 and 6 M HCl	N ₂
Na ₂ MoO ₄	powder	6	-	Air
Na ₂ MoO ₄	solution	6	0.1 M in 1 and 6 M HCl	Air

*air sensitive

Table 3.4 List of Ti reference materials for XANES measurements

Compound	State	Oxidation state	Solution composition	Environment
Anatase (TiO ₂)	powder	4	-	air
Rutile (TiO ₂)	powder	4	-	air
TiCl ₄	solution	4	9 mM TiCl ₄ in 0.55 M HCl	N ₂
BSA	solution	4	9 mM TiCl ₄ in 0.55 M HCl	air
Ringers solution	solution	4	9 mM TiCl ₄ in 0.55 M HCl	air

3.2.7. Ringer's solution and BSA

Ringer's solution recipe was made in 1000 ml distilled water as shown in Table 3.5.

Table 3.5 Chemical constitution of Ringer's solution

NaCl(g)	NaHCO ₃ (g)	CaCl ₂ .6H ₂ O(g)	KCl(g)	Distilled water(ml)
6.5	0.2	0.25	0.42	1000

BSA solution was made by dissolving 10 ml of BSA (Sigma Aldrich) in 1000 ml of PBS (phosphate buffer solution). PBS solution was also made by combining 7.75g (NaCl), 0.2g (KH₂PO₄) and 1.5g (K₂HPO₄) in 1000 ml distilled water.

3.3. Electrochemical cells and procedures for synchrotron studies of artificial pits

3.3.1. Electrochemical cells and samples

Working electrodes were made from 3 mm wide strips of 50 µm foils of 316L stainless steel or commercially pure titanium sandwiched between Kapton adhesive tape with epoxy adhesive (Araldite) and attached to a (PVC) plastic reservoir. The electrochemical cell contained ~ 20 mL of 1 M HCl or 1 M LiCl, an Ag/AgCl reference electrode and a platinum wire counter electrode. (All potentials are reported relative to Ag/AgCl). The schematic diagram of the sample and electrochemical cell is shown in Figure 3.6.

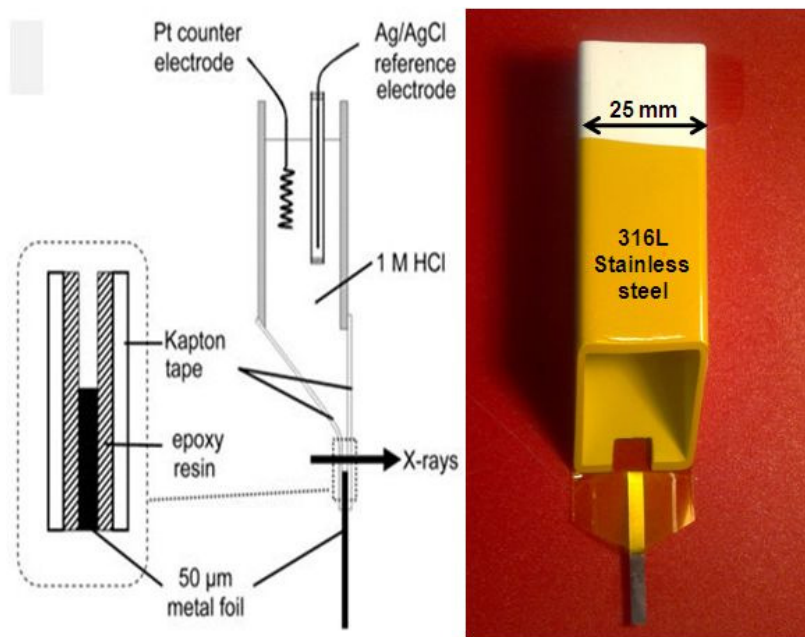


Figure 3.6 Schematic diagram of the sample and electrochemical cell used for XANES measurements.

3.3.2. Electrochemical procedures for growing artificial pits

Pits were grown to a depth of ~ 3 mm prior to making X-ray measurements. For 316L stainless steel, the potential of the working electrode was set at 0.9 V (Ag/AgCl) via an ACM potentiostat so that the 316L stainless steel would corrode across the entire section of the sample uniformly to a depth of ~ 3 mm. Kimura et al. [161] applied 0.8 V (Ag/AgCl) to grow the entire section of the 316 Stainless steel. Figure 3.7 shows a radiography image of the 316L stainless steel pit with a salt film above the interface.

Potentiodynamic measurements were carried out on titanium artificial pit to find out the lowest potential which the sample corrodes. The cyclic procedure was set up from 0 V (Ag/AgCl) to 12 V (Ag/AgCl). Therefore, for titanium, an applied potential of 10 V (Ag/AgCl) was required to corrode the entire cross-section of the sample to a depth approximately 3 to 4 mm. The potential was then decreased to 7V and the pit was grown

under potentiostatic conditions. The metal/solution interface was non-uniform showing considerable roughness with dark and bright regions inside the pit. XANES spectra were collected at a number of different regions inside the pit and above the pit mouth.

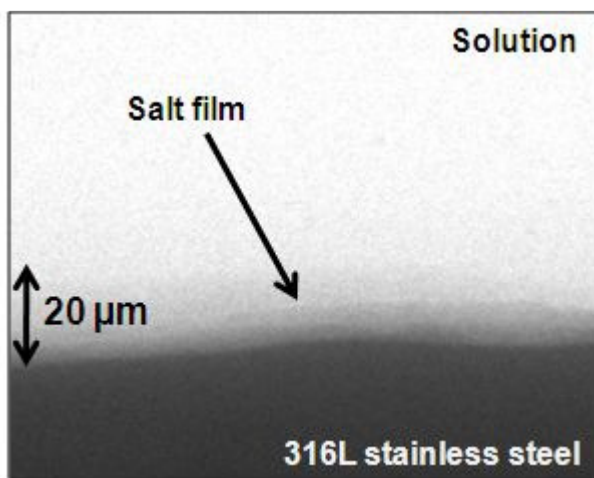


Figure 3.7 Radiography image of 316L stainless steel pit grown at 0.9 V (Ag/AgCl) in 1 M HCl (Image was taken at TOMCAT beamline, Swiss Light Source).

3.4. Preparation of human tissue and cell culture samples

Sections of human tissue and all cultures 4-6 μm thickness were mounted on ultra-pure fused silica plates (< 10 ppb Ti) (Spectrosil 2000, Heraeus Quarzglas GmbH & Co., Hanau, Germany), covered with 25 μm kapton film and sealed peripherally with epoxy. Supplementary tissue samples which had not been exposed to Ti were prepared in an identical manner as a control. Measurements on a Ti-free tissue control confirmed the absence of contamination during sample preparation. XANES spectra were acquired at regions where Ti was detected in the XRF map to determine its chemical state. XANES data was acquired to allow determination of the speciation of the Ti via a comparison with Ti species of known co-ordination.

3.5. Synchrotron experiments

3.5.1. XANES experiments at Diamond I18 beamline

Mo K-edge XANES measurements of artificial pit cells were all made in the fluorescence mode on the microfocus spectroscopy beamline (I18) at Diamond Light Source [162]. The beamline has a Si (111) monochromator to produce a X-ray beam working over a 2-20 keV energy range. The beam size was $3.5\text{ }\mu\text{m}$ high \times $6\text{ }\mu\text{m}$ wide. Different thickness ranges of attenuation filters between 0.5 and 2.05 mm of Al foil were used to carry out the measurements to give a flux of between 4×10^{10} and 1.5×10^{11} photon/s. Attenuation filters were used to prevent beam damage which could be observed as hydrogen evolution at the beam position at metal/solution interface. The cell was placed on a moving stage to collect the spectra at different positions by moving it up and down. For stainless steel, measurements were made close to and relative to the position of the dissolving interface. It takes 5–10 min to collect the XANES data for each measurement but the interface is moving due to a continuous dissolution at a velocity of $\sim 1\text{-}2\text{ }\mu\text{m/min}$. If the cell stays at the fixed position, the real position will not be fixed in the course of scan. Therefore the beam position should be maintained at a constant position during the data collection. The position of the interface was determined by measurement of the intensity of x-rays transmitted through the cell and the interface was defined as that point at which the transmitted intensity was halfway between the intensity measured through the cell in a region of bulk electrolyte and intensity measured through the electrode. The velocity of the interface was determined by a least squares fit to the position of the electrode surface measured at 2 min intervals over a 10 min period. The sample was moved to a position relative to the electrode interface and a XANES scan was initiated. Following every energy step in the scan, the movement of the electrode caused by

dissolution was estimated: if the predicted movement was greater than $0.05\text{ }\mu\text{m}$ the position was changed to compensate for the predicted movement of the electrode surface. The registration of the beam with respect to the interface during a scan was also monitored, qualitatively, using the microscope sample viewing system on the beamline. The electrode interface position was remeasured after each scan. The velocity was measured periodically and after any change in experimental conditions. The schematic diagram for the location of XANES measurements for 316L stainless steel artificial pit is shown in Figure 3.8.

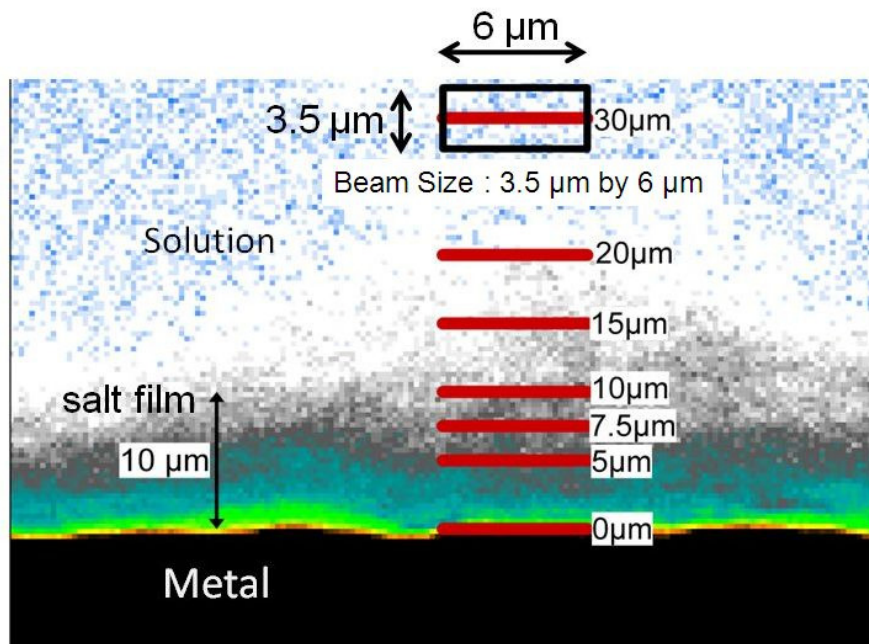


Figure 3.8 Schematic of XANES data collection positions relative to the interface (This image is the radiography image taken at TOMCAT beamline, Swiss Light Source)

As we are not interested in the salt film region for titanium, the XANES measurements were performed above the dissolving interface inside the pit solution at different positions in dark and bright spots in the pit solution.

3.5.2. XRF mapping at Diamond I18 beamline

Ti fluorescence was mapped using the micro-focus capability of I18 beamline (Diamond Light Source) (5 μm spot size) using an incident energy of 5.7 keV to identify the relative concentration and distribution of different Ti species within the respective tissue samples. Fluorescence data were collected using a 9-element Ge monolithic solid state detector (Ortec) with XSPRESS2 processing electronics [163]. The incident beam was focused to give a spot size 5 μm (H) by 3.4 μm (W) and the sample was mounted at a 45° angle to the incident beam, thus resulting in a resolution of 5 μm by 5 μm . The measurements were undertaken in reflection mode at room temperature. The fluorescence intensity under the K_α and K_β emission peaks were integrated to give the total number of counts.

3.5.3. XANES measurements at Diamond B16

XANES measurements on Mo standards were made at Diamond Light Source on the test Beamline B16, which is sited on a bending magnet and designed to carry out a wide variety of X-ray measurements [164]. These measurements used a water cooled fixed exit Si (111) double crystal monochromator and were made in transmission mode.

3.5.4. XANES measurements at Diamond B18

Some XANES measurements for Mo standards and 316L stainless steel artificial pits were made at B18 beamline. These measurements used Si (111) crystal monochromator [165] giving energy range 2.1 - 20.2 keV with a 9 element Ge detector (6 – 35 keV). The beam size was approximately 150 μm (H) x 200 μm (V) which gives higher flux and statistics in the case of solution standards.

3.6. XAS data analysis

3.6.1. XANES

XANES data analysis was carried out using Athena software (Version 0.8.061, 2001-2009, [166]). Figure 3.9a shows the raw data followed by background removal and normalisation as shown in Figure 3.9b for an Fe metallic foil. Normalisation should be carried out by selecting two points which have the best fit in pre-edge and post-edge regions. It is very important to be consistent in choosing the normalisation range for any single measurement.

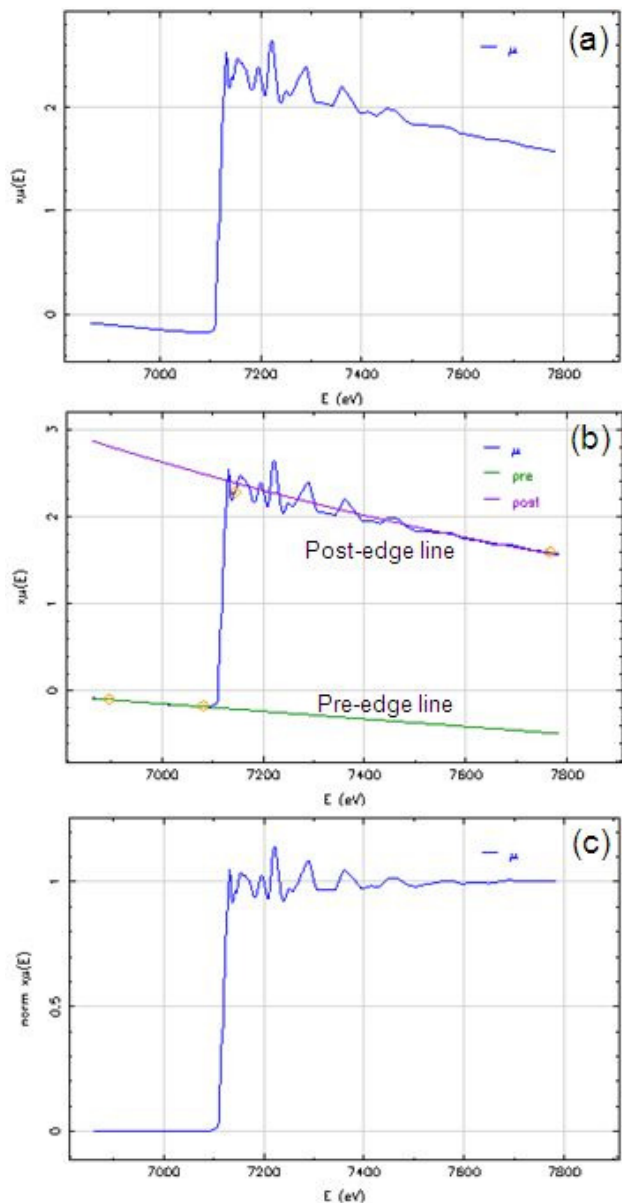


Figure 3.9 Normalisation procedure of XANES spectra using Athena software
(a) a typical plot of raw data (b) selection of the pre-edge and post-edge range for normalisation (c) a plot of normalised data

4. Chemistry of Fe, Ni and Cr in 316L stainless steel artificial pits

4.1. Introduction

XANES gives information about the oxidation state and speciation of different elements present in a system. In this chapter, XANES spectra were collected through the pit solution and salt film areas in artificial pits in 316L stainless steel in order to study the speciation and oxidation state of Fe, Cr and Ni. These results are very important for studying the chemistry of alloying elements during dissolution of 316L stainless steel in chloride environments through a salt film. During XANES measurements, the interface dissolves continuously at a velocity of $\sim 1\text{-}2 \mu\text{m/min}$. Therefore, it is necessary to maintain the dissolving electrode at a constant position relative to the X-ray beam, which was achieved with the procedure explained in Chapter 3.

4.2. Results

4.2.1. Electrochemistry of pit growth

Artificial pits in 316L stainless steel were grown in 1 M HCl under potentiostatic conditions as explained in Chapter 3. XANES measurements were carried out on different artificial pit samples for Fe, Cr and Ni K-edge spectra. Preparation of a sample for XANES typically required nine hours to grow the pit of sufficient depth ($\sim 3 \text{ mm}$). Figure 4.1 shows the time dependence of the current for a 316L stainless steel sample after applying 0.9 V (Ag/AgCl) for three consecutive periods of three hours for a typical artificial pit sample. Each stage has different vertical scales to show the current fluctuations. After 9 hours, the current reached a

current density of ca. 0.14 mA cm^{-2} (Figure 4.1c) at which point XANES measurements were carried out.

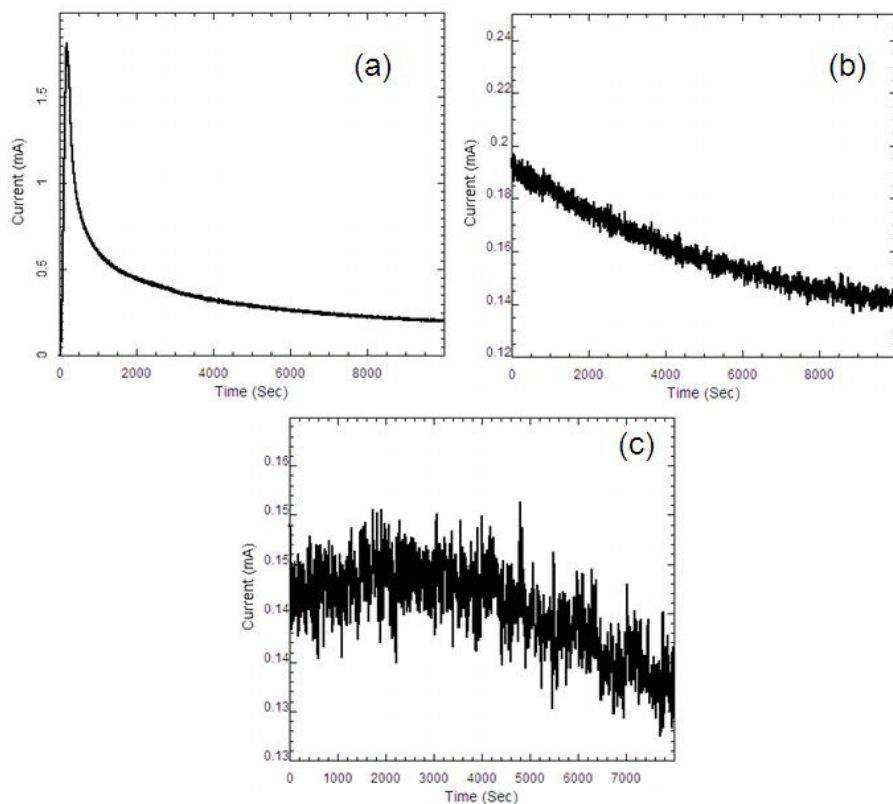


Figure 4.1 Electrochemical behaviour of a typical 316L stainless steel artificial pit grown at 0.9 V(Ag/AgCl) in 1 M HCl . (a) initially grown at 0.9 V for 3 hours; (b) the same sample continuing to grow at 0.9 V for 3 hours following stage a; (c) the same sample continuing to grow at 0.9 V for 3 hours following the stage (b).

The XANES measurements were carried out on pits of approximately 3 mm depth. The pits were growing under diffusion-limited conditions with a salt film at the dissolving interface and a saturated solution adjacent to the salt film. XANES spectra for Fe, Cr and Ni were measured and data are presented for each of these in turn. Figure 4.2 shows the schematic diagram of 316L stainless was grown at 0.9 V (Ag/AgCl) in 1 M HCl .

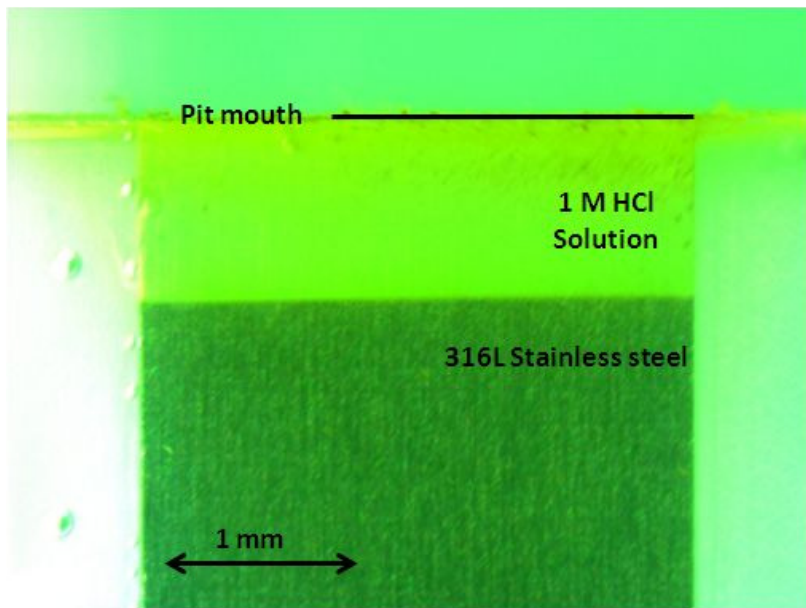


Figure 4.2 Optical image of a typical 316L stainless steel pit grown at 0.9 V (Ag/AgCl) in 1 M HCl used for XANES measurements.

4.2.2. Speciation of Fe in 316L stainless steel artificial pit

XANES spectra were collected from a series of reference samples, selected to encompass all of the species likely to be found in a 316L stainless steel pit. The iron foil K-edge spectrum was calibrated to the inflection point of iron of 7112 eV [167], and other spectra were calibrated accordingly to this standard.

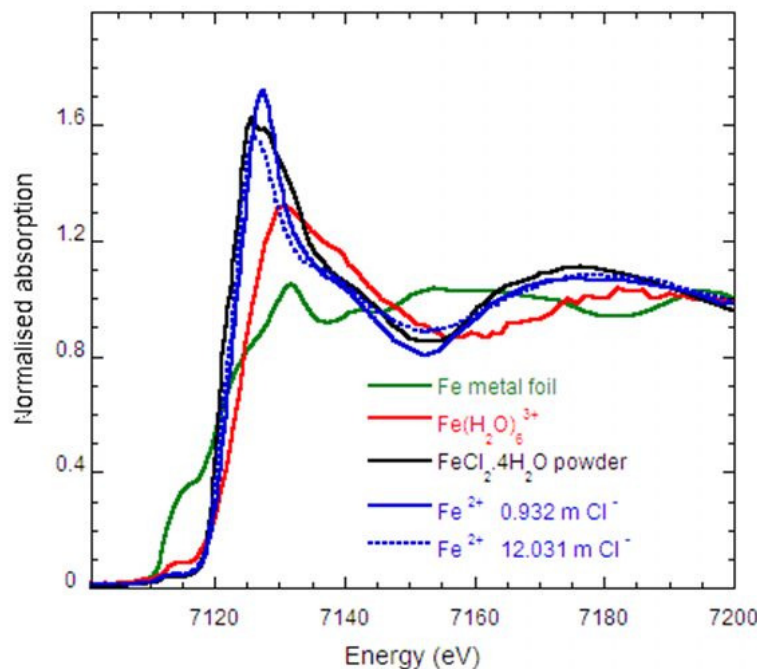


Figure 4.3 Normalised Fe K edge absorption spectra for reference materials: iron foil (green), $\text{Fe}(\text{H}_2\text{O})_6^{3+}$ (red) prepared according to Benfatto [125], $\text{FeCl}_2 \cdot 4\text{H}_2\text{O}$ powder (black) and Fe^{2+} standards (blue) data set provided by Barbara Etschmann [129]. All the spectra were measured in fluorescence except the metal foil, which was measured in transmission.

Figure 4.3 shows the Fe K-edge spectra of the reference materials that were used to compare with 316L stainless steel pit spectra. In all of the solid and solution standards, iron has an octahedral coordination. The data sets for Fe^{2+} were provided by Barbara Etschmann from the work published by Testemale et al. [129] for 0.932 m and 12.031 m chloride concentrations at 25 °C.

4.2.3. Fe spectroscopy in 316L stainless steel artificial pits

The XANES spectra measured at various positions above the interface of a 316L stainless steel pit ~ 3 mm deep grown at 0.9 V (Ag/AgCl) and in the presence of a salt film are shown in Figure 4.4. All the spectra measured more than 8 μm above the interface are similar but different from those at the interface and 4 μm above the interface.

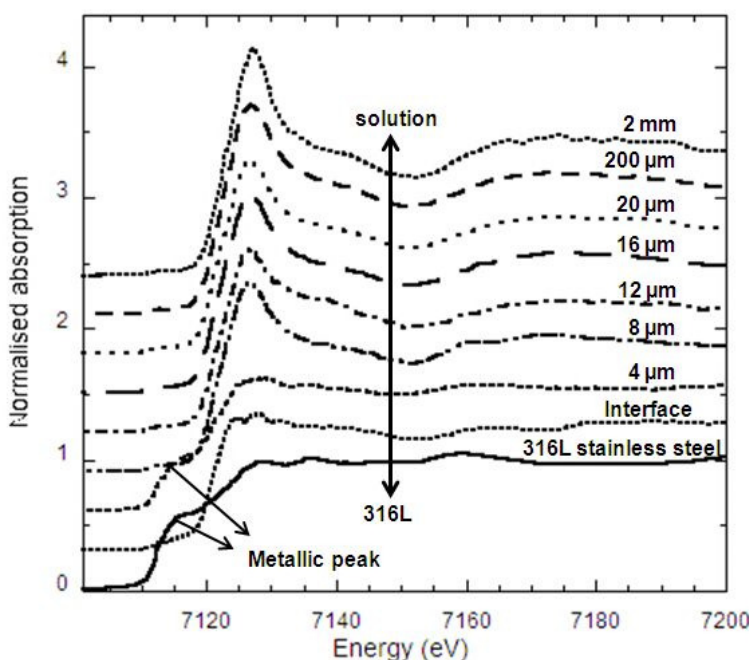


Figure 4.4 Fe K edge spectra (measured in fluorescence) for the solution inside a typical 316L stainless steel artificial pit grown at 0.9 V(Ag/AgCl) in 1 M HCl at different positions above the dissolving interface. The spectrum for the alloy (also measured in fluorescence) is shown for comparison.

The pre-edge region for the spectra measured at 4 μm and at the interface shows a shoulder that is characteristic of the metal. This is likely to be a result of some roughness at the interface and the fact that tail of the beam extends beyond the nominal 3.5 μm vertical height.

The oxidation state of iron in the pit can be determined by comparison with standards with different oxidation states. Figure 4.5 compares the XANES spectra measured at different positions within a pit with Fe^{2+} and Fe^{3+} solution standards. The position of the absorption edge for spectra measured within a pit fit very well with oxidation state +2 and there is a clear shift in edge energy with respect to the Fe^{3+} solution standard.

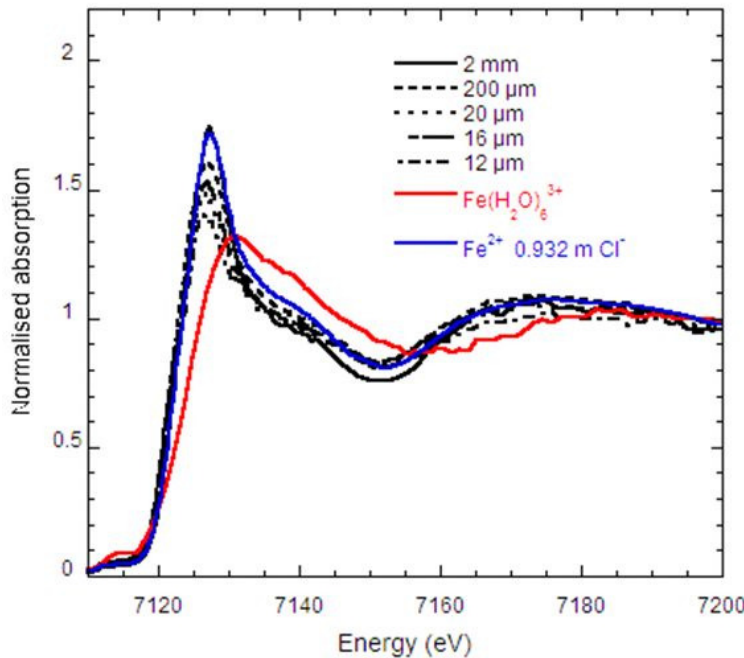


Figure 4.5 Normalised Fe K edge spectra (measured in fluorescence) for the solution inside a typical 316L stainless steel artificial pit grown at 0.9 V(Ag/AgCl) in 1 M HCl at different positions above the dissolving interface compared with Fe^{2+} (blue) and Fe^{3+} (red) solution standards.

Whilst the position of the absorption edge measured at all points within the pit is consistent with a +2 oxidation state for the iron species, there are systematic changes in the overall shape of the XANES spectra which indicate that the coordination of iron varies within the pit.

Figure 4.6 shows variation of the intensity of the white line (maximum peak height) as a function of position within the pit. It can be seen that the intensity of the white line is greatest for 2 mm, and is significantly lower for 200 µm, and then decreases further for 20 µm. However, the values for 16, 12 and 8 µm are scattered around that for 20 µm. The concentration of iron species is expected to vary from ca. 3.4 M at the salt film [12] to a significantly lower value at the pit mouth, hence that of the chloride ions also changes from ca. 11 M at the interface to close to 1M at the pit mouth (the bulk electrolyte is 1M HCl). Hence the most likely cause of the change in the white line intensity is the increased coordination of iron by chloride ions from the pit mouth to the salt film.

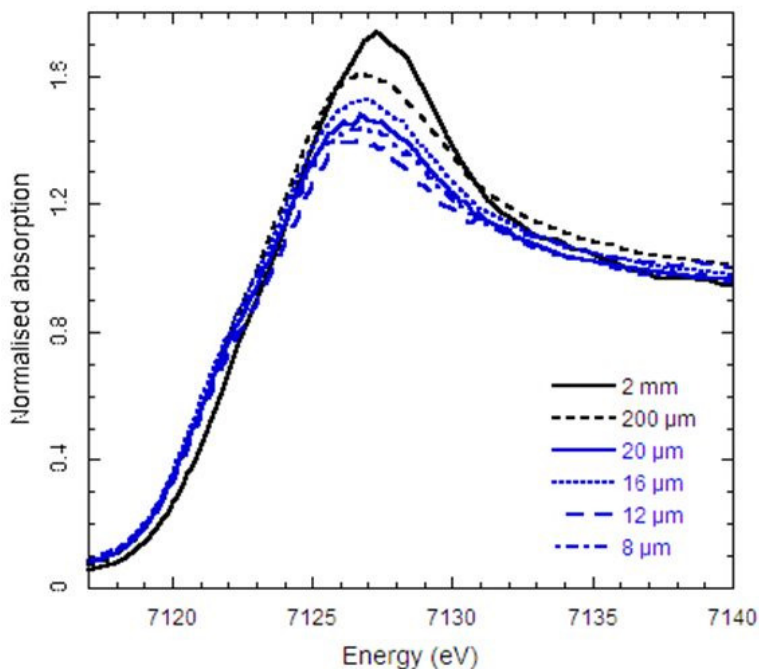


Figure 4.6 Normalised Fe K edge spectra (measured in fluorescence) for the solution inside a typical 316L stainless steel artificial pit grown at 0.9 V(Ag/AgCl) in 1 M HCl at different positions above the dissolving interface showing the white line intensity.

Supporting evidence for this is given in Figure 4.7 where spectra measured at the pit mouth and close to the salt film are compared with spectra of Fe^{2+} measured by Testemale et al. [129] in ~ 0.9 m and ~ 12 m chloride solutions. It can be seen that the spectrum for Fe^{2+} in 0.9 m Cl^- and that measured near the pit mouth at 2mm are very similar, and likewise, spectra measured at 16 μm in the pit and in ~ 12 m Cl^- are similar. However, both pairs are very different to the XANES spectrum of solid $\text{FeCl}_2 \cdot 4\text{H}_2\text{O}$. The second plot (b) in Figure 4.7 is included to show that all spectra were normalised at 7200 eV.

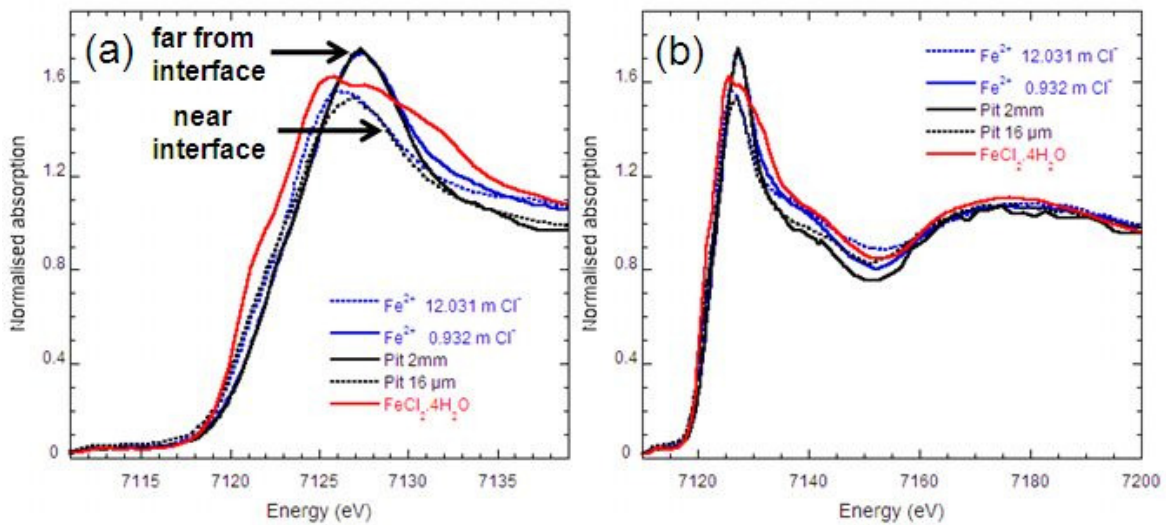


Figure 4.7 Normalised Fe K edge spectra (measured in fluorescence) of the solution inside a typical 316L stainless steel artificial pit grown at 0.9 V(Ag/AgCl) in 1 M HCl at 16 μm above the dissolving metal surface, and 2 mm (near the pit mouth); $\text{FeCl}_2 \cdot 4\text{H}_2\text{O}$ powder (red); Fe^{2+} solution standards with different chloride concentrations from Testemale et al. [129] (a) edge region (b) wider range

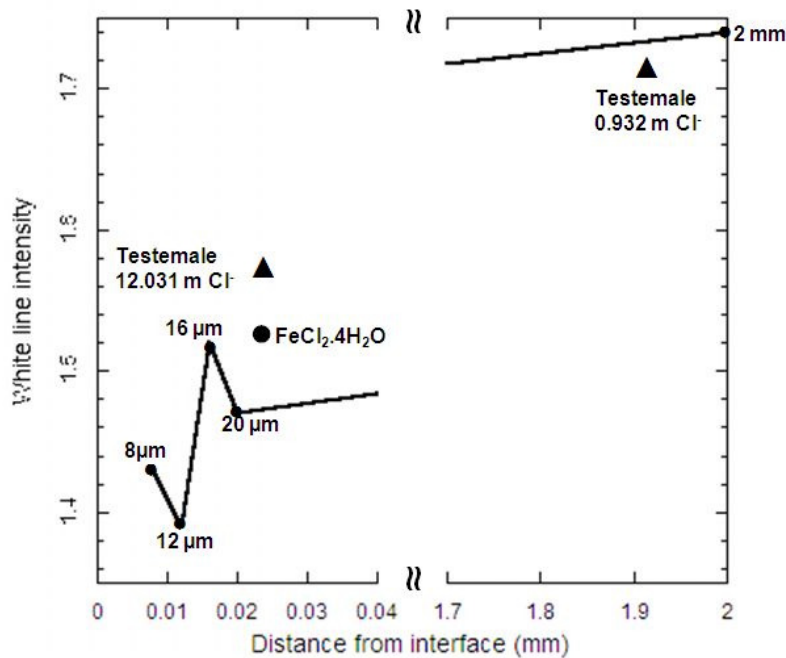


Figure 4.8 White line intensity (from Figure 4.6 and Figure 4.7) vs. distance from the interface for spectra inside a typical 316L stainless steel artificial pit grown at 0.9 V(Ag/AgCl) in 1 M HCl compared with Fe^{2+} solutions with 12.031 m and 0.932 m chloride concentrations from Testemale et al. [129] and $\text{FeCl}_2 \cdot 4\text{H}_2\text{O}$ powder standard.

Figure 4.8 shows a plot of the white line intensity for pit spectra as a function of distance from the dissolving interface, in comparison with the data from Testemale et al. [129] shown for reference. Again it is confirmed that a lower white line intensity is found near the

dissolving interface where the chloride concentration is likely to be ~11 M, consistent with data of Testemale et al. [129] at a chloride concentration of ~12 m, and a higher white line intensity is seen near the mouth of the pit where the chloride concentration is likely to be ~1 M, consistent with data of Testemale et al. [129] at a chloride concentration of ~0.9 m.

Testemale et al. [129] attributed the change in white line intensity to the formation of iron chloro-complexes in solutions of high chloride concentration. They also observed that the intensity of the pre-edge shoulder at ~7114 eV increased when the chloride concentration increased to ~12 m. Figure 4.9 shows that a similar trend is observed for the pit solutions: a higher pre-edge shoulder can be seen for the spectrum measured at 16 μm from the dissolving interface compared with the spectrum from the mouth of the pit (2 mm from the dissolving interface). The data from Testemale et al. [129] are included for reference.

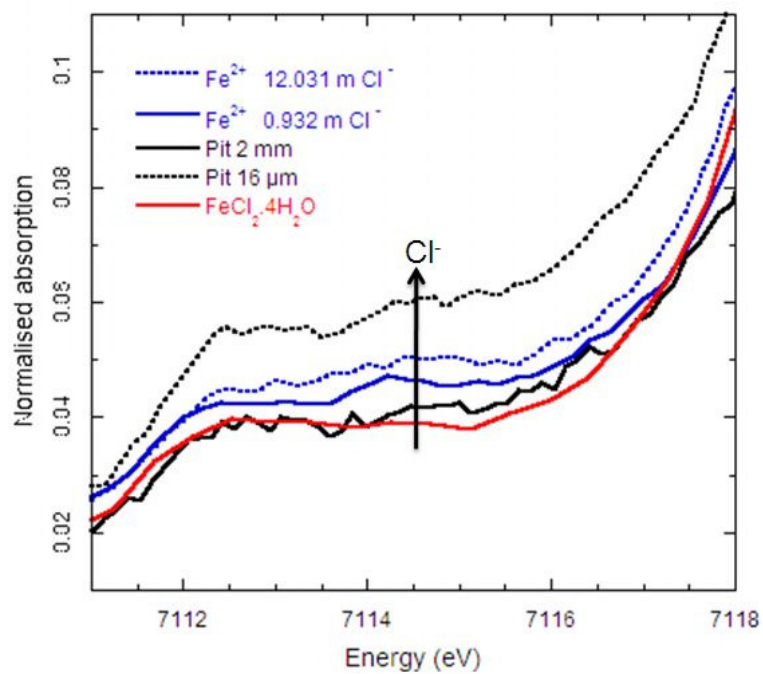


Figure 4.9 Pre-edge peaks for spectra inside a typical 316L stainless steel artificial pit grown at 0.9 V(Ag/AgCl) in 1 M HCl compared with Fe^{2+} with 12.031 m and 0.932 m chloride concentrations from Testemale et. al. [129] and $\text{FeCl}_2 \cdot 4\text{H}_2\text{O}$ powder standard.

The intensity of the pre-edge shoulder measured at 7114 eV is summarised in Figure 4.10. This shows that, spectra measured near to the interface have a lower pre-edge shoulder height. The changes are not large between 20 µm and 8 µm showing that in this region the speciation does not change dramatically and also that there is some fluctuation in the pre-edge intensity perhaps caused by errors in positioning the beam above the sample.

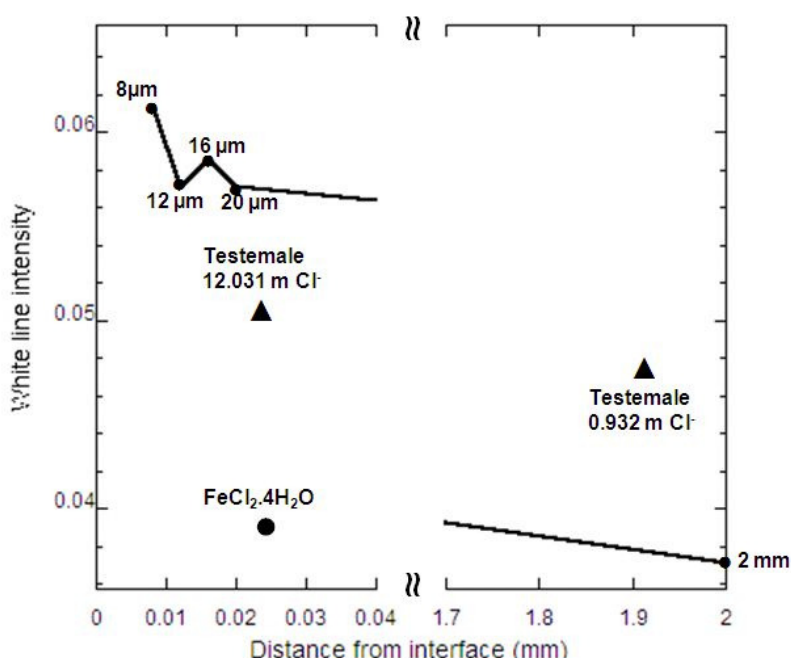


Figure 4.10 Pre-edge intensity vs. distance from the interface for spectra inside a typical 316L stainless steel artificial pit grown at 0.9 V(Ag/AgCl) in 1 M HCl compared with Fe^{2+} solutions with 12.031 m and 0.932 m chloride concentrations [129] and $\text{FeCl}_2 \cdot 4\text{H}_2\text{O}$ powder standard.

4.2.4. Speciation of Cr in artificial pit of 316L stainless steel

Chromium has oxidation states +2, +3 and +6 in aqueous environments and the chromium oxidation state in 316L stainless steel pit has been studied by a number of researchers [12, 16, 20, 27, 168] who reported a +3 oxidation state. However, pitting has not been studied using XANES. Therefore, both chromium reference materials were chosen with the same +3 oxidation state to investigate the chromium speciation in the 316L stainless steel pit. Two most well defined chromium species that may form in 316L stainless steel pits are $\text{Cr}(\text{H}_2\text{O})_6^{3+}$

and $\text{CrCl}_3(\text{H}_2\text{O})_3$. They were prepared to compare with XANES spectra obtained from 316L stainless steel pit solution as a function of distance from the metal-solution interface. Figure 4.11 shows the XANES spectra of the chromium hexa-aquo ion ($\text{Cr}(\text{H}_2\text{O})_6^{3+}$), chromium chloro-complex ($\text{CrCl}_3(\text{H}_2\text{O})_3$) and chromium metallic foil. The Cr foil K-edge spectrum was calibrated to the first inflection point of the chromium metal spectrum at 5989 eV [167].

It may be seen in Figure 4.11 that there is a significant difference between the spectra of the hexa-aquo and chloro-complex ions: the hexa-aqo ion shows a sharp peak at the top of the edge with a shoulder at higher energy whereas the chloro-complex ion shows a broad peak. However, they both have the same small pre edge peak at the same position.

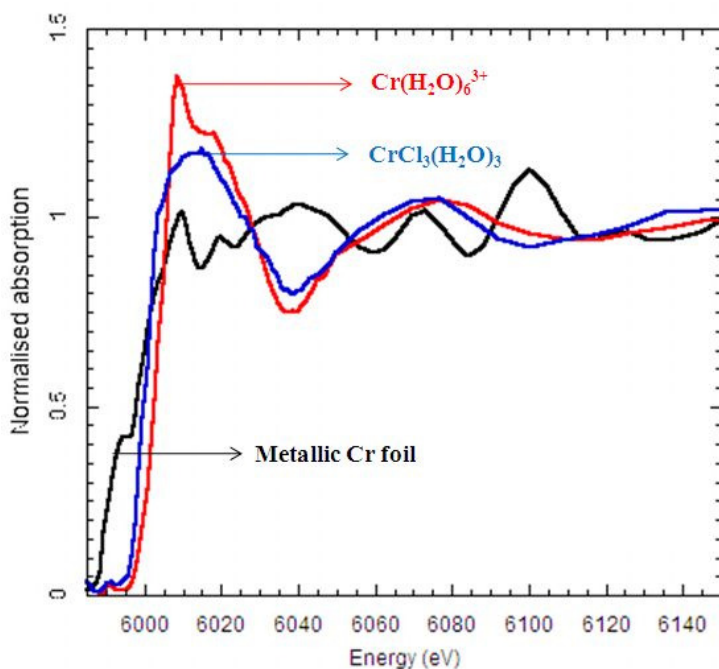


Figure 4.11 Normalised Cr K edge XANES spectra (measured in fluorescence) for $\text{Cr}(\text{H}_2\text{O})_6^{3+}$ (red) and $\text{CrCl}_3(\text{H}_2\text{O})_3$ (blue) solution standards [135] and Cr metal foil (measured in transmission).

4.2.5. Cr spectroscopy in 316L stainless steel artificial pits

The XANES measurements were carried out in a 316L stainless steel pit grown at 0.9 V (Ag/AgCl) to \sim 3 mm pit depth and in the presence of a salt film at the interface. Figure 4.12 shows a series of Cr k-edge XANES spectra measured as a function of position from the interface. The spectra at 4 μ m and 6 μ m are noisy compared with the spectra measured at greater distances from the electrode surface, and display a pre-edge feature which is not the same as the pre-edge peak of standard solution or spectra measured far from the surface. The cause of this is likely to be a contribution from a metallic pre-edge shoulder caused by surface roughness and a contribution from the tail of the beam beyond its nominal 3.5 μ m height.

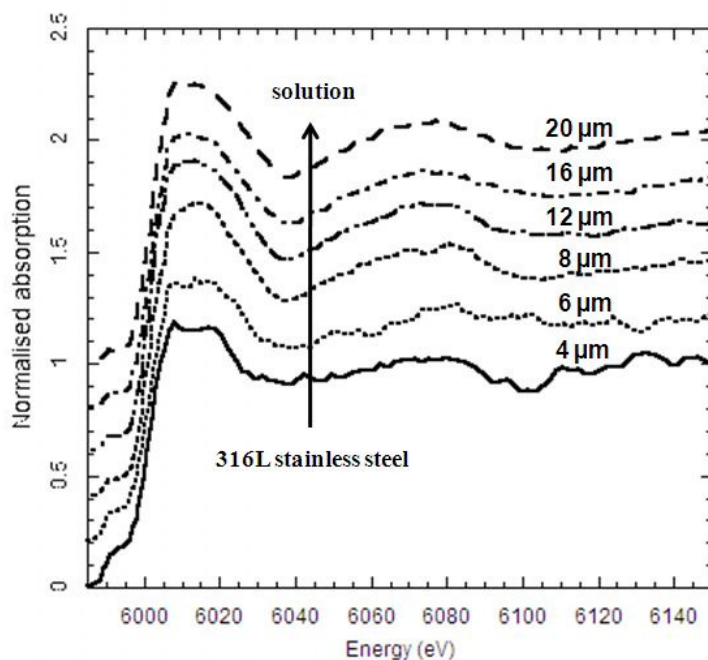


Figure 4.12 Normalised Cr K edge XANES spectra (measured in fluorescence) for the solution inside a typical 316L stainless steel artificial pit grown at 0.9 V(Ag/AgCl) in 1 M HCl at different positions above the dissolving interface.

Figure 4.13 compares the XANES spectra of the pit solution measured close to the interface with the spectra collected closer to the pit mouth from 100 μ m up to 2.8mm from the interface. The spectra for $\text{Cr}(\text{H}_2\text{O})_6^{3+}$ and $\text{CrCl}_3(\text{H}_2\text{O})_3$ are also shown for comparison. It can

be seen that the energy of the absorption edge is the same in all spectra and identical to that for the two Cr^{3+} reference solutions. However, there are marked changes in the shape of the white line dependent upon distance from the electrode. These can be readily interpreted by comparison with the two standards as shown in Figure 4.13. The Cr^{3+} hexa-aquo ion shows two features close to the absorption edge: a peak followed by a shoulder ~ 7 eV above the edge (A), whilst the chloro-aquo complex simply has a broad white line (B). Examination of spectra measured close to the mouth of the pit shows that they have a peak and shoulder. Hence, the spectra close to the pit mouth are most probably $\text{Cr}(\text{H}_2\text{O})_6^{3+}$. For spectra measured at $\sim 20 \mu\text{m}$ from the surface, the evidence for a peak and shoulder is much less clear and the spectra more closely resemble that of the chloro-complex standard. It is therefore likely that these are chloro-aqua complexes close to the electrode.

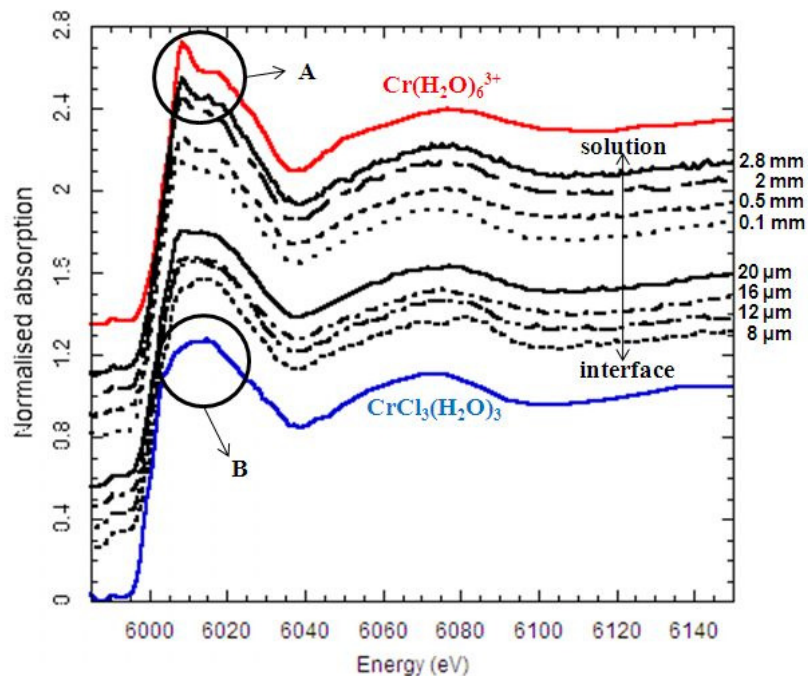


Figure 4.13 Normalised Cr K edge spectra (measured in fluorescence) for the solution inside a 316L stainless steel artificial pit grown at 0.9 V(Ag/AgCl) in 1 M HCl at different positions above the dissolving interface. The spectra of $\text{Cr}(\text{H}_2\text{O})_6^{3+}$ (red) and $\text{CrCl}_3(\text{H}_2\text{O})_3$ (blue) are shown for comparison.

4.2.6. Speciation of Ni in artificial pit of 316L stainless steel

The nickel oxidation state in 316L stainless steel pits in chloride environments has been studied by many researchers [12, 16, 20, 27, 168] and reported to be +2, so the solution species $\text{Ni}(\text{H}_2\text{O})_6^{2+}$ was selected as a reference solution. Figure 4.14 shows the XANES spectra of a 10 mM $\text{Ni}(\text{H}_2\text{O})_6^{2+}$ solution standard and a Ni foil. All the spectra were calibrated to the inflection point of nickel metal at 8333 eV [167].

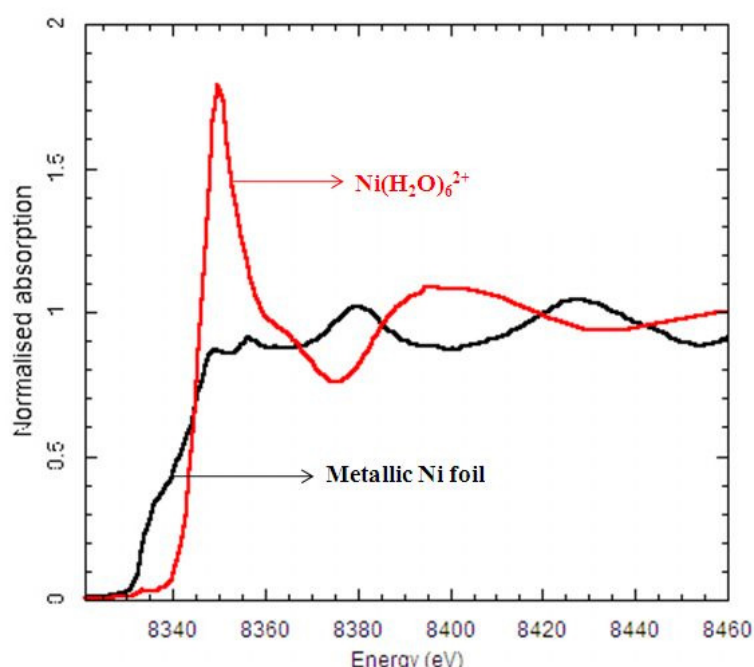


Figure 4.14 Normalised Ni K edge XANES spectra of $\text{Ni}(\text{H}_2\text{O})_6^{2+}$ (red) solution standard (measured in fluorescence) and Ni metal foil (measured in transmission).

Figure 4.15 shows a stack plot of XANES spectra measured at distances between 8-100 μm from the interface. All the spectra are similar, showing a very small pre-edge peak and featureless edge area. The spectrum at 8 μm position is noisy compared with spectra measured at other positions. As explained before in relation to Fe and Cr XANES spectra, the primary reason could be the spatial and temporal roughness at the interface.

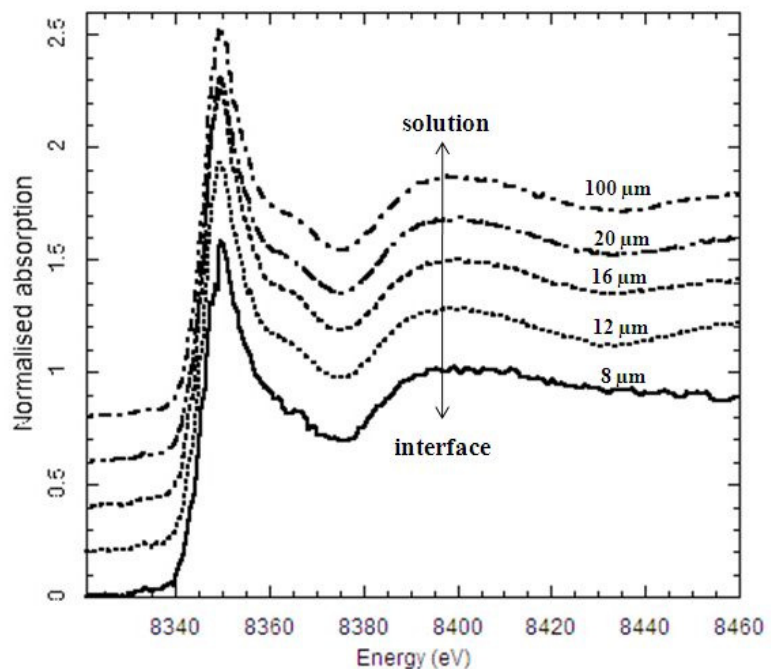


Figure 4.15 Normalised Ni K edge XANES spectra (measured in fluorescence) for the solution inside a typical 316L stainless steel artificial pit grown at 0.9 V(Ag/AgCl) in 1 M HCl at different positions above the dissolving interface.

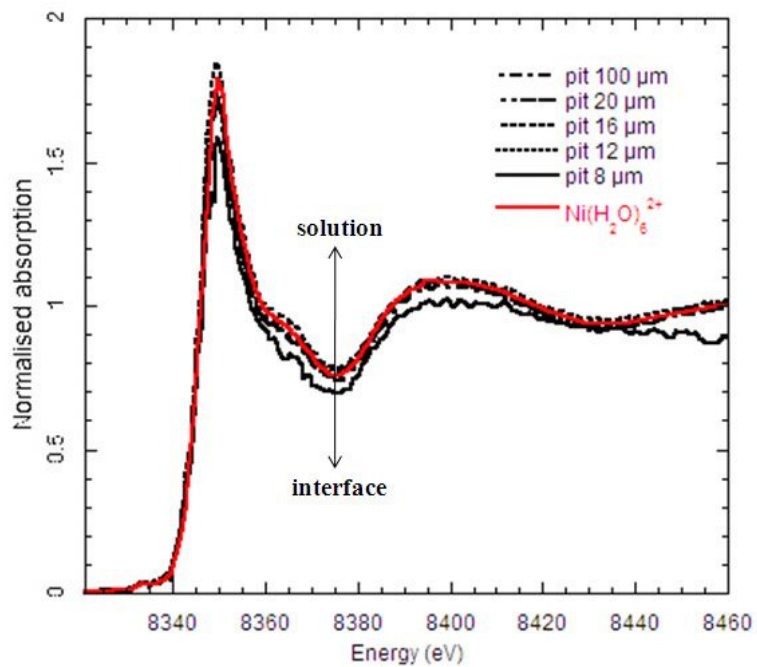


Figure 4.16 Normalised Ni K edge XANES spectra (measured in fluorescence) for the solution inside a typical 316L stainless steel artificial pit grown at 0.9 V(Ag/AgCl) in 1 M HCl at different positions above the dissolving interface. The spectrum of $\text{Ni}(\text{H}_2\text{O})_6^{2+}$ (red) is shown for comparison.

Figure 4.16, also shows the same spectra at different positions superimposed and compared with nickel hexa-aquo ion solution standard. All the spectra are normalised at 8460 eV. It can

be seen that the spectra at all positions comply very well with that of $\text{Ni}(\text{H}_2\text{O})_6^{2+}$ at both pre-edge and white line regions except the spectrum at 8 μm which is due to small fluctuations and heterogeneity of the dissolution process on a micron length scale at the solid/solution interface. Apart from the spectrum measured at 8 μm , there is no systematic change in white line or pre-edge intensity which shows consistent values for all positions through the pit.

4.3. Discussion

4.3.1. Fe spectroscopy in 316L stainless steel artificial pits

The pre-edge peak for spectra measured at 4 μm above the dissolving metal interface in a 316L stainless steel artificial pit is completely different from the spectra measured in the solution in that there is a metallic shoulder. The principal reason for this observation arises from the roughness of the interface and the fact that the tail of the beam extends beyond the nominal 3.5 μm vertical extent of the beam.

The solution spectra of the pit solution show that their overall shape is very similar to Fe^{2+} species obtained by Benfatto et al. [125] and Testemale et al. [129] who studied Fe^{2+} and Fe^{3+} solution species with the XANES method and found a distinct difference between these two species due to a sharp single peak for Fe^{2+} and a broader peak followed by a shoulder after the first peak for Fe^{3+} above the edge (See section 2.9.4.2) . There was also no shift in edge energy at different positions within the pit, which confirms that the oxidation state of iron inside the artificial pit of 316L stainless steel is indeed +2. This has been previously assumed in studies by Newman and Isaacs [20, 27] to study the dissolution and passivation kinetics of 316L stainless steel as well as in the simulation of Laycock et al. [43].

The solution spectra inside the pit solution showed a systematic trend in white line intensity which decreases from the mouth of the pit where there is ~ 1 M chloride concentration (background electrolyte is 1 M HCl) to the interface with ~ 11 M chloride [12]. This observation is supported by Testemale et al. [129], who observed similar results by measuring the XANES spectra at ~ 12 and ~ 0.9 m chloride concentrations, which are similar to the spectra collected from the interface and 2 mm above the pit, respectively. There was also an

increase in pre-edge intensity for the spectra close to the interface compared to the mouth of the pit. These observations can be attributed to the formation of chloro-complexes close to the interface owing to the increasing chloride concentration. However, it is unlikely that there is any structural change in the complexes from octahedral to tetrahedral, consistent with the results of Testemale et al. [129] and Liu et al. [129]. It should be noted that, solution spectra found for the pit solution are completely different with the spectra of solid $\text{FeCl}_2 \cdot 4(\text{H}_2\text{O})$ with octahedral structure coordinated with 4 oxygen and two chlorine atoms [169]. Apted et al. [124] studied Fe^{2+} ions in solutions with chloride concentrations ranging from 0.1 to 4 M and found octahedral hexa-aquo ions with no evidence of complexing. This suggests that chloride concentrations higher than 4 M are required for complexation.

In this work, chloro-complexes were found inside the pit solution close to the interface, but not near the pit mouth. Brossia et al. [40] did not find any evidence of Fe-Cl complexes in the solution of a simulated Type 308 stainless steel pit above the interface using Raman spectroscopy. It is possible that their work was not particularly sensitive to the region very close to the dissolving metal surface.

4.3.2. Cr spectroscopy in 316L stainless steel artificial pits

The Cr K-edge pit spectra at 4 and 6 μm above the dissolving interface are different from the other spectra, and display some fluctuations as well as a different pre-edge feature, which is likely to be a contribution from a metallic pre-edge peak caused by either surface roughness or x-ray fluorescence from the tail of the beam.

All the spectra in the pit and Cr^{3+} solution standards have the same edge energy position. There is also a similar small pre-edge feature in all spectra. This confirms that the oxidation

state of Cr throughout the pit is 3+, which is in agreement with the Raman measurements of Brossia et al. [40], the assumption of Newman and Isaacs [20, 27] and Laycock and White [43].

Figure 4.13 showed a clear difference between the spectra obtained from the mouth of the pit compared to that measured close to the interface. The spectrum at the pit mouth has a shape very similar to the $\text{Cr}(\text{H}_2\text{O})_6^{3+}$ standard spectrum, and the measurements of Diaz-Moreno et al. [135] for the hexa-aquo ion ($\text{Cr}(\text{H}_2\text{O})_6^{3+}$). The spectra measured at 8 μm are very similar to the standard $\text{CrCl}_3(\text{H}_2\text{O})_3$ solution and the measurements of Diaz-Moreno et al. [135]. The complexation is likely to be due to the high chloride concentration in the vicinity of the dissolving interface, $\sim 11 \text{ M}$ [12].

4.3.3. Ni spectroscopy in 316L stainless steel artificial pits

Ni K-edge spectra throughout the pit solution have the same edge shape and energy position. In addition the spectra fits very well with the $\text{Ni}(\text{H}_2\text{O})_6^{2+}$ reference solution (D'Angelo et al. [142]). This shows that the oxidation state of Ni is 2+ and its coordination is consistent throughout the 316L stainless steel artificial pit. This observation is in agreement with literature assumptions [12, 20, 27, 40, 43] that used the oxidation state 2+ for nickel in 316L stainless steel dissolution.

Solution spectra at all positions as a function of distance from the interface compares very well with the nickel hexaaquo ion ($\text{Ni}(\text{H}_2\text{O})_6^{2+}$), which is consistent with the observations of Brossia et al. [40] who found the same species using the Raman spectroscopy method.

4.4. Conclusions

1. The oxidation state of Fe inside 316L stainless steel artificial pits is +2 throughout the pit and the solution species changes from the hexa-aquo ion ($\text{Fe}(\text{H}_2\text{O})_6^{2+}$) near the mouth of the pit to chloro-complexes close to the dissolving interface adjacent to the salt film.
2. The oxidation state of Cr inside the artificial pit of 316L stainless steel is confirmed as +3 throughout the pit and the pit solution species are most probably $\text{Cr}(\text{H}_2\text{O})_6^{3+}$ near the mouth of the pit with chloro-complexes close to the dissolving interface.
3. Ni species inside a 316L stainless steel artificial pit are $\text{Ni}(\text{H}_2\text{O})_6^{2+}$ without any evidence of chloro-complexes.

5. Chemistry of Mo in 316L stainless steel artificial pits

5.1. Introduction

Molybdenum has a beneficial effect on the corrosion behaviour of 316L stainless steels. There are different mechanisms proposed as an explanation for this behaviour, including the effect of Mo on the chemistry of the passive film [48-54, 56, 170], formation of inhibiting molybdate species within pits [13], or the presence of Mo species on the metal surface within the pit blocking anodic dissolution [14, 26, 44, 45, 50, 51] in highly aggressive chloride environments. The aim of this chapter is to use X-ray absorption near edge structure (XANES) to study the chemistry of solutions in 316L stainless steel artificial pits to investigate the role of molybdenum in inhibition of pitting corrosion in chloride environments.

5.2. Results

Figure 5.1 shows a stack plot of Mo K-edge XANES spectra in the pit solution as a function of different positions from the metal/solution interface. It can be seen that the metal spectrum shows a clear shoulder below the edge energy with a corresponding peak as the first derivative at 20004 eV shown in Figure 5.1b. This peak may be seen for the spectra measured at the interface and 5 μm above the interface. The main reasons for this observation are the roughness of the interface and the tail of the beam which extends beyond the nominal 3.5 μm vertical height of the beam.

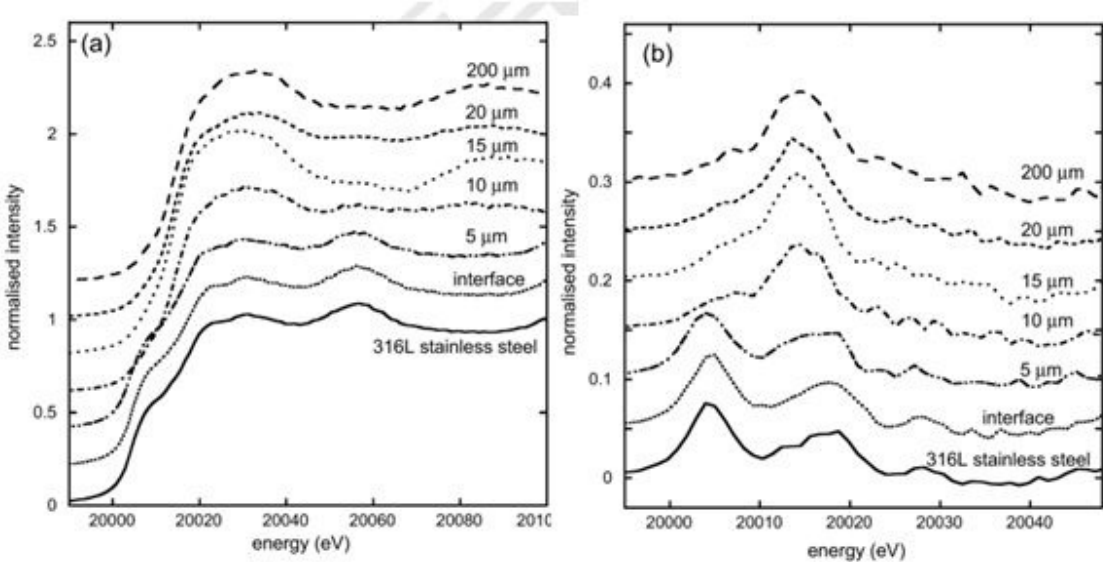


Figure 5.1 Mo K edge spectra (measured in fluorescence) for the solution inside a 316L stainless steel artificial pit grown at 0.9 V (Ag/AgCl) in 1 M HCl at different positions above the dissolving interface. The spectrum for the alloy (also measured in fluorescence) is shown for comparison. (a) Normalised spectra; (b) first derivative of the spectra shown in (a).

There is also a small metallic shoulder that can be seen in the spectrum 10 μm above the interface which is shown in the first derivative of the spectra in Figure 5.1b but the other spectra above 10 μm are similar in the pit solution without any edge features in the first derivative at 20004 eV. Least squares fitting of the above spectra at a range of different potentials showed that all the spectra showing a metallic shoulder can be fitted to a linear combination of 316L stainless steel metal and the solution spectra. Furthermore, there are no other species present in the spectra close to the interface. This observation is very important due to the presence of a salt film above the interface during the dissolution of metal [113, 171]. This is consistent with the findings of Isaacs and Huang [113], who used X-ray fluorescence to study 316L stainless steel artificial pits using a method very similar to the one used in these measurements. They reported that there is no accumulation of Mo in the salt film region close to the metal/solution interface.

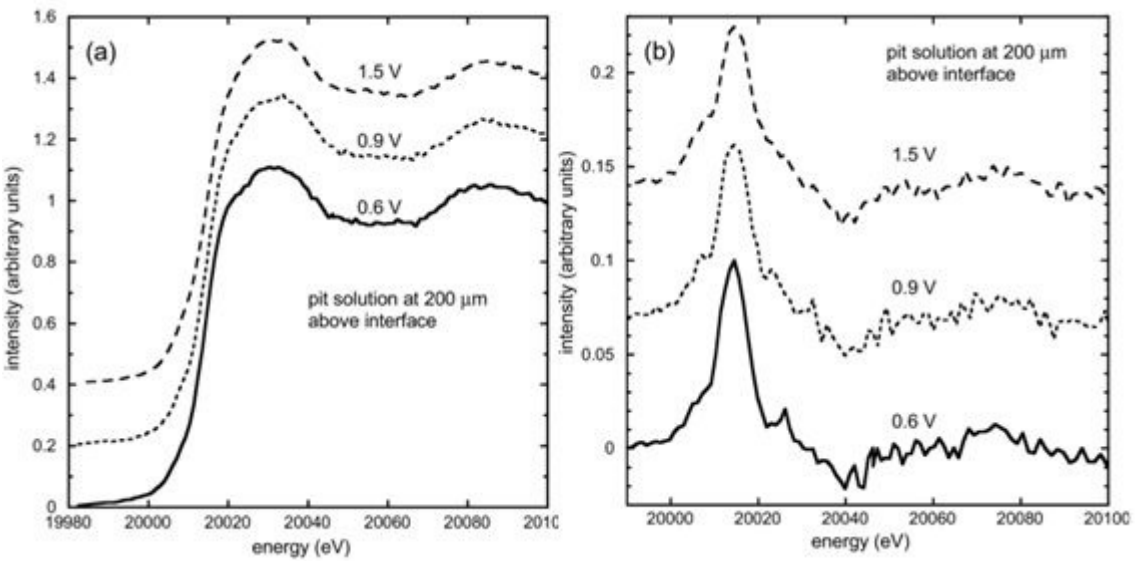


Figure 5.2 Mo K edge spectra (measured in fluorescence) for the solution at 200 μm above the dissolving interface inside a 316L stainless steel artificial pit grown in 1 M HCl at different potentials (vs. Ag/AgCl). (a) Normalised spectra; (b) first derivative of the spectra shown in (a).

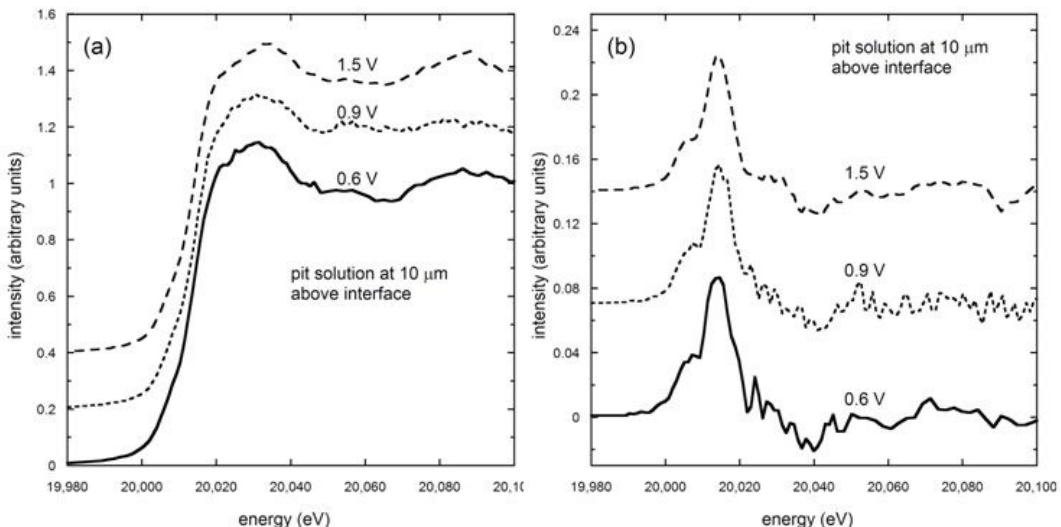


Figure 5.3 Mo K edge spectra (measured in fluorescence) for the solution at 10 μm above the dissolving interface inside a 316L stainless steel artificial pit grown in 1 M HCl at different potentials (vs. Ag/AgCl). (a) Normalised spectra; (b) first derivative of the spectra shown in (a).

Mo K-edge XANES spectra were also measured at different potentials at a position 200 μm above the interface as shown in Figure 5.2. All the spectra at different potentials have a very similar overall shape in the pre-edge and post edge region and there is no evidence of any systematic change in the species with changing potential. Similar observations were made at

other positions from the interface. Figure 5.3 shows a typical Mo K-edge XANES spectra were measured at a position 10 µm above the interface. Therefore, XANES measurements show that molybdenum speciation is not changing at different positions and different applied potentials from 0.6 to 1.5 V.

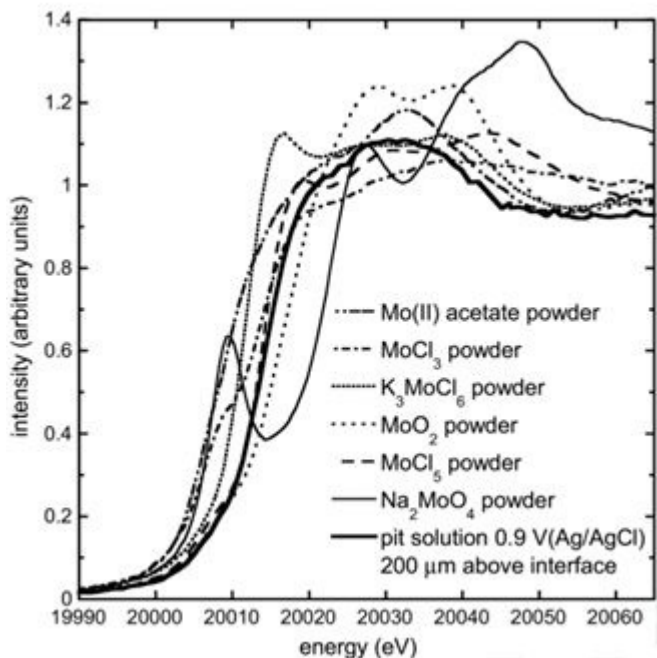


Figure 5.4 Normalised Mo K-edge spectra for the solution inside a 316L stainless steel artificial pit grown in 1 M HCl at 0.9 V(Ag/AgCl), 200 µm above the dissolving interface, and a number of molybdenum compounds in different oxidation states: molybdenum acetate(II), MoCl_3 (III), K_3MoCl_6 (III), MoO_2 (IV), MoCl_5 (V) and Na_2MoO_4 (VI) (see Table 3.3 for details).

Figure 5.4 shows the spectra of all molybdenum containing powder compound standards with different molybdenum oxidation states compared with a typical solution spectrum in an artificial pit at 200 µm above the dissolving interface. It can be seen that there is a general trend in the position of the absorption edge with increasing oxidation state. However, this small change in edge positions is very complicated since there is a pre-edge feature for some standards at ~20007 eV. Therefore, the oxidation state of molybdenum needs further investigation. The molybdenum (II) spectrum showed a similar shape to the spectrum in the pit solution, with no pre-edge. However, the edge position of the pit solution is ~ 5 eV above

the edge position of molybdenum (II). Therefore, the molybdenum oxidation state in the pit is not +2. The MoO_2 edge position is only 2 eV above the pit solution spectrum but has a completely different shape above the edge including two distinct peaks. Furthermore, it is known that MoO_2 is not soluble in solutions containing HCl [172], therefore the solution species is unlikely to be Mo(IV). Mo (III) and Mo (V) have closer edge positions to that of the pit solution so are possible candidates. Figure 5.4 shows that Mo (VI) has a very different spectrum compared with the solution spectrum, but since Kimura et al. [161] have claimed that molybdate species are present in 316L stainless steel pit solutions, Mo(VI) solution species also need to be investigated.

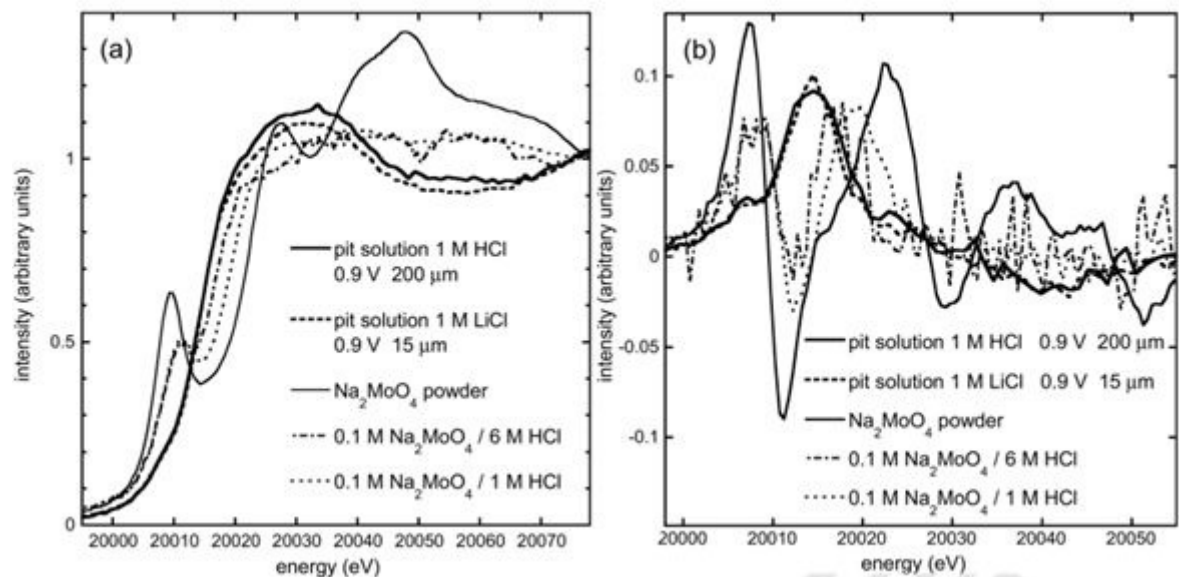


Figure 5.5 Normalised Mo K edge spectra for the solution inside 316L stainless steel artificial pits grown in 1 M HCl and 1 M LiCl at the potentials and locations indicated compared with 0.1 M Na_2MoO_4 solutions in 1 M and 6 M HCl and $\text{Na}_2\text{MoO}_4 \cdot 2\text{H}_2\text{O}$ powder. (a) Detail of the edge; (b) first derivative of the data shown in (a).

Figure 5.5 shows the spectra collected from pits grown in 1 M HCl and 1 M LiCl with sodium molybdate powder and Mo (VI) solution species. All Mo (VI) spectra have a very clear pre-edge peak compared with the featureless spectra of the pit solution in 1 M HCl and 1 M LiCl. This observation shows that it is unlikely that there are Mo (VI) species inside the

artificial pit of 316L stainless steel. Figure 5.6 shows the spectra of Mo (V) powder and Mo (V) solution species in 1 and 6 M HCl compared with a pit solution spectrum formed at 1 M HCl. Figure 5.6a and b show that Mo (V) powder has a featureless edge similar to the pit solution spectrum but has a completely different overall shape above the edge as shown in Figure 5.6c. Therefore the coordination of molybdenum species in the pit solution is not similar to MoCl_5 powder which has dimers of edge-shared MoCl_6 octahedra [173]. It can be seen in Figure 5.6b that the pre-edge shoulders for the first derivatives of the spectra for Mo (V) powder dissolved in HCl, are different from the pit solution spectrum. Therefore it is unlikely that the molybdenum oxidation state in the pits is +5.

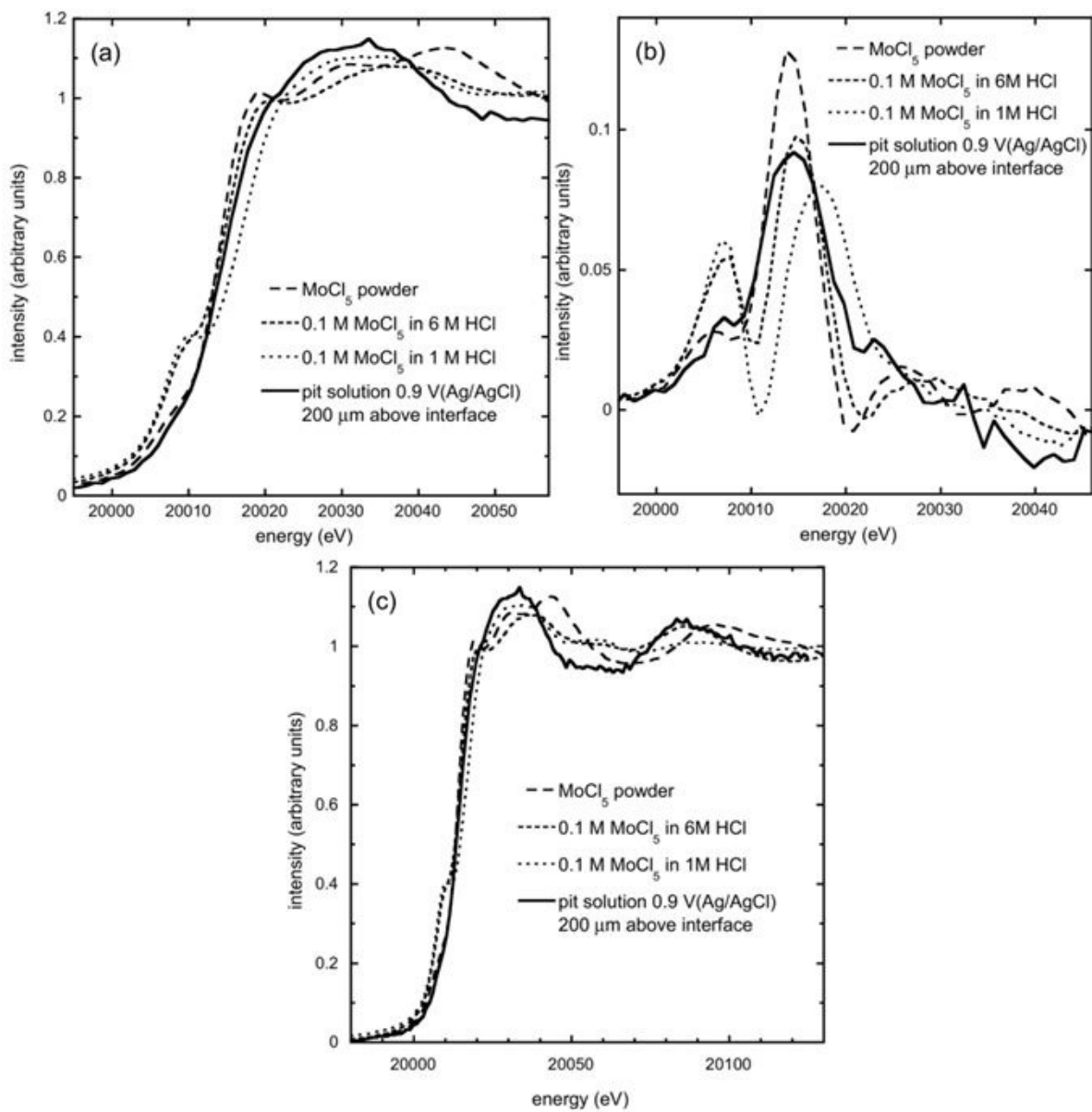


Figure 5.6 Normalised Mo K edge spectra for the solution 200 μm above the dissolving interface inside a 316L stainless steel artificial pit grown in 1 M HCl at 0.9 V(Ag/AgCl) compared with MoCl₅ powder and solutions of 0.1 M MoCl₅ dissolved in 1 M and 6 M HCl. (a) Detail of the edge; (b) first derivative of the data shown in (a); (c) region above the edge.

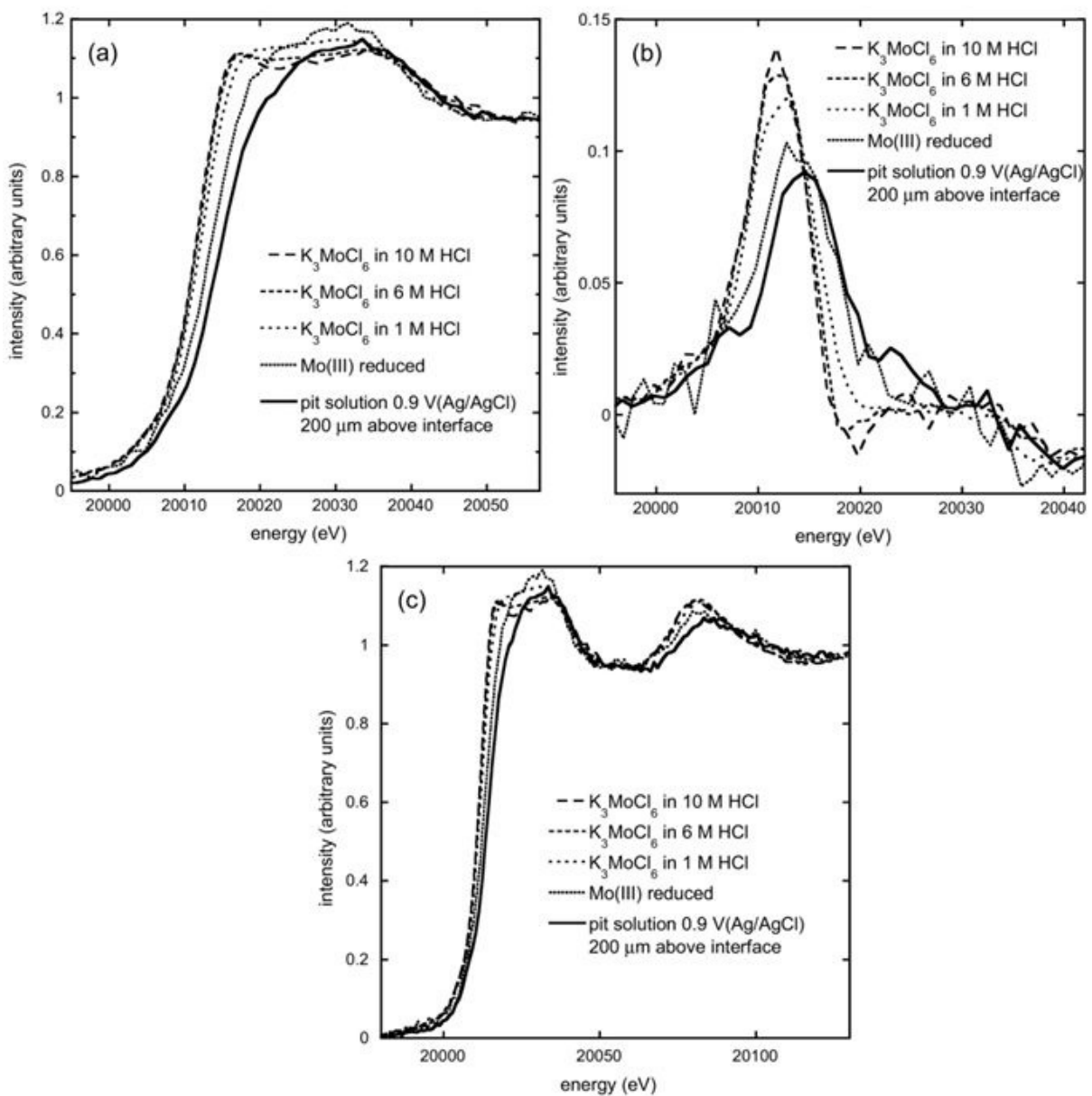


Figure 5.7 Normalised Mo K edge spectra for solution inside a 316L stainless steel artificial pit grown in 1 M HCl at 0.9 V(Ag/AgCl) compared with a solution of Mo(III) prepared by zinc reduction of a solution of 10 mM MoCl_5 and 0.1 M solutions of K_3MoCl_6 dissolved in 1, 6, and 10 M HCl. (a) Detail of the edge; (b) first derivative of the data shown in (a); (c) region above the edge.

The only molybdenum compounds remaining to be studied are those containing Mo (III).

Figure 5.7 shows the spectra of K_3MoCl_6 dissolved in 1, 6 and 10 M HCl solutions and Mo (III) reduced from Mo (V) solution prepared according to Kekesi et al. [160] procedure by zinc reduction, and compared with pit solution spectrum. It can be seen in Figure 5.7 that there is no pre-edge feature present in any of the Mo (III) spectra, but there are some

differences in the edge position and features at the top of the edge. It is notable that there is a very similar overall shape above the edge region between the Mo (III) reduced solution and the pit spectrum (Figure 5.7c). This is particularly clear in the first derivative of the spectra shown in Figure 5.7b.

5.3. Discussion

Sodium molybdate ($\text{Na}_2\text{MoO}_4 \cdot 2\text{H}_2\text{O}$) has a tetrahedral structure and its K-edge XANES spectra has a strong pre-edge peak corresponding to a $1s \rightarrow 4d$ dipole-forbidden transition [174]. Shinoda et al. [175] studied 1 M Na_2MoO_4 solution and reported a distorted octahedral structure for oxygen atoms by comparison with the MoO_3 crystalline structure very similar to the structure of $\text{Na}_6\text{Mo}_7\text{O}_{24}(\text{H}_2\text{O})_{14}$ [176]. These are the species that Kimura et al. [13] claimed are present in a 316L stainless steel artificial pit. However, it is very surprising to find these species at high chloride concentrations (11-12 M) [12, 38] and close to a pH value of 0 [8].

Figure 5.5 shows the very strong pre-edge peak for $\text{Na}_2\text{MoO}_4 \cdot 2\text{H}_2\text{O}$ at 20009.5 eV corresponding to tetrahedral co-ordination which is quite different from the featureless edge of Mo species inside the artificial pit. Spectra form HCl and LiCl solutions are very similar with a featureless edge, suggesting the same Mo species. The pre-edge feature for $\text{Na}_2\text{MoO}_4 \cdot 2\text{H}_2\text{O}$ solutions in 1 and 6 M HCl appears 1.7 eV above the pre-edge feature of $\text{Na}_2\text{MoO}_4 \cdot 2\text{H}_2\text{O}$, consistent with the result of Yokoi et al. [145] who carried out XANES and EXAFS measurements on $\text{Na}_2\text{MoO}_4 \cdot 2\text{H}_2\text{O}$ dissolved in a wide range of HCl concentrations. They related Mo species to the presence of MoO_2^{2+} ions in 1 and 2 M HCl concentrations whilst the decrease in pre-edge intensity in 4 and 6 M HCl concentrations was related to chloro complexation coordination of Mo species.

Jalilehvand et al. [144] and Yokoi et al. [146] has studied the Mo K-edge XANES for MoCl_5 powder dissolved over a wide range of HCl concentrations. In all HCl concentrations, pre-edge features were observed very similar to the pre-edge shoulder shown in Figure 5.6. These pre-edge shoulders were attributed to double-bridged Mo-O-Mo dimers in low HCl

concentrations and mononuclear Mo species in high HCl concentrations. Therefore, it is very unlikely that there are Mo (V) species in the artificial pit solution as there is no pre-edge feature present in the pit solution spectrum.

Since Mo (V) solution species have pre-edge features and a different overall shape above the edge compared with the pit solution spectrum, therefore Mo (III) species need to be investigated. K_3MoCl_6 has a known isolated octahedral structure coordinated with six chloride ions [177]. It may be seen in Figure 5.7 that Mo (III) solution species show good agreement with the corrosion pit spectrum as they have no pre-edge feature similar to pit solution. K_3MoCl_6 solutions have a lower edge energy position than the pit solution with two distinct peaks (~20012 and 20014 eV) in the first derivative of the spectra as shown in Figure 5.7b and show a sharp shape above the edge. Spectra of K_3MoCl_6 solutions also show an agreement in the post edge region but have larger peak amplitudes but at slightly lower energy values. In contrast, Mo (III) solution species formed by zinc reduction have very good agreement in edge position (Figure 5.7) and the shape of the post edge region (Figure 5.7c) suggesting that the pit solution species is similar to these species formed by zinc reduction of Mo (V). Therefore, the oxidation state of molybdenum inside the corrosion pit of 316L stainless steel is +3.

This observation is consistent with the work of Wang et al. [172] who simulated the chemistry of localised corrosion sites to develop E-pH diagrams for molybdenum species by titration of solutions with HCl and NaOH to change the pH at 25 °C. HCl was used to decrease the pH in their simulation which is similar to the corrosion pit conditions in an artificial pit. Their results indicate that Mo^{3+} is thermodynamically stable in solutions with $pH < 2$ at similar potentials of pitting of 316L stainless steel.

While the XANES spectra give good evidence for the formation of Mo (III) in corrosion pits, the data are not sufficient to determine the exact coordinated ion environment around molybdenum. However, the clear difference between the pit solution and MoCl_6^{3-} solution suggest that the Mo (III) in solution may be coordinated by water molecules and chloride ligands.

The aim of this work is to use the XANES method to study the mechanism by which molybdenum improves the corrosion resistance of 316L stainless steel. These results are inconsistent with the claim that there are Mo (VI) species inside the pits and indicates that there is no systematic change in Mo chemistry close to the interface. These observations are therefore more consistent with claims that monolayer molybdenum species block anodic dissolution in 316L stainless steel pits [14, 26, 44, 45, 50, 51, 57]. However, the technique has insufficient resolution to detect such a species.

5.4. Conclusions

1. The Mo K-edge XANES spectra of solution in 316L stainless steel artificial pits shows the presence of Mo (III) species.
2. High spatial resolution of the measurements (3.5 μm in the vertical direction) through the pit and close to the interface did not show any evidence of different Mo-containing species close to the interface.
3. The Mo K-edge spectra of the pit solution did not show any presence of Mo (VI) polymolybdates, which have been claimed to inhibit the corrosion of 316L stainless steel.
4. The spatial resolution is not enough to detect any monolayer Mo species that have been claimed to block dissolution of 316L stainless steel within a pit [45].

6. Spectroscopy of Ti in human tissue and artificial corrosion pits

6.1. Introduction

Titanium and its alloys are used extensively to manufacture biomedical prostheses. However, concerns have been raised regarding the potential biological impact of Ti ions and particles that may accumulate in soft tissues as a result of corrosion and wear processes. In order to investigate these risks further, it is necessary to identify the species that are present in tissue, and the species that are generated by localised corrosion of titanium alloys, so that the effect of both types of species on human cells can be determined. In this chapter, XANES measurements on titanium artificial pits are investigated and compared with results obtained from tissues adjacent to knee, BAHA (bone-anchored hearing aid) and dental implants.

6.2. Results

6.2.1. Ti reference compounds

Figure 6.1 shows the XANES spectra of commercially pure titanium reference foils used for comparison with spectra from artificial pits and human tissues. The XANES spectrum for 5 µm foil (measured in transmission) was used for comparison with XANES spectra from body tissues, while the 50 µm foil spectrum (measured in fluorescence) is from the foil that was corroded in the titanium artificial pit. All the spectra were calibrated to the inflection point of titanium at 4966 eV [167]. Features such as the pre-edge peak and oscillations are at identical energies, but the spectrum from the 50 µm foil is compressed above the edge owing to self-absorption effects.

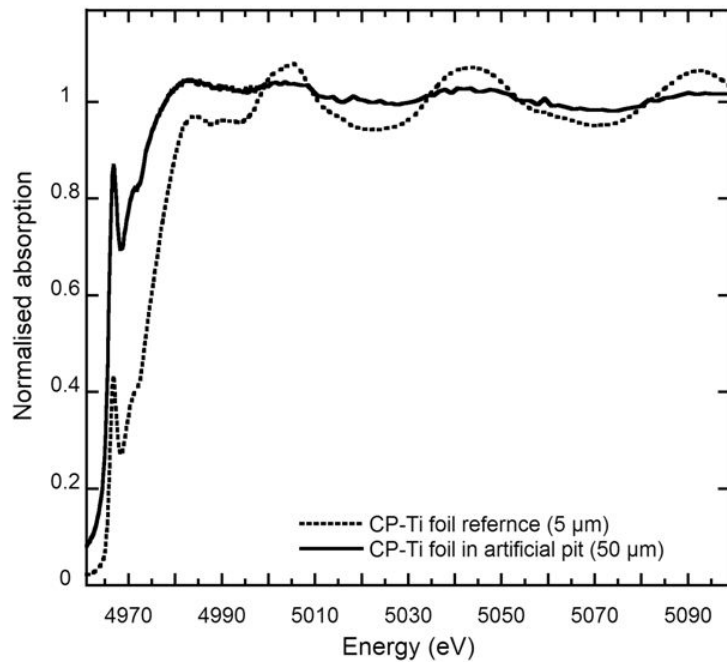


Figure 6.1 Normalised XANES Ti K-edge spectra of CP-Ti 5 μm foil reference (measured in transmission) and CP-Ti 50 μm foil in artificial pit (measured in fluorescence)

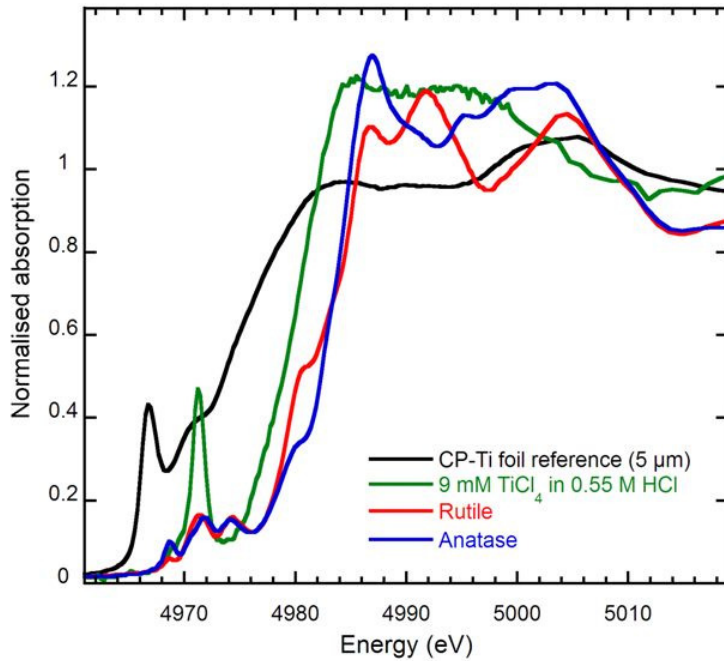


Figure 6.2 Normalised XANES Ti K-edge spectra of CP-Ti reference foil (black), 9 mM TiCl_4 in 0.55 M HCl solution (green), rutile (red) and anatase (blue). All spectra were measured in transmission geometry except TiCl_4 which was measured in fluorescence geometry.

Figure 6.2 shows the XANES spectra of titanium dioxide solid standards (rutile and anatase) and a solution reference (9 mM TiCl_4 in 0.55 M HCl). It can be seen that rutile and anatase

have the same edge position 4 eV above the TiCl_4 edge position. However, rutile and anatase show three well-resolved pre-edge features at ~ 4968.7 , 4971.5 and 4974.2 eV whilst TiCl_4 has a single intense pre-edge peak at 4971.5 eV.

6.2.2. Ti artificial pit

The preparation of titanium artificial pits was described in Chapter 3. Figure 6.3 shows a potentiodynamic sweep on a titanium sample from 0 to 12 V(Ag/AgCl) in 1 M HCl. It can be seen that the current does not show a significant increase before 2 V and then slightly increases above 2 V, possibly due to the formation of metastable pits. It then shows a substantial increase above 10 V(Ag/AgCl), leading to general attack within the artificial pit.

Figure 6.4(a) shows the current-time behaviour of titanium artificial pit after applying 9 V(Ag/AgCl). The background current is very low, but there are occasional current spikes. The titanium artificial pit starts to undergo general corrosion after applying 10 V(Ag/AgCl) as shown in Figure 6.4(b). As the titanium dissolves, a concentrated highly acidic solution rich in titanium dissolution products and chloride ions develops in the cavity.

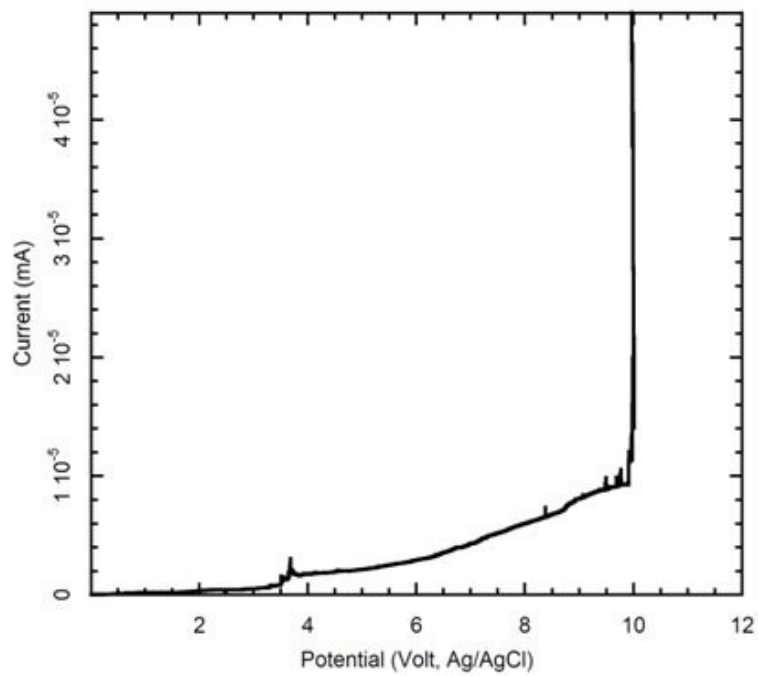


Figure 6.3 Potentiodynamic sweep on titanium from 0 to 12 V(Ag/AgCl), scan rate 10 (mV/s) in 1 M HCl solution.

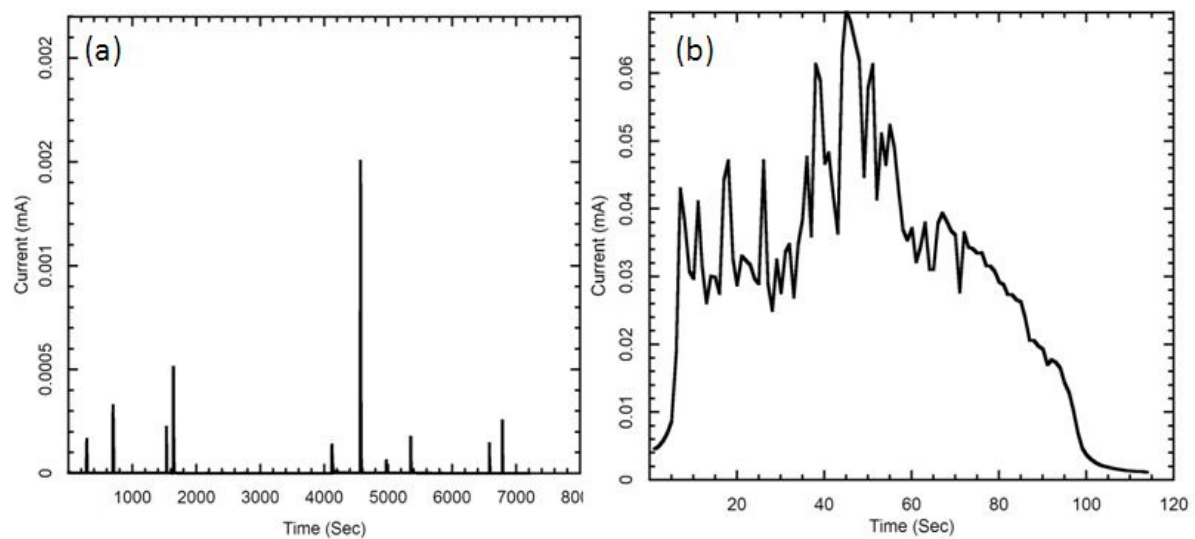


Figure 6.4 Current-time behaviour of Cp-Ti artificial pit grown at (a) 9V (Ag/AgCl) (b) 10 V (Ag/AgCl) in 1 M HCl solution

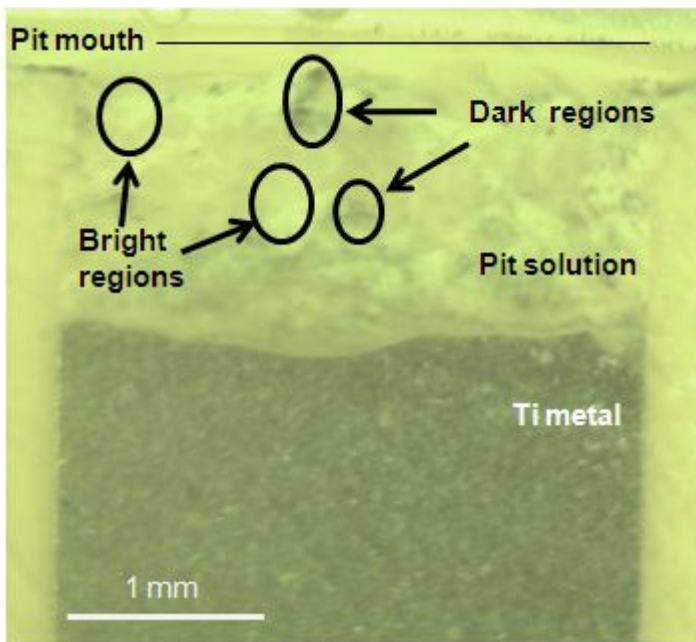


Figure 6.5 Optical image of a typical titanium artificial pit grown at 7 V (Ag/AgCl) in 1 M HCl. The black solid line at the top shows the original sample edge position before dissolution and the oval shapes show characteristic bright and dark regions of the type used for XANES measurements.

Figure 6.5 shows an optical micrograph of the titanium artificial pit used for XANES measurements initially corroded at 10 V (Ag/AgCl) and then stably grown at 7 V (Ag/AgCl). It may be seen that the pit interface is not as uniform as that for a 316L stainless steel pit. The solid black line at the top shows the position of the original sample of the titanium foil (pit mouth) before electrochemical dissolution in 1 M HCl. Near the mouth of the pit above and below the solid black line, the solution may be seen to be fairly clear but bright and dark regions are visible inside the pit as shown in the photograph. XANES measurements were carried out at dark and bright spots inside the pit at approximately 1 and 2 mm above the interface as well as the bright spots at approximately 1 mm above the pit mouth. These bright and dark spots were selected by using the optical microscope aligned with the x-ray beam and focused on the pit region.

6.2.3. Ti XANES in artificial pits

XANES spectra were obtained from various regions inside and above the pits. XANES measurements were carried out in two artificial pits and the second pit showed similar results to those obtained from the first pit. In some cases, the spectra were similar to titanium oxides while in others, spectra characteristic of Ti metal were found. Some spectra showed a mixture of metal, titanium oxides and TiCl_4 as summarised in Table 6.1. It should be noted that the “dark” spots were always collected above “bright” regions. The XANES spectra were acquired at six spots in “bright” regions and four different types of spectra were found as shown in Figure 6.6.

Table 6.1 Summary of the number of XANES measurements for different corrosion product components inside and above the pit mouths for a Ti artificial pit grown at 7 V (Ag/AgCl) (The letter in the bracket indicates the dominant species)

Corrosion products	M	R + A + Cl	M + R + A + Cl
Dark spots inside the pit	3	-	-
Bright spots inside the pit	-	2(A)	4(A)
Spots above the pit mouth	-	3(A), 1(R)	1(A)

(M: Metal, R: Rutile, A: Anatase, Cl: 9 mM TiCl_4 in 0.55 M HCl)

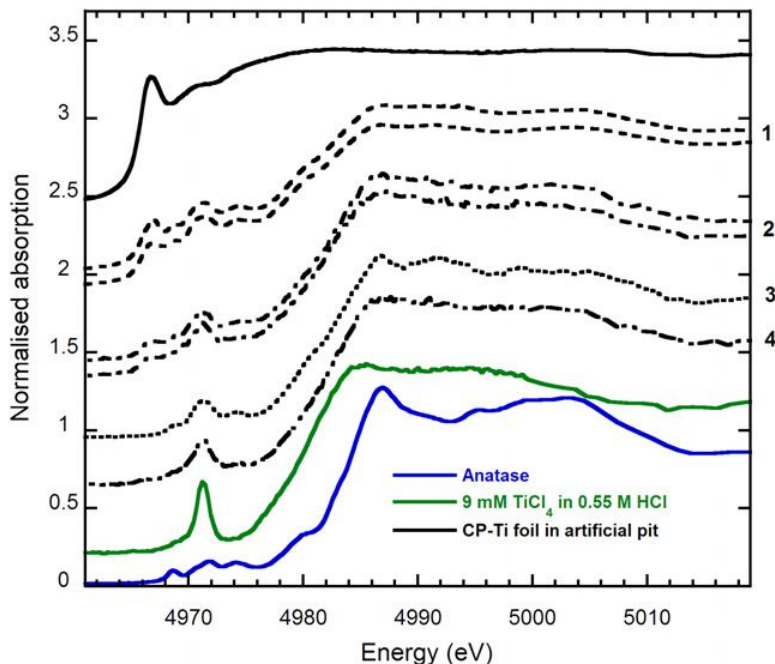


Figure 6.6 Normalised Ti K edge XANES spectra (types 1, 2, 3 and 4) at bright regions inside the titanium artificial pit grown at 7 V (Ag/AgCl) in 1 M HCl, compared with anatase (blue), 9 mM TiCl_4 in 0.55 M HCl solution (green) and CP-Ti corroding foil (black solid line).

The spectra type 1 and 2 are similar with a stronger metallic pre-edge peak for type 1 and a sharper middle pre-edge peak at type 2. However, spectrum type 3 is a mixture of anatase, rutile and TiCl_4 with no indication of any metal. Type 2 spectra can be fitted by a linear combination of spectra for titanium metal, anatase, rutile and TiCl_4 as shown in Figure 6.7. The quality of the fit is demonstrated by the residual spectrum (the difference between the observed spectrum and a linear combination of standards). Figure 6.8 shows the linear combination of titanium standards for the typical spectrum type 2 including titanium metal, anatase, rutile and TiCl_4 , mostly dominated by TiCl_4 and anatase. The spectrum type 4 is quite different from all other regions and seems to be the mixture of TiCl_4 and another unknown species as it shows the same sharp pre-edge peak of TiCl_4 with no sign of similar pre-edge of rutile or anatase.

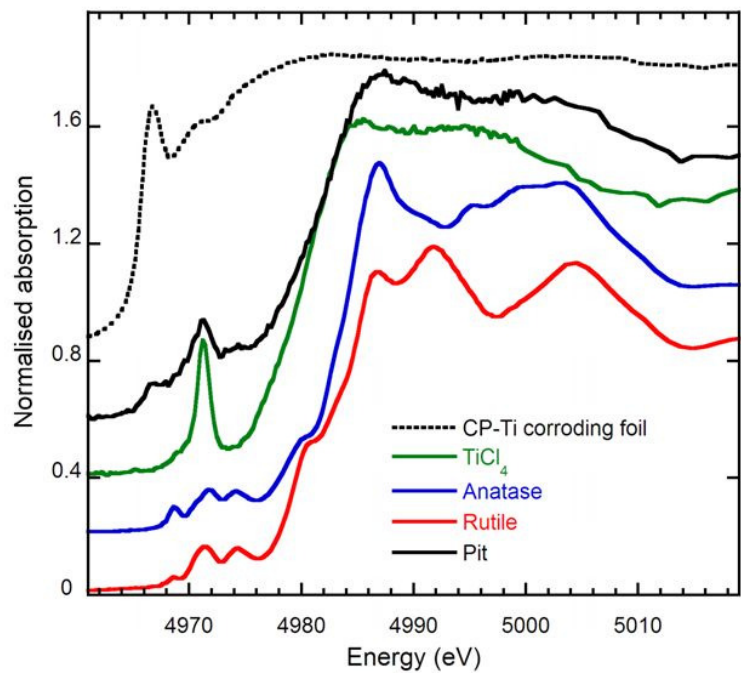


Figure 6.7 Normalised Ti K edge XANES spectra of CP-Ti corrodin foil (black dashed line), 9 mM TiCl_4 in 0.55 M HCl solution (green), anatase (blue) and rutile (red) compared with a type 2 spectrum of a bright regions in a titanium artificial pit grown at 7 V (Ag/AgCl) in 1 M HCl.

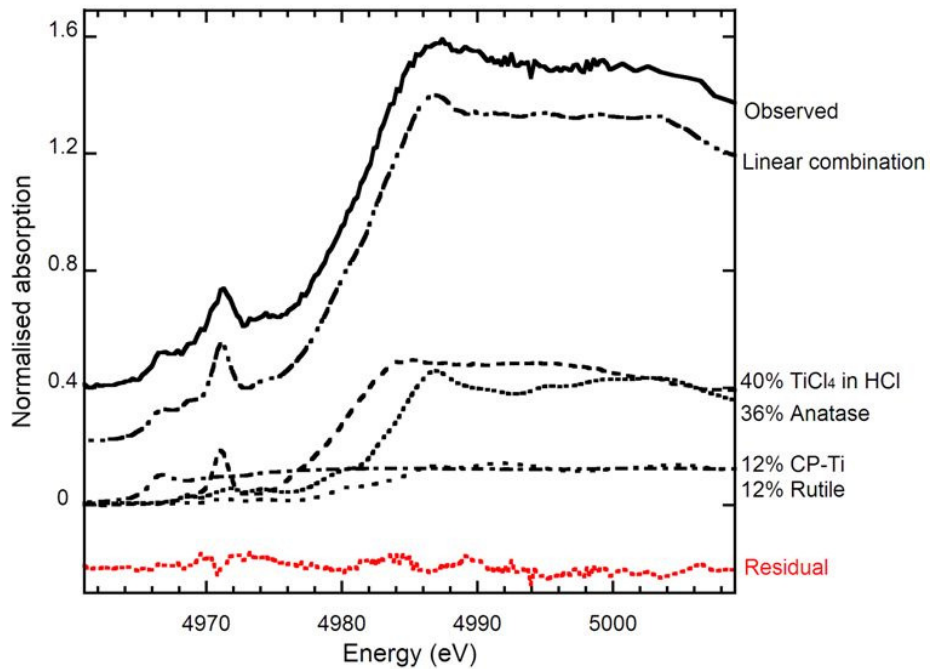


Figure 6.8 A linear combination fit of titanium standards for a typical XANES spectrum type 2 of a bright region inside a titanium artificial pit grown at 7 V (Ag/AgCl) in 1 M HCl.

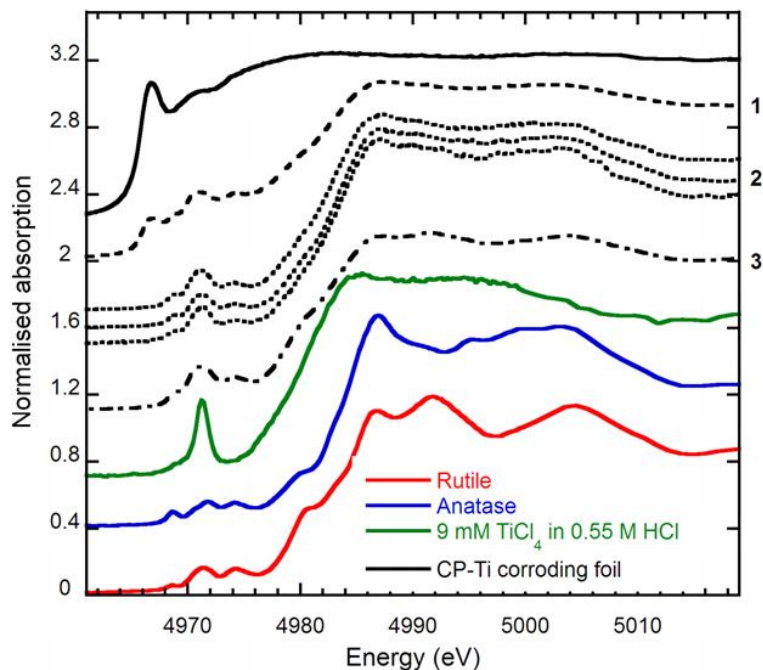


Figure 6.9 Normalised Ti K edge XANES spectra (types 1, 2 and 3) above the mouth of the titanium artificial pit grown at 7 V (Ag/AgCl) in 1 M HCl, compared with rutile (red), anatase (blue), 9 mM TiCl₄ in 0.55 M HCl solution (green) and CP-Ti corrodng foil (black).

Measurements taken at various places above the pit mouth showed that there were three types of spectra as shown in Figure 6.9. Comparison with standard spectra shows:

- The typical spectrum of type 1 is a mixture of rutile, anatase, TiCl₄ and titanium metal as the metallic pre-edge peak appears at 4966 eV.
- The typical spectra of type 2 are similar to anatase and are the linear combination fits of anatase and TiCl₄ as they have middle pre-edge peak with higher intensity comparing to titanium oxides.
- The spectrum type 3 is different and more similar to rutile and is the linear combination of rutile and TiCl₄ as it has a pre-edge peak with higher intensity.

These spectra show the variety of titanium species that are present above the pit mouth. Figure 6.10 shows the linear combination fit of titanium standards to a typical type 2 spectrum

above the pit mouth and shows that there are anatase, rutile and TiCl_4 present, but mostly dominated by anatase.

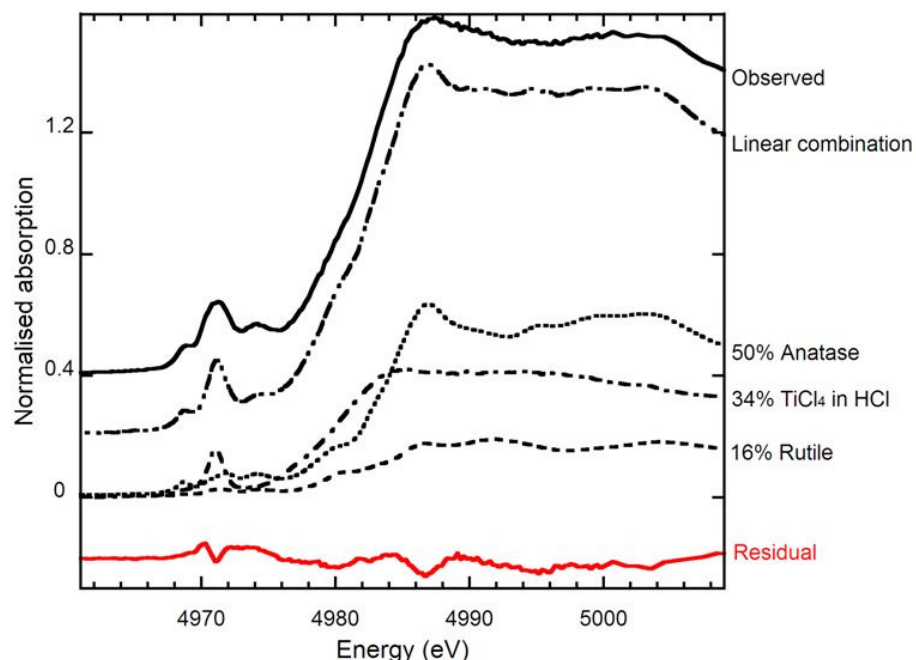


Figure 6.10 A linear combination fit of titanium standards for a typical XANES spectrum of a bright region above the pit mouth of a titanium artificial pit grown at 7 V (Ag/AgCl) in 1 M HCl.

Figure 6.11 shows the typical pit spectra for several dark spots inside the titanium artificial pit. The XANES measurements for dark spots were carried out at three different dark regions as marked and shown in Figure 6.5. The pre-edge peak appears at 4966 eV at the same position as the metallic pre-edge peak. This shows the presence of metal fragments in dark regions following the dissolution of titanium metal. However, these spectra are not pure metallic spectra: Figure 6.12 shows that the XANES spectrum for a typical spectrum in a dark region is a linear combination of titanium metal, rutile and anatase but with more than 90% of the metallic component. The XANES spectra from the dark regions show clear evidence of non-linearity since the intensity of the pre-edge peak is proportionally larger than observed in

the transmission mode spectra. However, the self absorption is less than that for the uncorroded foil measured in fluorescence mode.

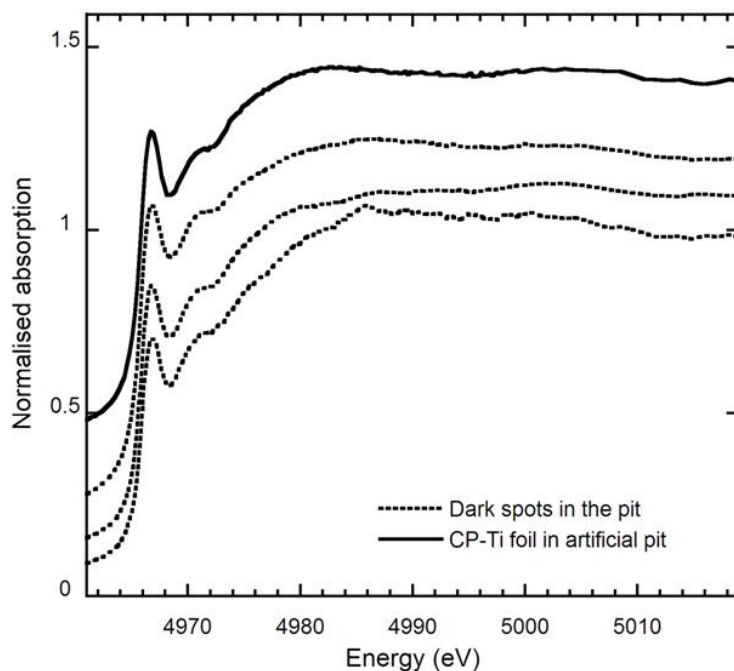


Figure 6.11 Normalised Ti K-edge XANES spectra of typical dark spots inside a titanium artificial pit grown at 7 V (Ag/AgCl) in 1 M HCl, compared to CP-Ti foil in artificial pit.

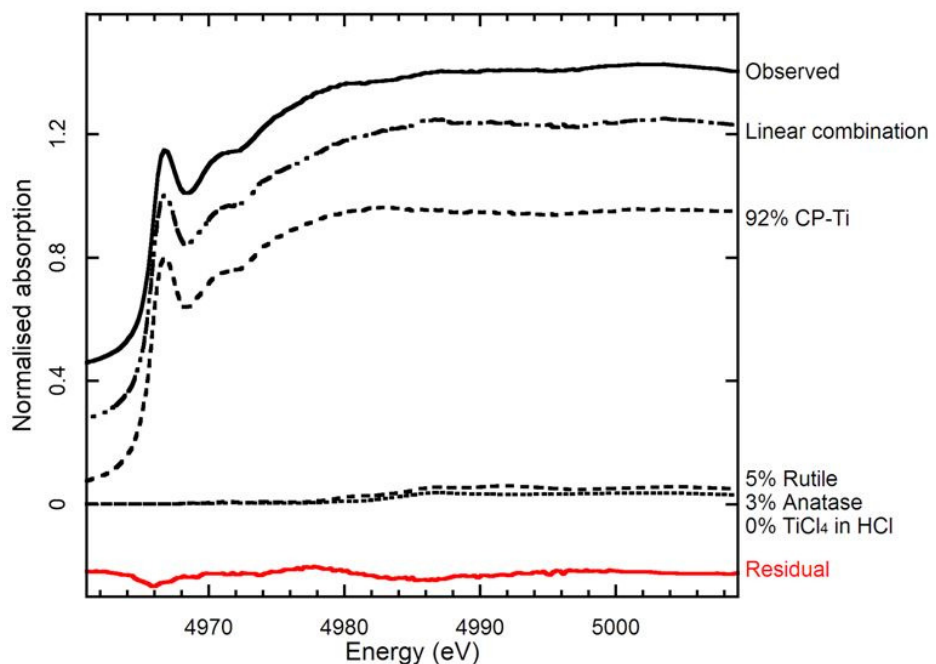


Figure 6.12 A linear combination fit of titanium standards for a typical XANES spectrum of a dark region inside a titanium artificial pit grown at 7 V (Ag/AgCl) in 1 M HCl.

6.2.4. Ti XANES in BSA and Ringers solutions

Ti species found in tissues around implants are likely to be the result of reactions between species generated during localised corrosion of Ti and proteins found in the body. A simple simulation of this has been carried out by reacting TiCl_4 (found in pits) with bovine serum albumin (BSA). Similar measurements were carried out by reacting TiCl_4 and Ringer's solution as this is often used to simulate the inorganic constituents of extracellular fluid. XANES measurements were carried out in Ringer's solution after reaction with TiCl_4 solution and the pit solution as shown in Figure 6.13. It can be seen that after reaction between Ringers solution and TiCl_4 , the pre-edge peak appears similar to TiCl_4 but it has a sharper peak above the edge similar to anatase. The XANES spectrum after the reaction can be fitted to a mixture of TiCl_4 and anatase and is mostly dominated by the TiCl_4 spectrum. Table 6.2 shows the components and dominant species of the solution after mixing the Ringer's solution with a TiCl_4 solution.

Table 6.2 Summary of XANES measurements following mixing Ringer's solution with TiCl_4 and BSA with TiCl_4 and titanium artificial pit solution (The letter in the bracket indicates the dominant species)

Solutions	A + Cl	R
BSA + TiCl_4 after mixing	1 (A)	-
BSA + TiCl_4 (after 40 minutes)	1 (A)	-
Ringers + TiCl_4	1(Cl)	-
BSA + pit solution	-	1

(A: Anatase, R: Rutile , Cl: 9 mM TiCl_4 in 0.55 M HCl)

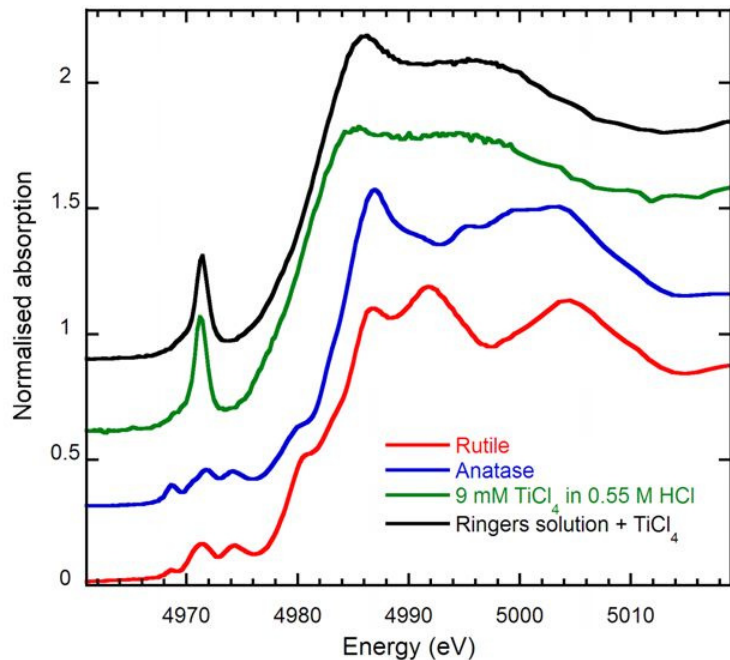


Figure 6.13 Normalised Ti K edge XANES of Ringer's solution following addition of 9 mM TiCl_4 in 0.55 M HCl compared with rutile, anatase and TiCl_4 reference spectra.

XANES spectra were also collected immediately and 40 minutes following addition of BSA to the TiCl_4 solution and after adding it to the pit solution as indicated in Figure 6.14 . The pre-edge peak intensity and positions show the presence of TiCl_4 (from the presence of the pre-edge peak) but it is more similar to anatase above the edge. In both cases, the spectrum can be fitted to a mixture of TiCl_4 and anatase, but mostly dominated by anatase. BSA was also added to the pit solution which gave a spectrum similar to the rutile standard as shown in Figure 6.14. The components of the solution after adding BSA to TiCl_4 and pit solution are summarised in Table 6.2.

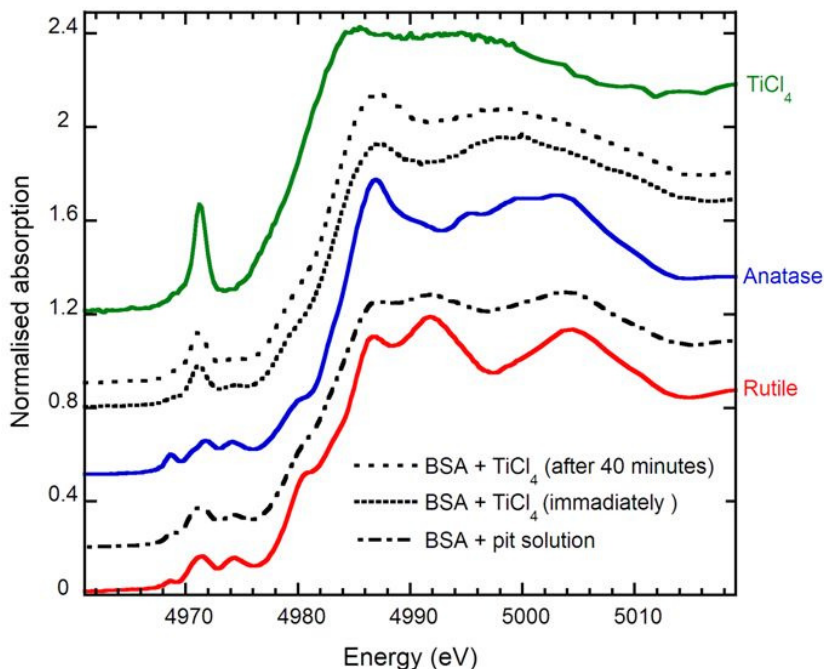


Figure 6.14 Normalised Ti K edge XANES of BSA added to 9 mM TiCl₄ in 0.55 M HCl and titanium artificial pit solution compared to rutile (red), anatase (blue) and 9 mM TiCl₄ in 0.55 M HCl solution.

6.2.5. Ti XANES in neutrophil cells

Neutrophil cells were used as a model for the types of cells found around the implants. These cells were grown in the presence of Ti species (anatase) to simulate Ti corrosion products in the body and determine the effect of Ti species on the cell metabolism. Figure 6.15 shows the Ti K-edge XANES spectra of neutrophil cells after culturing in the presence of 100 or 1000 ppm anatase. The spectrum shown above the rutile standard was measured following cultivation in the presence of 100 ppm anatase, but shows a spectrum more similar to rutile standard while the other 100 ppm spectrum has a very sharp peak above the edge similar to anatase (the spectrum at the top). The other spectra containing 1000 ppm anatase are quite similar to the anatase standard at both pre-edge and post-edge regions. The titanium-containing components of the neutrophil cell cultures are summarised in Table 6.3.

Table 6.3 Summary of number of XANES measurements including titanium components in neutrophil cells (The letter in the bracket indicates the dominated species)

Cells	Metal	Metal+A	Metal+R	R+A	R
Neutrophil cells	-	-	-	3(A)	1

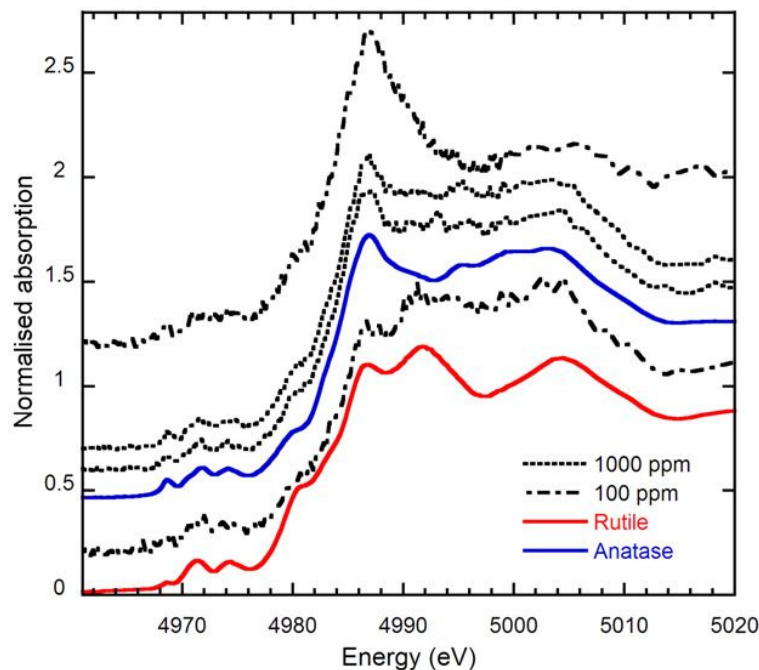


Figure 6.15 Normalised Ti K edge XANES spectra of neutrophil cells with 100 and 1000 ppm of anatase compared to rutile (red) and anatase (blue)

6.2.6. XRF mapping of human tissues

The titanium distribution in human tissue around a knee implant, a dental implant and a bone-anchored hearing aid (BAHA) were investigated by XRF mapping followed by XANES measurements at sites of highest concentration of Ti, and also at regions with low levels of titanium. Figure 6.16 shows an example of the heterogeneous distribution of titanium in tissue around a failed knee implant. Figure 6.17 shows the distribution of titanium species in tissue taken from around a BAHA implant. In both figures, point A represents a higher and B

represents a lower concentration of Ti where XANES measurements were carried out. The intensity scale represents the number of counts at each pixel.

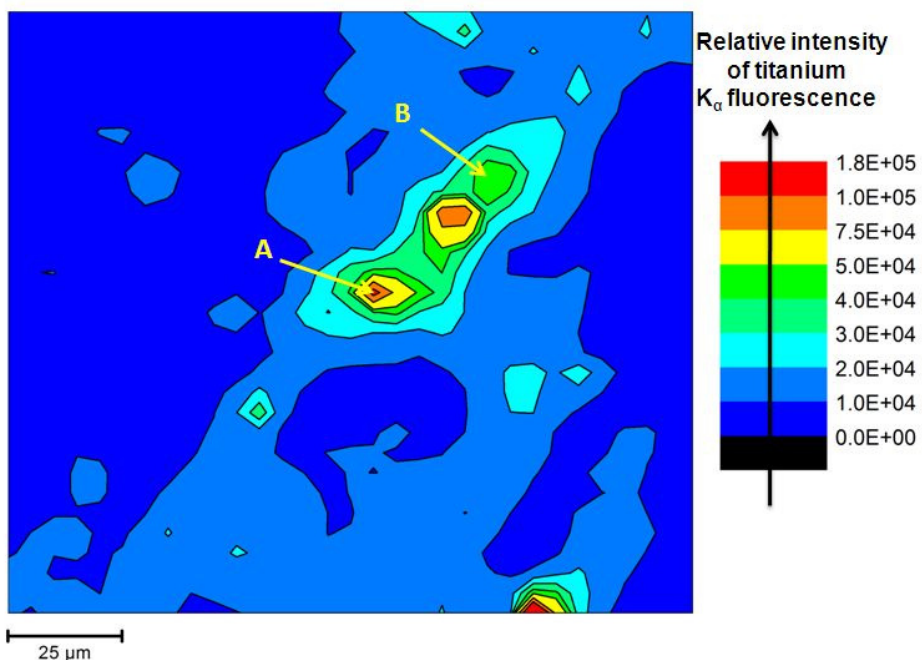


Figure 6.16 Ti XRF mapping of a typical tissue taken from a failing knee implant (A: high concentration of titanium; B: low concentration of titanium)

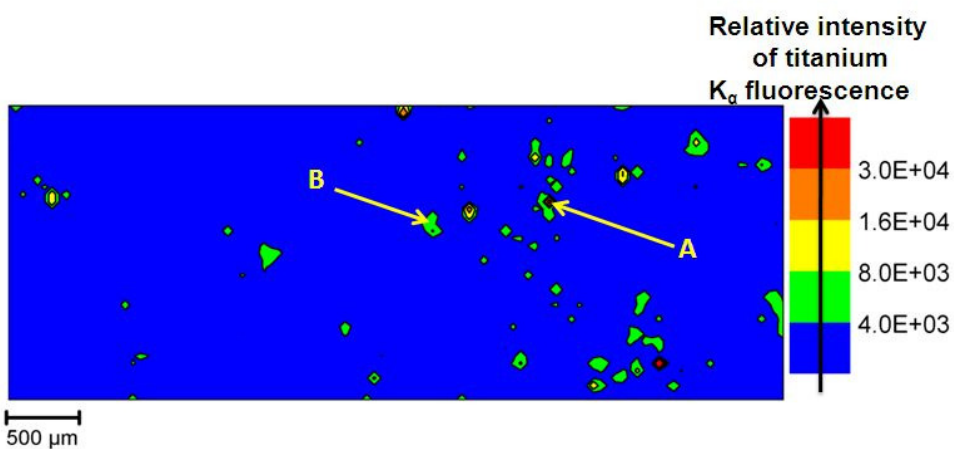


Figure 6.17 Ti XRF mapping of a typical tissue taken surrounding the BAHA implant (A: high concentration of titanium; B: low concentration of titanium)

6.2.7. Ti XANES in human tissues

XANES spectra were obtained at the sites of highest concentration of Ti, and also at regions where lower levels were found. In some cases the spectra were similar to rutile while in some tissues metallic fragments of titanium were found. It was observed that some spectra are also the mixture of metal and titanium oxide. While the discovery of metal fragments is not surprising for a knee joint, it is more surprising to find metallic species around BAHA tissues, which are not involved with any mechanical wear processes. Table 6.4 gives a summary of different titanium species found in knee, BAHA and dental tissues.

Table 6.4 Summary of titanium components in different type of body tissues (The letter in the bracket indicates the dominant species)

Tissues	Metal	Metal+ U	Metal+R	R+A	Unknown	R
knee tissues near implant	-	2(M+U)	-	4	3	4
Knee tissues distant from implant	-	4(M+U)	3	-	-	5
BAHA	1	2(M+U)	-	-	-	1
Dental	-	-	-	-	2	-

(M:Metal, R:Rutile, A:Anatase and U:Unknown)

6.2.7.1. Knee tissues

Samples of knee tissues were taken from two regions, one near to the Ti implant and the other further away. Some of the XANES spectra of the tissues both near to and distant from the knee implants showed similar spectra to rutile as shown in Figure 6.18 and Figure 6.19 respectively. Sixteen spectra out of twenty five measurements for the knee tissues showed spectra similar to rutile, rutile+metal or rutile+anatase as summarised in Table 6.4.

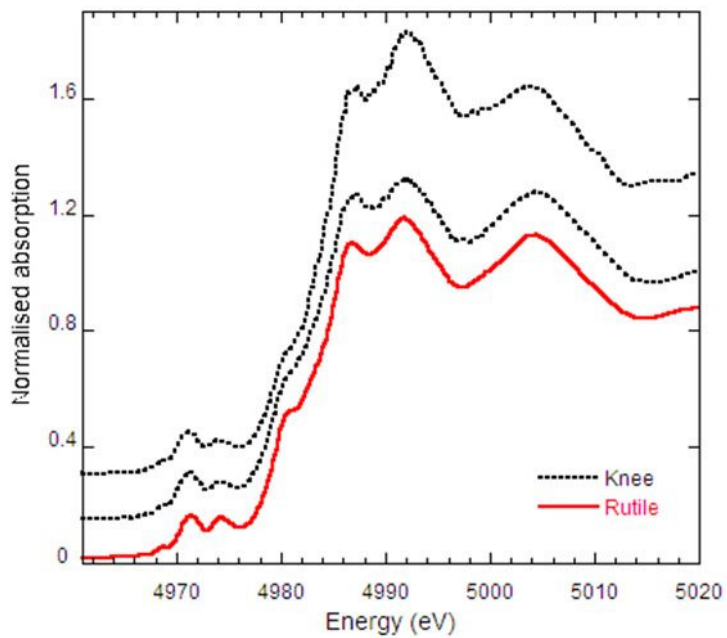


Figure 6.18 Normalised Ti K edge XANES spectra of tissues distant from knee implant compared with rutile (red)

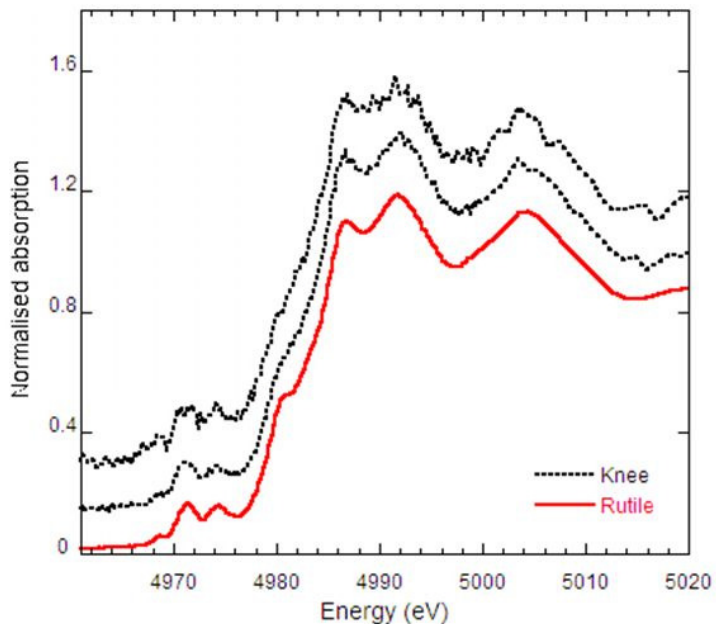


Figure 6.19 Normalised Ti K edge XANES spectra of tissues near the knee implant compared with rutile (red)

The XANES spectra of the knee tissues also showed evidence of metallic titanium for six measurements out of twenty five for both type of tissues near and distant from the implant. It can be seen that a metallic pre-edge peak is present at 4966 eV, similar to the titanium metal

pre-edge peak. The typical XANES spectra showing metallic species in both types of knee tissues are shown in Figure 6.20 and Figure 6.21. These spectra are likely to be a linear combination of metallic titanium and unknown species as they couldn't be fitted to mixture of metallic titanium, rutile and anatase.

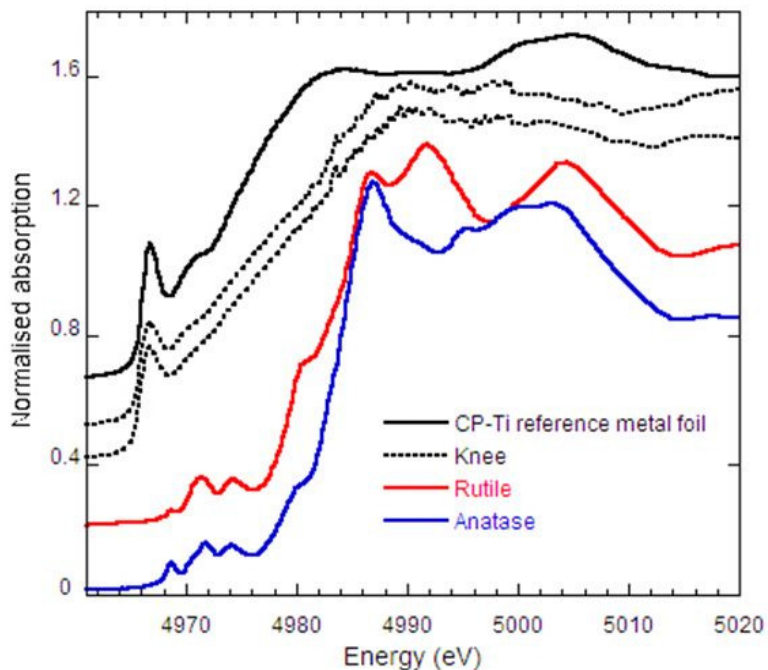


Figure 6.20 Normalised Ti K edge XANES spectra of tissues near the knee implant compared with rutile (red) and anatase (blue)

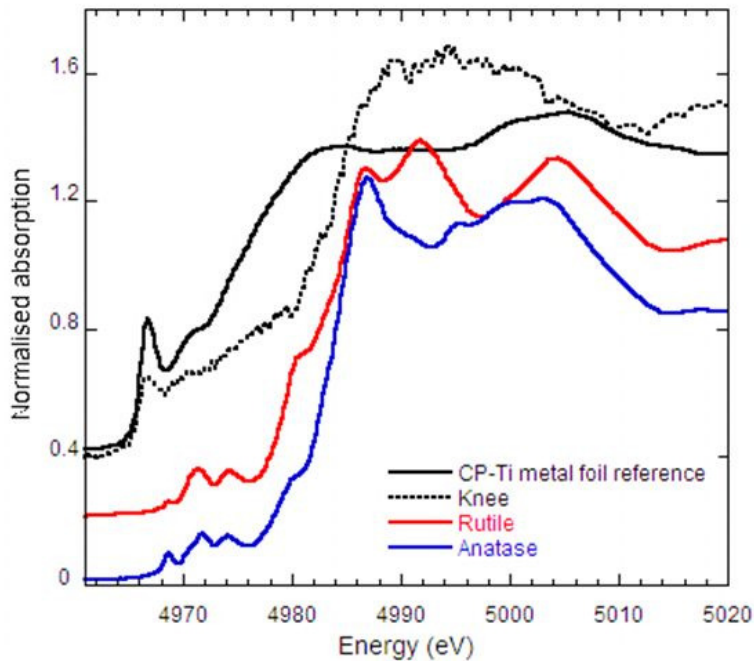


Figure 6.21 Normalised Ti K edge XANES spectra of tissues distant from the knee implant and titanium standards compared to rutile (red), anatase (blue) and CP-Ti reference foil (black)

Figure 6.22 shows XANES spectrum found in knee tissues near the implant that is linear combination of metal and rutile and mostly dominated by rutile as the main component. There were three spectra out of twenty five measurements that showed a combination of metallic titanium and rutile. There were also found four consistent measurements out of twenty five that were a linear combination of rutile and anatase as shown in Figure 6.23. It can be seen from all the measurements that, there are different types of spectra similar to rutile, Ti metal or a linear combination of rutile, anatase and Ti metallic foil. However, two spectra shown in Figure 6.24 were different from the titanium reference compounds and it was difficult to determine the species present. There is no evidence for the presence of metal but the pre-edge and white line regions are less clearly defined.

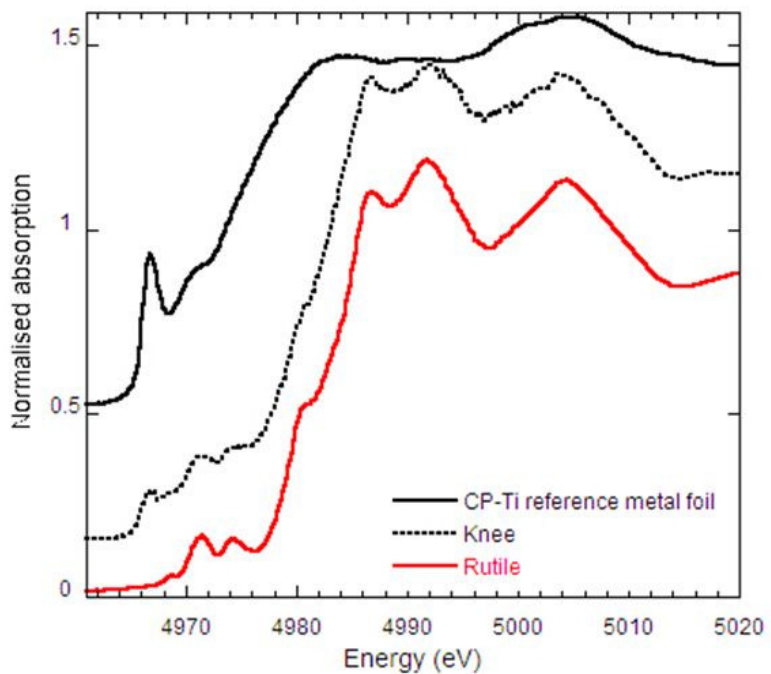


Figure 6.22 Normalised Ti K edge XANES spectrum of tissue near a knee implant compared with rutile (red) and CP-Ti reference foil (black)

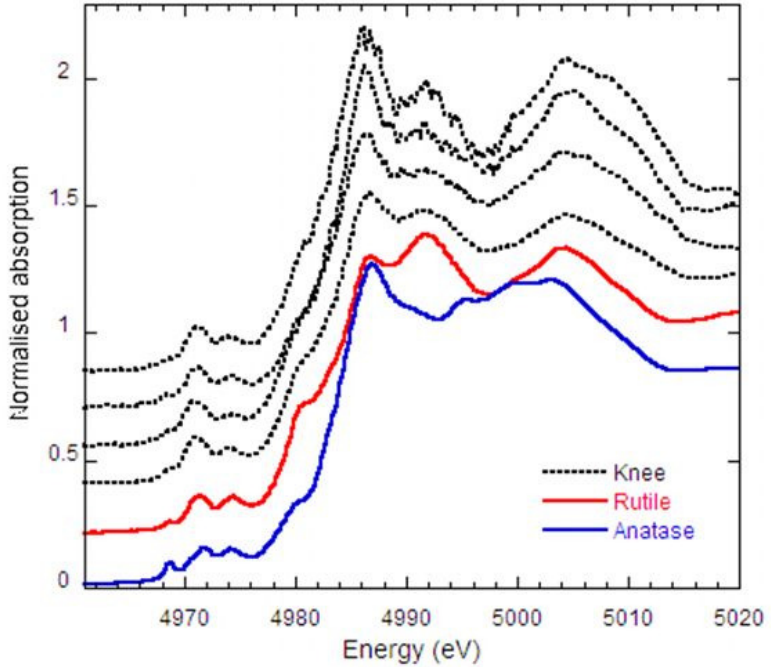


Figure 6.23 Normalised Ti K edge XANES spectra of tissues distant from the knee implant compared to rutile (red) and anatase (blue)

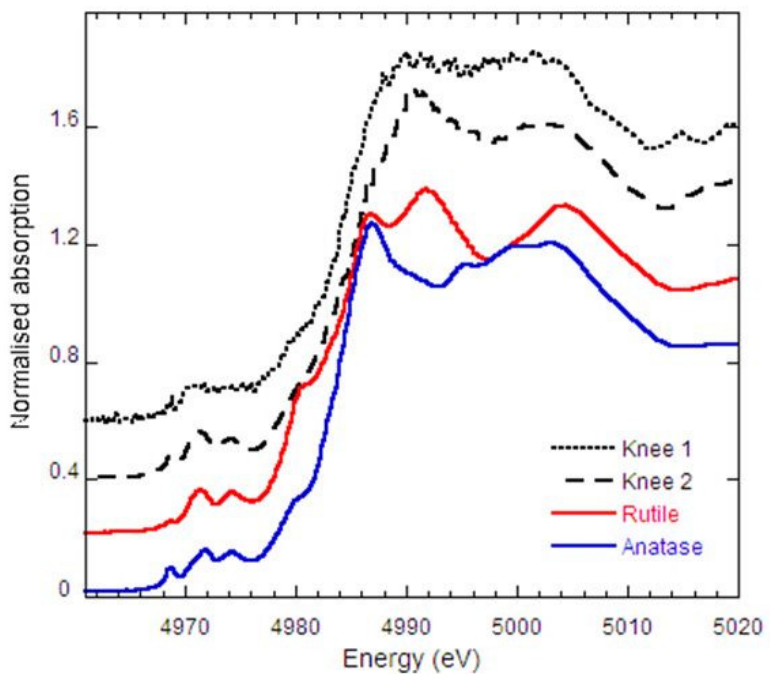


Figure 6.24 Normalised Ti K edge XANES spectra of tissues distant from the knee implant compared with rutile (red) and anatase (blue)

6.2.7.2. Dental tissues

Figure 6.25 also shows the XANES spectra of dental tissue obtained from two different regions of tissue. It can be seen that both spectra are different from previous spectra found for knee tissues and titanium reference compounds. It is very difficult to determine if these spectra are similar to any of the standards but the presence of a metallic pre edge feature at 4966 eV suggests the presence of metallic titanium in dental tissues.

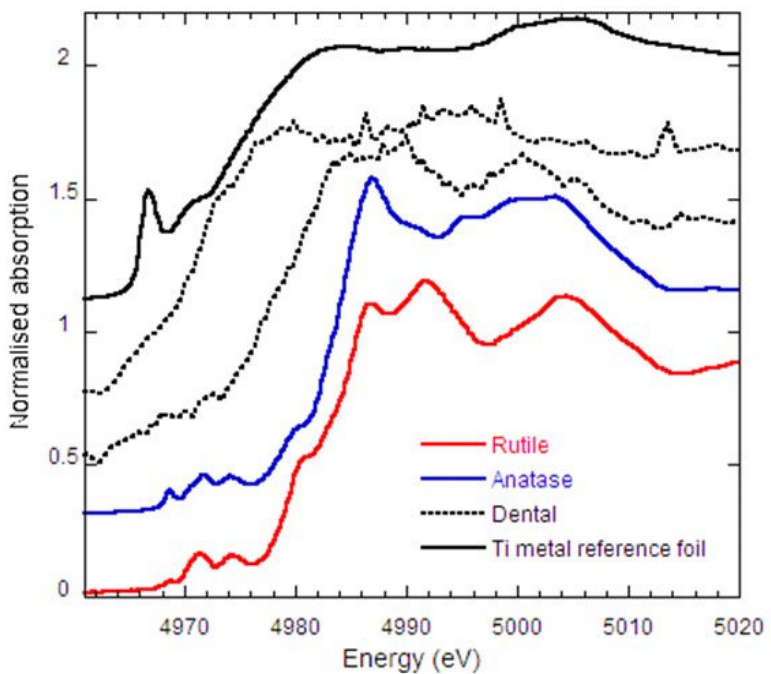


Figure 6.25 Normalised Ti K edge XANES spectra of dental tissues

6.2.7.3. BAHA tissues

The XANES spectra of BAHA tissues are illustrated in Figure 6.26 at three different regions showing three different spectra. The spectrum of region 1 is very similar to the Ti metallic reference material as the pre-edge peak at 4966 eV has a similar shape at region above the edge. Both spectra of region 2 show the metallic pre-edge peak at 4966 eV but have a different shape above the edge region. However, it is very difficult to distinguish features from the Ti reference standards. The spectrum of region 3 is very similar to the rutile standard and shows the same peaks as rutile.

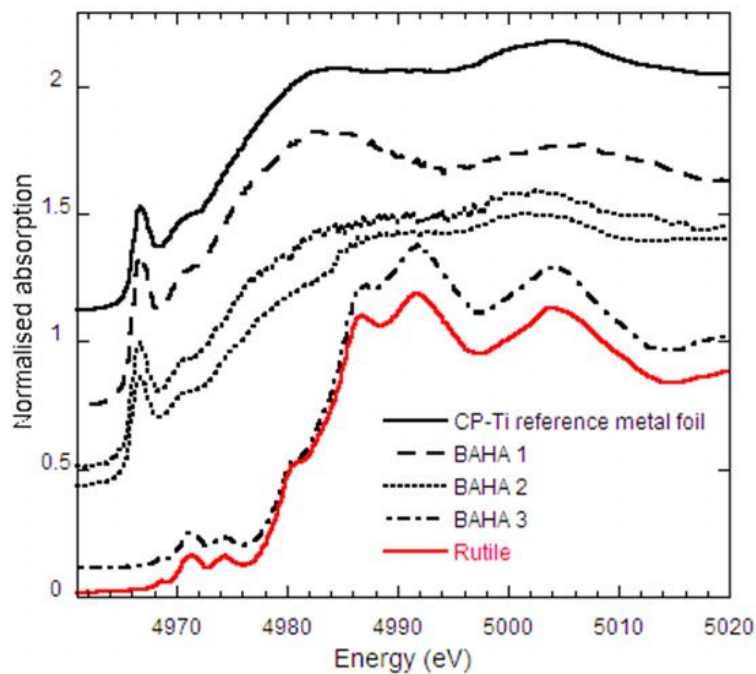


Figure 6.26 Normalised Ti K edge XANES spectra of BAHA tissues at three different regions

6.3. Discussion

XANES spectra inside the Ti artificial pit show a linear combination of Ti metal, TiCl_4 and titanium oxides. The intensity of pre-edge peak for Ti species within the pit is higher than that of Ti oxides due to the contribution of TiCl_4 to the overall shape of the spectrum. This observation is consistent with the measurements of Assfeld et al. [156] on TiCl_4 , which showed a very sharp and distinct pre-edge peak (see section 2.10.8.1). In contrast, the studies of Leon et al. [157] on TiCl_3 solution complexes showed a featureless pre-edge region at the same position. This indicates that the oxidation state of titanium oxidation inside the pit is 4+, which is consistent with the work of Beck [17, 18] and Kelly et al. [66], who reported 4+ as an oxidation state in chloride solutions.

XANES measurements revealed the presence of metal fragments and Ti oxides in human tissues. It is not surprising to find titanium species or metal particles in knee tissues since the knee implant is subjected to wear and movement. This can be related to micro-motion and wearing process of knee implant similar to the mechanism proposed by Thomas et al. [59] and Hallam et al. [58]. However, it is very surprising to find metallic fragments in BAHA and dental tissues since they are not under any movement or loading. Therefore, Ti metallic particles and species found in BAHA tissues can be possibly generated by a pure corrosion process. Ti metallic fragments were also found in the artificial pit. This observation is important since there is a possibility that metallic particles found in these tissues were generated by pure corrosion process. However, metallic fragments were generated in artificial pits at 7 V (Ag/AgCl) in 1 M HCl which is higher potential than would be found in the human body, but this simply shows the possibility of metal particles generation during electrochemical processes. Ti is very highly corrosion resistant, so it will only corrode when

there is a very concentrated solution of TiCl_4 in the cavity. If the TiCl_4 solution is diluted with water from the bulk solution, then the Ti will passivate. It is therefore possible that the localised corrosion of Ti takes place by a microscopic undercutting process (similar to the formation of lacy covers on stainless steel) [5, 6], in which pit only grows at the propagating front where the metal ions concentration is very high, while the rest of the pit surface is passive. The propagating front undermines the metal from within the micro cavity and eventually perforates the surface from beneath and makes a new hole into the bulk solution. This process may cause separation of micro-particles from the metal in titanium artificial pit.

Neutrophil cells were cultured in the presence of anatase powder and showed spectra similar to anatase in three measurements out of four. One sample with 100 ppm anatase showed a spectrum very similar to rutile and this observation is very interesting since the spectra obtained from the pit are predominantly anatase whereas tissues showed the presence of rutile species as well. Therefore it is possible that interaction of Ti species with cells can lead to the formation of rutile. However, only one sample out of four measurements showed this effect for neutrophil cells so further investigation is needed to confirm this.

Addition of BSA and Ringers solution to TiCl_4 resulted in the formation of anatase, whereas BSA addition to the pit solution led to formation of rutile. However, rutile was the predominant species found in tissue. This is consistent with the observation above of formation of rutile in neutrophil cells that had been exposed to anatase, suggesting that human tissue can convert anatase to rutile. However, further work is required to provide further data in support of this idea.

6.4. Conclusions

XANES spectra measured inside an artificial pit grown in CP-Ti in 1 M HCl show the presence of TiCl_4 and anatase in bright regions and predominantly metallic Ti in dark spots above the bright spots, consistent with the formation of metal fragments.

Mixing BSA or Ringers solution with TiCl_4 solution leads to the formation of anatase, but one measurement showed that addition of BSA to the pit solution leads to the formation of rutile.

Neutrophil cells cultured in the presence of 1000 ppm anatase gave a spectrum of anatase, whereas cells cultured in the presence of only 100 ppm anatase showed one spectrum of anatase and another of rutile suggesting the possibility that cells may be able to convert the anatase to rutile.

XANES spectra from human tissue around implants showed the presence predominantly of metallic fragments and rutile, although some anatase and an unidentified species were observed. The presence of metallic fragments is not surprising for tissues around knee where there is mechanical articulation, but is more surprising for bone-anchored hearing aids, suggesting the possibility that corrosion may lead to the formation of mechanical fragments as observed for the artificial pit. The presence of rutile in human tissue may be a result of the action of human cells on corrosion products, suggested by the observation of rutile formation in neutrophils cultured in the presence of anatase powder.

7. Summary

7.1.1. Fe, Cr, Ni speciation in 316L stainless steel artificial pits

X-ray absorption spectroscopy is a powerful technique to study the oxidation state and speciation of different elements in a solution environment. XANES has not been used extensively to study the pit solution chemistry of 316L stainless steel; therefore it was used as a new technique to explore 316L stainless steel artificial pits. XANES spectra were collected from a series of reference standards to compare with the spectra measured at various positions above the interface of the 316L stainless steel artificial pit to study the chemistry of alloying elements. The edge energy positions were compared with reference materials to examine the oxidation state as well as pre-edge and white line intensity to study the speciation in chloride environment near the mouth of the pit and close to the interface. These experiments showed the presence of chloro-complexes close to the interface for Fe and Cr resulting from the high chloride concentration at the dissolving interface, and hexa-aquo ions at the pit mouth. For Ni, only the hexa-aquo ion was found throughout the pit.

7.1.2. Mo speciation in 316L stainless steel artificial pits

The beneficial effect of Mo on corrosion behaviour of 316L stainless steel has been attributed to three different mechanisms. This improvement could be due to the effect of Mo on the passive layer, blocking of anodic dissolution by presence of Mo species on dissolving interface or formation of inhibiting molybdate species within the pit solution. Therefore a wide range of solid and solution Mo reference compounds were studied at different chloride concentrations to examine the oxidation state and Mo species at different positions relative to dissolving interface. The results did not confirm the mechanisms proposed by Kimura et al.

[13] involving corrosion inhibition by a molybdate network in the pit solution. The spatial resolution of the beam was not also enough to study the blocking dissolution mechanism.

7.1.3. Ti XANES studies in artificial pits and human tissues

Titanium alloys are used extensively in biomedical implants. However, Ti species can be released into human body environment by fretting, wear or corrosion and cause an inflammatory effects. XRF mapping was used to find regions with high concentrations of titanium in tissues taken from around failed knee, BAHA and dental implants, and local XANES measurements were then carried out to detect the species present. It was very surprising to find metal fragments in BAHA and dental tissues since they are not involved in any wear or mechanical process and this may be related to generation of metallic particles by pure corrosion process in these tissues. Rutile was found to be a dominant phase in knee tissues with a few measurements that showed anatase and metallic particles. BAHA tissues showed only metallic fragments and rutile; and dental tissues only showed the possibility of metal fragments with some unidentified species.

Similar measurements were carried out on neutrophil cells that had been cultured in the presence of anatase and then washed to remove external traces of the anatse. Three out of four measurements on these cells showed a spectrum indicating the presence of anatase but one showed a spectrum that corresponded to that rutile, suggesting the possibility that cells may be able to convert anatase to rutile.

XANES spectra were also obtained from a Ti artificial pit grown in 1 M HCl at 7 V (Ag/AgCl), which showed the presence of TiCl_4 , anatase, rutile and metallic fragments. The latter were found predominantly in dark spots above bright regions showing only

oxidised Ti, suggesting the possibility of metal fragments formation during the titanium corrosion process. However, the corrosion reaction took place at a much higher potential than would normally be found in the body.

8. Future work

EXAFS experiments can be planned on the same reference materials and positions inside the pit consistent with the XANES experiments to give more precise information of the coordination environment surrounding the Fe, Cr, Ni and Mo species inside the pit solution since the XANES technique is only able to determine the oxidation state and coordination structure.

Artificial Ti-6Al-4Al pits can be studied and compared with the results obtained from CP-Ti since Ti-6Al-4Al is commonly used in biomedical implants.

Larger scale future studies can be planned to explore the presence of Ti recovered from tissue surrounding a wide range of knee, BAHA and dental implants, exploring in more detail the effect of different Ti alloys. Furthermore, Ti distribution as a function of time in the body and as a function of distance from the implant surface can be investigated. The biological response of human cells to Ti corrosion processes can be investigated by adding different Ti compounds to neutrophil cells to study the inflammatory effects of Ti species. In addition, Ti electrochemical experiments can be carried out at different range of potentials as well as growing Ti artificial pits in the presence of proteins and peroxide species to more closely simulate the environment in the human body.

Titanium fragments released during corrosion of titanium artificial pit could be investigated further by using thinner foils to see if it is possible to see the morphology of attack in a similar way to Ernst and Newman [5, 6]. Alternatively, this could be investigated by looking at the localised corrosion of thin films similar to the work of Ryan et al. [42] who looked at 304 stainless steel foils by using 10 or 20 μm 316 stainless steel foils. It is also possible to

carry out SEM experiments on titanium artificial pit sample by looking at the corroded interface to investigate the morphology of the surface, and to carry out TEM measurements on the corrosion products in artificial pits to see the morphology of the metal particles.

9. References

1. M. J. Fontana, Corrosion Engineering. 3rd ed. 1988, Singapore: McGraw-Hill.
2. R. W. Revie, Uhlig's Corrosion Handbook. 2nd ed. 2000: John Wiley & Sons.
3. G. S. Frankel, Journal of the Electrochemical Society, 1998, 145(6): p. 2186-2198.
4. L. L. Shreir, R. A. Jarman and G. T. Burstein, Corrosion. 1993, Oxford: Butterworth Heinemann.
5. P. Ernst and R. C. Newman, Corrosion Science, 2002, 44: p. 927-941.
6. P. Ernst and R. C. Newman, Corrosion Science, 2002: p. 943-954.
7. T. P. Hoar, Transactions of the Faraday Society, 1937, 33(2): p. 1152-1166.
8. T. Suzuki, M. Yamabe and Y. Kitamura, Corrosion, 1973, 29(1): p. 18-22.
9. B. E. Wilde and E. Williams, Electrochimica Acta, 1971, 16(11): p. 1971-1985.
10. J. R. Galvele, Journal of the Electrochemical Society, 1976, 123(4): p. 464-474.
11. P. Ernst, N. J. Laycock, M. H. Moayed and R. C. Newman, Corrosion Science, 1997, 39(6): p. 1133-1136.
12. H. S. Isaacs, J. H. Cho, M. L. Rivers and S. R. Sutton, Journal of the Electrochemical Society, 1995, 142(4): p. 1111-1118.
13. M. Kimura, M. Kaneko and N. Ohta, Isij International, 2002, 42(12): p. 1399-1403.
14. R. C. Newman, Corrosion Science, 1985, 25(5): p. 341-350.
15. H. S. Isaacs, Electrochemical Science and Technology, November, 1973: p. 1456-1462.
16. J. W. Tester and H. S. Isaacs, Journal of the Electrochemical Society, 1975, 122(11): p. 1438-1445.
17. T. R. Beck, Journal of the Electrochemical Society, 1973, 120(10): p. 1310-1316.
18. T. R. Beck, Journal of the Electrochemical Society, 1973, 120(10): p. 1317-1324.
19. F. Hunkeler and H. Bohni, Corrosion chemistry within pits, crevices and cracks, ed. A. Turnbull, HMSO London, 1987: p. 27.
20. R. C. Newman and H. S. Isaacs, Passivity of metals and semiconductors, edited by M. Froment, 1983: p. 269-274.
21. U. Steinsmo and H. S. Isaacs, Corrosion Science, 1993, 35(1-4): p. 83-88.
22. U. Steinsmo and H. S. Isaacs, Journal of the Electrochemical Society, 1993, 140(3): p. 643-653.
23. R. C. Newman, M. A. A. Ajjawi, H. Ezuber and S. Turgoose, Corrosion Science, 1988, 28(5): p. 471-477.
24. Vetter K.J. and Strehblow H.H., NACE, Houston, 1974: p. 240.
25. P. Ernst and R. C. Newman, Electrochemical and Solid State Letters, 2008, 11(1): p. C1-C4.
26. R. C. Newman and E. M. Franz, Journal of the Electrochemical Society, 1984, 131(1): p. 223-225.
27. R. C. Newman and H. S. Isaacs, Journal of the Electrochemical Society, 1983, 130(7): p. 1621-1624.
28. T. R. Beck and R. C. Alkire, Journal of the Electrochemical Society, 1979, 126(10): p. 1662-1666.
29. R. D. Grimm and D. Landolt, Corrosion Science, 1994, 36: p. 1847-1868.
30. R. D. Grimm, A. C. West and D. Landolt, Journal of the Electrochemical Society, 1992, 139(6): p. 1622-1629.
31. F. Hunkeler, A. Krolikowski and H. Bohni, Electrochimica Acta, 1987, 32(4): p. 615-620.
32. D. Landolt. Mass Transport Process in High Rate Metal Dissolution and Deposition. M. Datta, in. 1996. Penington N.J.: Electrochemical Society Inc.
33. N. Sridhar and D. S. Dunn, Journal of the Electrochemical Society, 1997, 144(12): p. 4243-4253.

34. T. Suter and H. Bohni, *Electrochimica Acta*, 2001, 47(1-2): p. 191-199.
35. J. O. Park, T. Suter and H. Bohni, *Corrosion*, 2003, 59(1): p. 59-67.
36. G. T. Burstein, P. C. Pistorius and S. P. Mattin, *Corrosion Science*, 1993, 35(1-4): p. 57-62.
37. S. M. Ghahari, A. J. Davenport, T. Rayment, T. Suter, J. P. Tinnes, C. Padovani, J. A. Hammons, M. Stampanoni, F. Marone and R. Mokso, *Corrosion Science*, 53(9): p. 2684-2687.
38. J. Mankowski and Z. Szklarskasmialowska, *Corrosion Science*, 1975, 15(8): p. 493-501.
39. N. Sridhar and D. S. Dunn, *Corrosion*, 1994, 50(11): p. 857-872.
40. C. S. Brossia, D. S. Dunn and N. Sridhar, *Proceedings of The Symposium on Critical Factors in Localised Corrosion III: A Symposium in Honor of The 70th Birthday of Jerome Kruger*, 1999, 98(17): p. 485-499.
41. T. Hakkarainen. Anodic behaviour of stainless steel in simulated pit solutions. A. Turnball, in *Corrosion chemistry within pits, crevices and cracks*. 1987. London: HMSO.
42. M. P. Ryan, N. J. Laycock, H. S. Isaacs and R. C. Newman, *Journal of the Electrochemical Society*, 1999, 146(1): p. 91-97.
43. N. J. Laycock and S. P. White, *Journal of the Electrochemical Society*, 2001, 148(7): p. B264-B275.
44. R. Goetz and D. Landolt, *Electrochimica Acta*, 1982, 27(8): p. 1061-1070.
45. R. C. Newman, *Corrosion Science*, 1985, 25(5): p. 331-339.
46. R. Qvarfort, *Corrosion Science*, 1998, 40(2-3): p. 215-223.
47. J. N. Wanklyn, *Corrosion Science*, 1981, 21(3): p. 211-225.
48. K. Hashimoto, K. Asami and K. Teramoto, *Corrosion Science*, 1979, 19(1): p. 3-14.
49. K. Sugimoto and Y. Sawada, *Corrosion Science*, 1977, 17(5): p. 425-445.
50. H. Habazaki, A. Kawashima, K. Asami and K. Hashimoto, *Corrosion Science*, 1992, 33(2): p. 225-236.
51. K. Hashimoto, K. Asami, A. Kawashima, H. Habazaki and E. Akiyama, *Corrosion Science*, 2007, 49(1): p. 42-52.
52. Y. C. Lu, C. R. Clayton and A. R. Brooks, *Corrosion Science*, 1989, 29(7): p. 863-880.
53. A. Pardo, M. C. Merino, A. E. Coy, F. Viejo, R. Arrabal and E. Matykina, *Corrosion Science*, 2008, 50(6): p. 1796-1806.
54. M. Sakashita and N. Sato, *Corrosion Science*, 1977, 17(6): p. 473-486.
55. M. Urquidi-Macdonald and D. D. Macdonald, *Journal of the Electrochemical Society*, 1989, 136(4): p. 961-967.
56. L. Wegrelius, F. Falkenberg and I. Olefjord, *Journal of the Electrochemical Society*, 1999, 146(4): p. 1397-1406.
57. N. J. Laycock and R. C. Newman, *Corrosion Science*, 1997, 39(10-11): p. 1771-1790.
58. P. Hallam, F. Haddad and J. Cobb, *Journal of Bone and Joint Surgery-British Volume*, 2004, 86B(1): p. 27-30.
59. S. R. Thomas, D. Shukla and P. D. Latham, *Journal of Bone and Joint Surgery-British Volume*, 2004, 86B(7): p. 974-978.
60. M. U. C. Manivagasam G., Asokamani R., Raj B., *Corrosion Reviews*, 2003, 21(2-3): p. 125-159.
61. J. Mathieu, *Journal of The Electrochemical Society*, 1978, 125(7): p. 1039-1043.
62. J. Mathieu, *Journal of the Electrochemical Society*, 1978, 125(7): p. 1044-1049.
63. R. Quinn, *Journal of the Electrochemical Society*, 1978, 125(11): p. 1790-1796.
64. R. Nishimura and K. Kudo, *Corrosion Science*, 1982, 22(7): p. 637-645.
65. E. J. Kelly, *Journal of the Electrochemical Society*, 1976, 123(2): p. 162-170.
66. E. J. Kelly, *Journal of the Electrochemical Society*, 1979, 126(12): p. 2064-2075.
67. E. J. Kelly, *Modern Aspects of Electrochemistry*, 1982(14): p. 319-424.
68. I. Dugdale and J. B. Cotton, *Corrosion Science*, 1964, 4(1-4): p. 397-411.
69. N. Casillas, S. J. Charlebois, W. H. Smyrl and H. S. White, *Journal of the Electrochemical Society*, 1994, 141(3): p. 636-642.

70. N. Casillas, S. J. Charlebois, W. H. Smyrl and H. S. White, *Journal of the Electrochemical Society*, 1993, 140(9): p. L142-L145.
71. L. F. Garfias-Mesias, M. Alodan, P. I. James and W. H. Smyrl, *Journal of the Electrochemical Society*, 1998, 145(6): p. 2005-2010.
72. L. F. Garfias-Mesias and W. H. Smyrl, *Journal of the Electrochemical Society*, 1999, 146(7): p. 2495-2501.
73. G. T. Burstein, C. Liu and R. M. Souto, *Biomaterials*, 2005, 26(3): p. 245-256.
74. Z. L. Jiang, X. Dai, T. Norby and H. Middleton, *Corrosion Science*, 2011, 53(2): p. 815-821.
75. A. M. Fekry and M. A. Ameer, *International Journal of Electrochemical Science*, 2011, 6(5): p. 1342-1354.
76. J. Li, L. Zhou and Z. Li, *Rare Metals*, 2010, 29(1): p. 37-44.
77. J. Wang, J. Wu, Z. H. Zhang, X. D. Zhang, Z. J. Pan, L. Wang and L. A. Xu, *Ultrasound in Medicine and Biology*, 2006, 32(1): p. 147-152.
78. X. He, J. J. Noel and D. W. Shoesmith, *Corrosion Science*, 2005, 47(5): p. 1177-1195.
79. X. H. He, J. J. Noel and D. W. Shoesmith, *Journal of the Electrochemical Society*, 2002, 149(9): p. B440-B449.
80. L. Yan, J. J. Noel and D. W. Shoesmith, *Electrochimica Acta*, 2011, 56(4): p. 1810-1822.
81. S. Yu, *ASM Handbook*, ASM International, 2003, 13A: p. 703-711.
82. M. I. Abdulsalam, *Journal of Materials Engineering and Performance*, 2007, 16(6): p. 736-740.
83. N. J. Hallab and J. J. Jacobs, *Corrosion Reviews*, 2003, 21(2-3): p. 183-213.
84. N. T. Thomas and K. Nobe, *Journal of the Electrochemical Society*, 1972, 119(11): p. 1450-&.
85. R. D. Armstrong, J. A. Harrison, H. R. Thirsk and Whitfield.R, *Journal of the Electrochemical Society*, 1970, 117(8): p. 1003-1006.
86. I. Cserenyak, G. H. Kelsall and W. Wang, *Electrochimica Acta*, 1996, 41(4): p. 563-572.
87. I. Cserenyak, G. H. Kelsall and W. Wang, *Electrochimica Acta*, 1996, 41(4): p. 573-582.
88. F. A. Cotton and G. Wilkinson, *Advanced Inorganic Chemistry*. 6th ed. 1999. 695-710.
89. M. Pourbaix, *Atlas of Electrochemical Equilibria in Aqueous Solutions*. 1974: NACE. 217.
90. V. A. Joshi, *Titanium Alloys. in Titanium Alloys*. 2006, Boca Raton: CRC Press.
91. I. J. Polmear, *Light Alloys, Metallurgy of light alloys*. 1995: Butterworth-Heinemann Ltd.
92. C. Leyens and M. Peters, *Titanium and Titanium Alloys*. 2003, Koln: Wiley-VCH.
93. N. J. Hallab and J. J. Jacobs, *Corrosion Reviews*, 2003, 21(2-3): p. 183-213.
94. M. Long and H. J. Rack, *Biomaterials*, 1998, 19(18): p. 1621-1639.
95. C. Aparicio, *Biomaterials*, 2003, 24(2): p. 263-273.
96. J. J. Jacobs, A. K. Skipor, J. Black, R. M. Urban and J. O. Galante, *Journal of Bone and Joint Surgery-American Volume*, 1991, 73A(10): p. 1475-1486.
97. J. Black, *Biomaterials*, 1984, 5(1): p. 11-18.
98. R. M. Urban, J. J. Jacobs, J. L. Gilbert and J. O. Galante, *Journal of Bone and Joint Surgery-American Volume*, 1994, 76A(9): p. 1345-1359.
99. A. Sargeant and T. Goswami, *Materials & Design*, 2007, 28(1): p. 155-171.
100. M. L. Wang, R. Tuli, P. A. Manner, P. F. Sharkey, D. J. Hall and R. S. Tuan, *Journal of Orthopaedic Research*, 2003, 21(4): p. 697-707.
101. M.-C. Bernier, K. El Kirat, M. Besse, S. Morandat and M. Vayssade, *Colloids and surfaces. B, Biointerfaces*, 2012, 90: p. 68-74.
102. M. L. Guo, H. Z. Sun, H. J. McArdle, L. Gambling and P. J. Sadler, *Biochemistry*, 2000, 39(33): p. 10023-10033.
103. A. D. Tinoco, E. V. Eames and A. M. Valentine, *Journal of the American Chemical Society*, 2008, 130(7): p. 2262-2270.
104. N. J. Hallab, K. Mikecz, C. Vermes, A. Skipor and J. J. Jacobs, *Molecular and Cellular Biochemistry*, 2001, 222(1-2): p. 127-136.

105. J. A. Bardwell, G. I. Sproule, B. Macdougall, M. J. Graham, A. J. Davenport and H. S. Isaacs, Journal of the Electrochemical Society, 1992, 139(2): p. 371-373.
106. A. J. Davenport and M. Sansone, Journal of the Electrochemical Society, 1995, 142(3): p. 725-730.
107. A. J. Davenport, M. Sansone, J. A. Bardwell, A. J. Aldykiewicz, M. Taube and C. M. Vitus, Journal of the Electrochemical Society, 1994, 141(1): p. L6-L8.
108. J. Kruger and G. G. Long, Journal of the Electrochemical Society, 1986, 133(8): p. C302-C302.
109. G. G. Long, J. Kruger, D. R. Black and M. Kuriyama, Journal of Electroanalytical Chemistry, 1983, 150(1-2): p. 603-610.
110. O. M. Magnussen, J. Scherer, B. M. Ocko and R. J. Behm, Journal of Physical Chemistry B, 2000, 104(6): p. 1222-1226.
111. A. J. Davenport, L. J. Oblonsky, M. P. Ryan and M. F. Toney, Journal of the Electrochemical Society, 2000, 147(6): p. 2162-2173.
112. A. J. Davenport, M. P. Ryan, M. C. Simmonds, P. Ernst, R. C. Newman, S. R. Sutton and J. S. Colligon, Journal of the Electrochemical Society, 2001, 148(6): p. B217-B221.
113. H. S. Isaacs and S. M. Huang, Journal of the Electrochemical Society, 1996, 143(12): p. L277-L279.
114. A. Adriaens and M. Dowsett, Surface Engineering, 2008, 24(2): p. 84-89.
115. J. Monnier, S. Reguer, D. Vantelon, P. Dillmann, D. Neff and I. Guillot, Applied Physics a-Materials Science & Processing, 99(2): p. 399-406.
116. R. De Marco, Z. T. Jiang, B. Pejcic and E. Poinen, Journal of the Electrochemical Society, 2005, 152(10): p. B389-B392.
117. B. Ingham, M. Ko, G. Kear, P. Kappen, N. Laycock, J. A. Kimpton and D. E. Williams, Corrosion Science, 52(9): p. 3052-3061.
118. T. J. Marrow, L. Babout, A. P. Jivkov, P. Wood, D. Engelberg, N. Stevens, P. J. Withers and R. C. Newman, Journal of Nuclear Materials, 2006, 352(1-3): p. 62-74.
119. M. Newville, Consortium for Advanced Radiation Sources, 2004, Rev 1.6: p. 3-9.
120. S. Virtanen, P. Schmuki, A. J. Davenport and C. M. Vitus, J. Electrochem. Soc., Jan 1997, 144: p. 198-204.
121. G. Bunker, Introduction to XAFS, A practical guide top X-ray absorption fine structure spectroscopy. 2010, Cambridge: Cambridge University Press.
122. A. Ide-Ektessabi and M. Rabionet, Analytical Sciences, 2005, 21(7): p. 885-892.
123. C. F. A. and W. G., 6th ed., 1999: p. 775-814.
124. M. J. Apted, G. A. Waychunas and G. E. Brown, Geochimica Et Cosmochimica Acta, 1985, 49(10): p. 2081-2089.
125. M. Benfatto, J. A. Solera, J. G. Ruiz and J. Chaboy, Chemical Physics, 2002, 282(3): p. 441-450.
126. L. Galoisy, G. Calas and M. A. Arrio, Chemical Geology, 2001, 174(1-3): p. 307-319.
127. G. A. Waychunas, M. J. Apted and G. E. Brown, Physics and Chemistry of Minerals, 1983, 10(1): p. 1-9.
128. T. E. Westre, P. Kennepohl, J. G. DeWitt, B. Hedman, K. O. Hodgson and E. I. Solomon, Journal of the American Chemical Society, 1997, 119(27): p. 6297-6314.
129. D. Testemale, J. Brugger, W. H. Liu, B. Etschmann and J. L. Hazemann, Chemical Geology, 2009, 264(1-4): p. 295-310.
130. W. Liu, B. Etschmann, G. Foran, M. Shelley and J. Brugger, American Mineralogist, 2007, 92(5-6): p. 761-770.
131. F. A. Cotton and G. Wilkinson, Advanced Inorganic Chemistry. 6th edition. 1999. 736-756.
132. W. Kharmawphlang, S. Choudhury, A. K. Deb and S. Goswami, Inorganic Chemistry, 1995, 34(14): p. 3826-3828.
133. M. Magini, Journal of Chemical Physics, 1980, 73(5): p. 2499-2505.
134. P. K. Wrona, Inorganic Chemistry, 1984, 23(11): p. 1558-1562.

135. S. DiazMoreno, A. MunozPaez, J. M. Martinez, R. R. Pappalardo and E. S. Marcos, Journal of the American Chemical Society, 1996, 118(50): p. 12654-12664.
136. F. A. Cotton and G. Wilkinson, 6th edition, 1999: p. 835-854.
137. J. X. Ji and W. C. Cooper, Electrochimica Acta, 1996, 41(9): p. 1549-1560.
138. C. A. Angell and D. M. Gruen, Journal of the American Chemical Society, 1966, 88(22): p. 5192-&.
139. K. Waizumi, T. Kouda, A. Tanio, N. Fukushima and H. Ohtaki, Journal of Solution Chemistry, 1999, 28(2): p. 83-100.
140. Kleinber.R, Journal of Chemical Physics, 1969, 50(11): p. 4690-&.
141. P. D'Angelo, O. M. Roscioni, G. Chillemi, S. Della Longa and M. Benfatto, Journal of the American Chemical Society, 2006, 128(6): p. 1853-1858.
142. P. D'Angelo, M. Benfatto, S. Della Longa and N. V. Pavel, Physical Review B, 2002, 66(6).
143. S. P. Cramer, P. K. Eidem, M. T. Paffett, J. R. Winkler, Z. Dori and H. B. Gray, Journal of the American Chemical Society, 1983, 105(4): p. 799-802.
144. F. Jalilehvand, V. Mah, B. O. Leung, D. Ross, M. Parvez and R. F. Aroca, Inorganic Chemistry, 2007, 46(11): p. 4430-4445.
145. K. Yokoi, N. Matsubayashi, T. Miyanaga, I. Watanabe and S. Ikeda, Polyhedron, 1993, 12(8): p. 911-914.
146. K. Yokoi, N. Matsubayashi, T. Miyanaga, I. Watanabe, S. Ikeda and K. Murata, Polyhedron, 1989, 8(1): p. 45-49.
147. F. Farges, American Mineralogist, 1997, 82(1-2): p. 36-43.
148. F. Farges, American Mineralogist, 1997, 82(1-2): p. 44-50.
149. F. Farges and G. E. Brown, Geochimica Et Cosmochimica Acta, 1997, 61(9): p. 1863-1870.
150. F. Farges, G. E. Brown and J. J. Rehr, Physical Review B, 1997, 56(4): p. 1809-1819.
151. F. Farges, G. E. Brown and J. J. Rehr, Geochimica Et Cosmochimica Acta, 1996, 60(16): p. 3023-3038.
152. S. D. George, P. Brant and E. I. Solomon, Journal of the American Chemical Society, 2005, 127(2): p. 667-674.
153. N. Jiang, D. Su and J. C. H. Spence, Physical Review B, 2007, 76(21): p. 1-9.
154. G. A. Waychunas, American Mineralogist, 1987, 72(1-2): p. 89-101.
155. X. C. Yang, M. Dubiel, D. Ehrt and A. Schutz, Journal of Non-Crystalline Solids, 2008, 354(12-13): p. 1172-1174.
156. X. Assfeld, J. Garcia, J. I. Garcia, J. A. Mayoral, M. G. Proietti, M. F. Ruizlopez and M. C. Sanchez, Journal of the Chemical Society-Chemical Communications, 1994(18): p. 2165-2166.
157. A. Leon, O. Kircher, J. Rothe and M. Fichtner, Journal of Physical Chemistry B, 2004, 108(42): p. 16372-16376.
158. M. Uo, K. Asakura, A. Yokoyama, M. Ishikawa, K. Tamura, Y. Totsuka, T. Akasaka and F. Watari, Dental Materials Journal, 2007, 26(2): p. 268-273.
159. R. McRae, P. Bagchi, S. Sumalekshmy and C. J. Fahrni, Chemical Reviews, 2009, 109(10): p. 4780-4827.
160. T. Kekesi, T. I. Torok and M. Isshiki, Hydrometallurgy, 2005, 77(1-2): p. 81-88.
161. M. Kimura, M. Kaneko and T. Suzuki, Journal of Synchrotron Radiation, 2001, 8: p. 487-489.
162. J. F. W. Mosselmans, P. D. Quinn, A. J. Dent, S. A. Cavill, S. D. Moreno, A. Peach, P. J. Leicester, S. J. Keylock, S. R. Gregory, K. D. Atkinson and J. R. Rosell, Journal of Synchrotron Radiation, 2009, 16: p. 818-824.
163. R. Farrow, G. E. Derbyshire, B. R. Dobson, A. J. Dent, D. Bogg, J. Headspith, R. Lawton, M. Martini and K. Buxton, Nuclear Instruments & Methods in Physics Research Section B-Beam Interactions with Materials and Atoms, 1995, 97(1-4): p. 567-571.
164. K. J. S. Sawhney, I. P. Dolbnya, M. K. Tiwari, L. Alianelli, S. M. Scott, G. M. Preece, U. K. Pedersen and R. D. Walton, A Test Beamline on Diamond Light Source, in *Sri 2009: The 10th*

- International Conference on Synchrotron Radiation Instrumentation*, R. G. I. N. K. W. S. Garrett, Editor. 2010. p. 387-390.
- 165. A. J. Dent, G. Cibin, S. Ramos, A. D. Smith, S. M. Scott, L. Varandas, M. R. Pearson, N. A. Krumpa, C. P. Jones and P. E. Robbins, B18: A core XAS spectroscopy beamline for Diamond, in *14th International Conference on X-Ray Absorption Fine Structure*, A. F. A. DiCicco, Editor. 2009.
 - 166. B. Ravel and M. Newville, *Journal of Synchrotron Radiation*, 2005, 12: p. 537-541.
 - 167. A. Thompson, *X-Ray Data Booklet*. 2001, Berkeley: Lawrence Berkeley National Laboratory.
 - 168. C. S. Brossia, D. S. Dunn and N. Sridhar, *Proceedings of the Symposium on Critical Factors in Localized Corrosion* iii, 1999, 98(17): p. 485-499.
 - 169. J. J. Verbist, T. F. Koetzle, M. S. Lehmann and W. C. Hamilton, *Journal of Chemical Physics*, 1972, 56(7): p. 3257-3264.
 - 170. M. Urquidi-Macdonald and D. D. Macdonald, *J. Electrochem. Soc.*, 1989, Vol. 136(No. 4): p. 961-967.
 - 171. T. Rayment, A. J. Davenport, A. J. Dent, J. P. Tinnes, R. J. K. Wiltshire, C. Martin, G. Clark, P. Quinn and J. F. W. Mosselmans, *Electrochemistry Communications*, 2008, 10(6): p. 855-858.
 - 172. P. M. Wang, L. L. Wilson, D. J. Wesolowski, J. Rosenqvist and A. Anderko, *Corrosion Science*, 52(5): p. 1625-1634.
 - 173. D. E. Sands and A. Zalkin, *Acta Crystallographica*, 1959, 12(10): p. 723-726.
 - 174. S. J. George, O. B. Drury, J. X. Fu, S. Friedrich, C. J. Doonan, G. N. George, J. M. White, C. G. Young and S. P. Cramer, *Journal of Inorganic Biochemistry*, 2009, 103(2): p. 157-167.
 - 175. K. Shinoda, E. Matsubara, M. Saito, Y. Waseda, T. Hirato and Y. Awakura, *Zeitschrift Fur Naturforschung Section a-a Journal of Physical Sciences*, 1997, 52(12): p. 855-862.
 - 176. K. Sjobom and B. Hedman, *Acta Chemica Scandinavica*, 1973, 27(10): p. 3673-3691.
 - 177. Z. Amilius, B. Vanlaar and H. M. Rietveld, *Acta Crystallographica Section B-Structural Crystallography and Crystal Chemistry*, 1969, B 25: p. 400-402.